Architecture study for in-orbit long term cryogenic storage

As support to space exploration

Ludovica Formisani

Technische Universiteit Delft

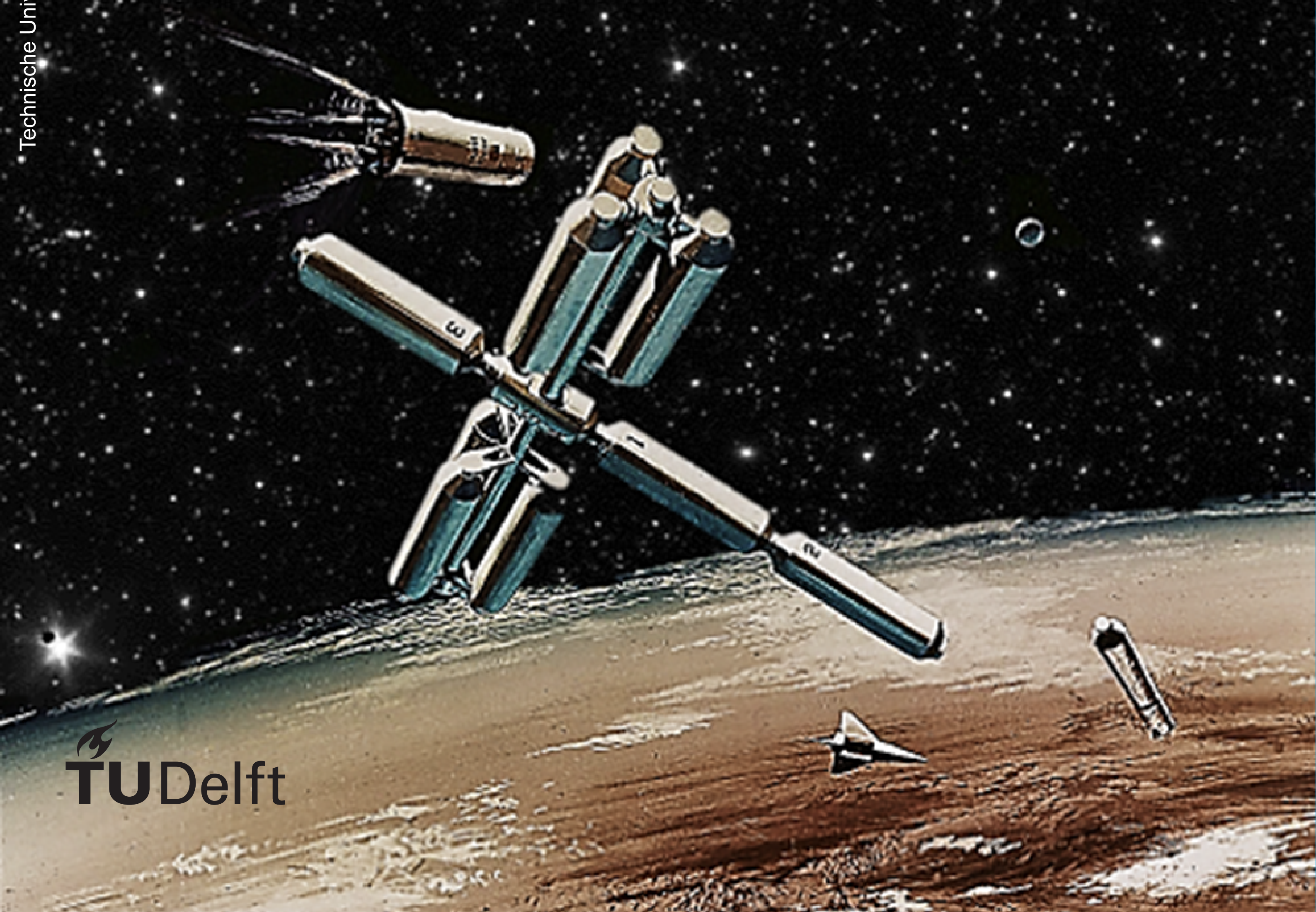

TU Delft

Architecture study for in-orbit long term cryogenic storage

As support to space exploration

by

Ludovica Formisani

to obtain the degree of Master of Science
at the Delft University of Technology,
faculty of Aerospace Engineering,
to be defended publicly on Monday October 10, 2022 at 9:30 AM.

Student number:	5379156	
Project duration:	February 8, 2022 – October 10, 2022	
Thesis committee:	Professor B.T.C. Zandbergen	TU Delft, supervisor
	Associate Professor J. Guo	TU Delft, chair
	Researcher I. Uriol Balbin	TU Delft, examiner

An electronic version of this thesis is available at `http://repository.tudelft.nl/`.
Cover image credit of NASA.

TU Delft

Preface

Earth is the cradle of humanity, but one cannot remain in the cradle forever.

Konstantin E. Tsiolkovsky

This work can be considered the rightful end to one of the most enriching and challenging experiences of my life. Doing my Master of Science in Spaceflight at the Delft University of Technology has been an honor, giving me the guidance, resources, and knowledge to pursue this research and to follow my dreams. So many people have been fundamental to build the person that is writing this page today. I am not able to name all of you, that would require another full thesis, but I am sure that you will be able to identify yourself by reading this.

My deepest gratitude goes to my thesis supervisor, professor Barry Zandbergen. Your support, help, and guidance have been indispensable to me during my journey. Thank you for passing on to me your passion towards this topic and to showing me that great teachers are first of all great human beings. *Dank je wel.*

A special thanks goes to my thesis group colleagues. Thank you for offering me guidance and support, especially when the work seemed so far from being finished and the numbers did not seem to make sense.

To my friends in Delft. This work would have not existed without you. I am beyond grateful for all the time spent together, from studying in room 2.62 to bouldering and pizza on Fridays. Thank you for the parties, for the *gezelligheid*, for the Space bars, the concerts, and the dinners cooking exotic dishes. Thank you for the days as tourists in The Netherlands, the conferences and the beautiful experiences we had together. Thank you for literally saving this thesis by introducing me to the wonderful world of Python. Thank you for the assignments together and the endless Teams calls.
I am grateful for The Student Hotel, and for strangers that became family. Thank you for the house in Rijswijk, for the Domino's pizza as a reward for the hard work and the Ben and Jerry's for happy and dark days. Thank you for always bringing the Sun to me, both in Delft and in Vollenhove.

Ai miei amici a casa. A quelli che ci sono sempre stati, e a quelli che sono arrivati proprio nel momento giusto, per poi non andare più via. A quelli che mi sono vicini ogni giorno, a quelli che ascoltano i miei messaggi audio infiniti, e a quelli che quando sento anche dopo tanto tempo, è come se non fosse passato un giorno. Grazie per essere rimasti sempre al mio fianco, vincendo il tempo e la distanza. Voi siete la famiglia che ho scelto.

Alla mia mamma e al mio papà, che mi hanno sopportata e supportata in ogni momento della mia vita e senza i quali non sarei diventata la persona che sono oggi. Ai miei nonni, che hanno sempre creduto in me. Alla mia famiglia, che è per me punto di rifermento, posto sicuro, e piena dimostrazione che la vera bellezza si trova nell'essere unici.

You all have supported and encouraged me every step of the way, and I will forever be grateful for this. It is now time for me to go out of my cradle and reach for the stars.

Ludovica Formisani
Delft, October 2022

Abstract

The space community is currently focusing on defining mission architectures able to perform multiple interplanetary missions to support deep space exploration. In particular, placing orbital propellant depots in strategic locations in space would allow to increase the useful payload mass at launch.
Despite all the efforts that are being invested in finding effective propellant solutions, cryogenics are still widely used within the space industry. In particular, the hydrolox combination (formed by liquid hydrogen and oxygen) is the most used as it returns the best Δv performance thanks to its high specific impulse. However, this class of propellants faces an issue that could jeopardize all the mass savings: boil-off. This consists in propellant evaporation due to heat penetration in the tank structure, and it could become so severe for long storage times (in the order of months) that the additional propellant mass used to make up for the boil-off losses would nullify all the benefits that come from the high impulse of these mixtures.
Therefore, it is clear that the design of the propellant depot depends greatly on the propellant storage duration and the thermal environment it experiences, and finding efficient boil-off reduction strategies is fundamental. The aim of this work is to evaluate the thermal performance of different depot architectures for different thermal environments and mission durations, and to identify the one that is most mass efficient.

The approach taken in this work consists in developing a propellant depot sizing model that allows determining the effect of different thermal control design options, thermal environments, and depot configurations for varying mission duration. To do so, a literature review on the currently employed thermal control technologies for in-orbit storage is first performed to find out which methods are the best to be selected for this work.
The model performs a multi-nodal thermal analysis to estimate boil-off rates and allows for taking into account different thermal control methods, which include Multi-Layer Insulation with uniform and variable density distributions and Vapour Cooled Shields. This is done by extending an original version of the Boil-off tool. The extensions include, among others, a flexible thermal network structure, an ESATAN-TMS based thermal environment definition, and a variety of thermal control design options.
Alongside the program development, a sensitivity study on the design choices and the assumptions made is performed to evaluate the robustness of the tool.

Finally, the analysis of different depot architectures is performed. In particular, Low Earth and Geostationary orbits are investigated as locations for a depot, with the possibility to extend the results to the Earth-Moon Lagrange point L1. As for the depot, both single and multi-tank configurations are studied.
Results showed that variable density MLI (VDMLI) improves the effectiveness of the thermal insulation compared to the uniform density case: the most mass efficient designs in terms of insulation plus boil-off mass are achieved with less total number of layers when VDMLI is used.
The use of a vapor cooled shield (VCS) additionally reduces the boil-off into the cryogenic tank. However, for the VCS to become advantageous in terms of mass, a minimum storage duration is needed: this corresponds to two months for the LEO depot, and at least six for the GEO depot. This is due to the mass penalty introduced by the addition of the metal shield into the system.
Lastly, it is shown that multi-tank depots have increased boil-off rates than single tank depots due to the effect of reflected fluxes among the depot elements. However, some propellant savings come from placing the cryogenic tank in the shadow of the other tanks of the depot station.

Nomenclature

Acronyms

ACES	Advanced Common Evolved Stage
BO	Boil-off
ESATAN-TMS	ESATAN Thermal Modelling Suite
GEO	Geostationary Orbit
GH2	Hydrogen in vapor phase
GRC	Glenn Research Centre
IR	Infra-red
L	Left tank side
LCH4	Liquid Methane
LEO	Low Earth Orbit
LH2	Liquid Hydrogen
LOX	Liquid Oxygen
MCRT	Monte Carlo ray-tracing method
MLI	Multi-Layer Insulation
NASA	National Aeronautics and Space Administration
NEA	Near Earth Asteroid
O/F	Oxidizer-to-Fuel ratio
R	Right tank side
RHS	Right Hand Side
S1, S2, S3	VDMLI inner, middle and outer sector
SOFI	Spray-on Foam Insulation
TMM	Thermal mathematical model
TRL	Technology Readiness Level
UDMLI	Uniform Density Multi-Layer Insulation
ULA	United Launch Alliance
VCS	Vapor Cooled Shield(s)
VDMLI	Variable Density Multi-Layer Insulation
ZBO	Zero Boil-Off

Greek symbols

α	Spectral absorptivity	-
α_p	Argument of periapsis	deg
ΔT	Temperature difference	K
Δv	Velocity change	m/s
γ	Isentropic expansion coefficient	-
μ_{vap}	Dynamic viscosity of vented vapor	Pa s
Ω	Right ascension of ascending node	deg
ϕ	Solar incidence angle	rad
ρ	Spectral reflectivity	-
ρ_a	Albedo factor	-
ρ_m	Specific weight of a reflector layer	kg/m^2
ρ_s	Specific weight of a spacer layer	kg/m^2
σ	Stefan-Boltzmann constant	W/m$^2 K^4$
τ	Spectral transmissivity	-
ε	Spectral emissivity	-
ε_{in}	MLI inner emissivity (single reflector layer)	-

Roman symbols

$\dot{m}_{\text{boil-off}}$	Boil-off rate	kg/s
$\dot{m}_{\text{evap}}$	Evaporation rate at liquid-vapor interface	kg/s
$\dot{m}_{\text{venting}}$	Venting rate	kg/s
$\dot{Q}_{\text{cond}}$	Rate of conduction heat transfer	W
$\dot{Q}_{\text{conv}}$	Rate of convection heat transfer	W
$\dot{Q}_{\text{emit}}$	Radiation emitted by real surface	W
$\overline{N}$	MLI layer density	layers/cm
$\overline{T}_F$	Average temperature of the fluid	K
A	Area	m^2
a,b,c	Lockheed equation constants	-
A_{cont}	Heat transfer contact area	m^2
A_{emit}	Emitting surface area	m^2
A_{frontal}	Frontal area of surface considered	m^2
C_p	Specific heat capacity	J/kgK
dm_{boiloff}	Boil-off mass increase (or decrease) for time-step dt	kg
dm_{vent}	Vented mass in time-step dt	kg

dp_{vapor}	Pressure increase (or decrease) of vapor in ullage for time-step dt	Pa
$dQ_{\text{vapor,net}}$	Total heat leak into vapor in ullage for time-step dt	W
dT_{vapor}	Temperature increase of vapor in ullage for time-step dt	K
d_{VCS}	VCS tube diameter	m
dt	Time step	s
dT_{node}	Temperature increase (or decrease) of single node for time-step dt	K
F	Visibility factor	-
h	Orbit altitude from planet surface	m
H_a, H_p	Altitude of orbit apogee and perigee	m
h_{conv}	Convection heat transfer coefficient	W/m^2K
h_{VCS}	VCS convection heat transfer coefficient	W/m^2K
i	Integration step	-
i_{orbit}	Orbit inclination	deg
k	Thermal conductivity	W/mK
k_{vap}	Thermal conductivity of vented vapor	W/mK
l	Conductive path length	m
L_{vap}	Latent heat of vaporization	J/kg
M	Mass	kg
m, n	Lockheed equation constant exponents	-
M_m	Molar mass	kg/mol
m_{vapor}	Vapor mass in tank ullage	kg
$m_{\text{vap,fin}}$	Vapor mass in ullage after venting	kg
N_s	Number of MLI layers	-
Nu_{vap}	Nusselt number of vented vapor	-
P^*	MLI interstitial pressure	torr
$P_{\text{dissipated}}$	Power dissipated	W
p_{max}	Maximum pressure in tank	Pa
$p_{\text{vap,fin}}$	Ullage pressure after venting	Pa
$p_{\text{vap,in}}$	Ullage pressure before venting	Pa
Pr	Prandtl number	-
Q_{absorbed}	Absorbed heat	W
Q_{albedo}	Albedo heat load	W
Q_{emitted}	Emitted heat	W
$q_{\text{gas conduction}}$	gas conduction heat flux through the MLI	W/m^2

Q_{in}	Incoming heat	W
Q_{IR}	Planetary IR heat load	W
$Q_{\text{leak,liq}}$	Total heat leak into bulk liquid	W
$q_{\text{liquid}\rightarrow\text{vapor}}$	Heat flux between ullage and bulk liquid	W/m^2
q_{Lock}	Total heat flux through the MLI (from the Lockheed equation)	W/m^2
$Q_{\text{N,next}}$	Heat exchanged with next node in thermal network	W
$Q_{\text{N,opp}}$	Heat exchanged with opposite node in thermal network	W
$Q_{\text{N,prev}}$	Heat exchanged with previous node in thermal network	W
Q_{net}	Net heat leak into the node	W
Q_{out}	Outgoing heat	W
$q_{\text{radiation}}$	Radiation heat flux through the MLI	W/m^2
$Q_{\text{S,next}}$	Heat exchanged with next sub-node in thermal network	W
$Q_{\text{S,prev}}$	Heat exchanged with previous sub-node in thermal network	W
Q_{solar}	Direct solar heat load	W
$q_{\text{solid conduction}}$	Solid conduction heat flux through the MLI	W/m^2
Q_{tank}	Total heat leak into tank	W
Q_{VCS}	Heat absorbed by VCS system	W
$q_{\text{wall}\rightarrow\text{liquid}}$	Heat flux into bulk liquid from insulation	W/m^2
$q_{\text{wall}\rightarrow gas}$	Heat flux into ullage gas from insulation	W/m^2
R_e	Earth radius	m
R_G	Universal gas constant	J/molK
Re	Reynolds number	-
S	Direct solar radiation	W/m^2
T_C	Temperature cold side of MLI	K
T_F	Temperature of fluid	K
T_H	Temperature hot side of MLI	K
T_m	MLI average temperature	K
t_m	Nominal thickness of reflector layer	m
t_s	Nominal thickness of spacer layer	m
T_{in}	Temperature of VDMLI inner sector	K
T_{mid}	Temperature of VDMLI middle sector	K
t_{MLI}	Thickness of MLI	m
T_{out}	Temperature of VDMLI outer sector	K
T_{sat}	Saturation temperature	K

T_{space}	Outer space temperature	K
T_{s}	Temperature of the solid	K
$T_{\text{vap,fin}}$	Vapor temperature in ullage after venting	K
$T_{\text{vap,in}}$	Vapor temperature in ullage before venting	K
T_{VCS}	VCS shield temperature	K
$T_{F,\infty}$	Temperature of the fluid far from the solid surface	K
V_{cap}	Tank end-cap volume	m^3
V_{cyl}	Tank cylindrical body volume	m^3
V_{tot}	Total tank internal volume	m^3
V_{vapor}	Volume of vapor in ullage	m^3

List of Figures

List of Tables

Contents

1 Introduction

The current trend in space exploration is to develop advanced systems that are able to transport humans to the far edges of the Solar System. Indeed, the farther is the destination, the bigger is the velocity change (Δv) to be applied to the spacecraft and thus the amount of propellant needed. According to the Tsiolkovsky rocket equation[1], a way to achieve the same Δv with less propellant mass would be to select a mixture with a high specific impulse [2]. Reducing the propellant mass stored on board of a spacecraft would result either in mass (and cost) savings at launch, or increase the useful payload mass to be launched in space.

According to [1], storable propellant combinations (that is, liquid at space ambient temperatures) are mostly used for bi-propellant low-thrust and reaction control rocket engines, allowing for long-term storage and instant readiness. On the other hand, cryogenic propellant mixtures are preferred for upper rocket stages and booster stages of launch vehicles. In particular, the cryogenic oxygen-hydrogen propellant system (also called hydrolox) is characterized by the highest specific impulse among the available non-toxic liquid rocket propellant combinations, and thus is considered the most suitable for missions that require high velocity changes.

A major drawback of cryogenic propellants that could jeopardize all the mass savings is boil-off. This is unused propellant which comes from cryogen evaporation due to heat penetration in the tank structure. For current systems, this boil-off is about 1% per day of the initial stored propellant mass [2]. Such a high boil-off rate can easily nullify the benefits of using cryogenic propellants.

One of the options considered for future space exploration is in-orbit (re)fuelling of spacecrafts from orbital propellant depots, allowing to reduce the amount of propellant stored in launch vehicles, thus allocating more mass to payload [3]. In particular, orbital propellant depots are designed for storage durations that vary from a few days up to several months, depending on the mission objectives. For these systems, boil-off reduction becomes fundamental.

The aim of this work is to evaluate the thermal performance of different propellant depot architectures, and to identify the one that is most mass efficient.

More details on the work to be performed are given in this chapter, together with a brief introduction to cryogenic technologies and propellant depots state-of-the-art. The research plan is also presented, together with the report layout.

[1] The maximum achievable change of velocity of the vehicle is: $\Delta v = I_{\mathrm{sp}} g_0 \ln \frac{m_0}{m_f}$, with I_{sp} specific impulse measured in seconds, g_0 standard gravity, m_0 the rocket's wet mass and m_f the dry mass [1].

[2] Figure of merit of the performance of any rocket propulsion system, defined as the ratio of the total impulse generated by the rocket (during the burn time t) to the total weight of propellant used: $I_{sp} = \frac{\int_0^t F dt}{g_0 \int_0^t \dot{m} dt}$, with F thrust force, g_0 standard gravity, and $\dot{m}$ total propellant mass flow rate [1].

1.1. Cryogenic technologies to support space missions

Cryogenic [3] technologies as a way to improve payload capability of space vehicles have been studied since the beginning of the space exploration era. For example, the National Aeronautics and Space Administration (NASA) Glenn Research Center (GRC), began experimentation with cryogenic propellants in the early 1940s, to then starting operating small rocket engines from 1950 using liquid oxygen and hydrogen as propellant [4]. This started a chain of events that led to one of the greatest achievements in the history of human space exploration: the landing of the Apollo 11 on the Moon in 1969, powered by the hydrogen-oxygen cryogenic propellant mixture.

Ever since then, research on cryogenics has continued to move forward. Liquid hydrogen and oxygen (LH2/LOX) have been argued by [5] to be the best propellant mixture in terms of performance, thanks to its very high specific impulse (between 460 s and 480 s in vacuum for an oxidizer-to-fuel ratio of 6:1). Furthermore, an analysis performed by Lockheed Martin [6] showed that using hydrolox based propulsion systems would reduce initial mass launched in Low Earth Orbit (LEO) by more than 45% with respect to storable bi-propellant and solid systems, as shown in Figure 1.1. These savings indeed increase for interplanetary missions, where the required initial launch mass is greater.

The hydrolox mixture has been also considered suitable for onsite production, for example for the Mars Base Camp mission with Surface Sorties [7]. In this mission scenario, resupply cryogenics are envisioned to be generated by splitting water via electrolysis, with large quantities of water (103 MT per sortie) being delivered from Earth or placed in the Mars orbit as a sort of fuel depot.

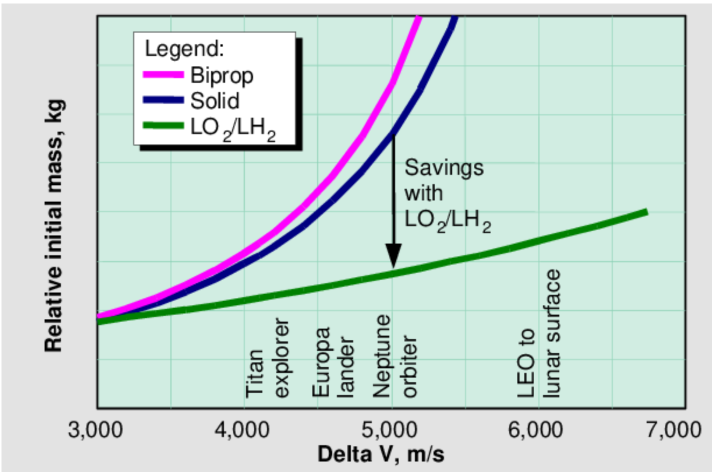

Figure 1.1: Initial mass savings of hydrolox compared to other propellant mixtures based on required velocity change [6].

It should be noted that in the comparison shown in Figure 1.1, the attention is focused only on the mass savings that the hydrolox mixture brings as a result of the reduced propellant mass required to achieve the same velocity change as storable propulsion systems.

When using cryogenic-based systems, other factors need to be taken into account, such as the mass of the tank structure used to store the propellants (the structural coefficient[4] is in general higher for hydrolox stages compared to storable bipropellant and solid rocket stages [8]). Additional system mass would also be allocated for the thermal control of the cryogenic propellant in the tank, which needs to be kept at very low temperatures (about 20 K for hydrogen and 90 K for oxygen) to limit boil-off losses. In fact, the more these losses are, the more is the additional propellant mass to be stored in the tank. All the above-mentioned factors add-up complexity and technical challenges to the design of cryogenic propellant systems that need to be tackled to keep their mass advantage over storable propellants.

According to [2], the Centaur designs estimated a boil-off rate on the order of 4-5%/day and about 1-2%/day of the initially stored mass of liquid hydrogen and oxygen respectively. These rates were

[3] *Cryogenics* is defined as the production and behaviour of materials at very low temperatures (below 120 K).

[4] This is defined as the ratio of the structural mass M_s of the rocket stage and the propellant mass M_p loaded on the stage: $\sigma_s = \frac{M_s}{M_p}$ [8].

lowered to a minimum of 1%/day by implementing improvements of the insulation structure. It is clear that the mission duration strongly influences boil-off rates requirements. Such high boil-off rates as the Centaur's have been considered acceptable for missions from a few days up to a week-long.

One of the options considered for future space exploration is in-orbit (re)fuelling of spacecrafts from orbital propellant depots. Orbital propellant depots would in fact allow to allocate more vehicle launch mass to payload, while propellant is launched on less expensive (because uncrewed) launch vehicles [3]. These depots are designed for storage durations on the order of several months, which can vary depending on the mission objectives. For these systems, using current passive heat insulation technologies would allow to reduce the cryogen boil-off rate below 3% of the initial stored mass per month [9].

Even with this reduced boiling rate, the boil-off issues starts to become challenging when storage durations exceed 6 months [9]. Therefore, adopting efficient boil-off reduction strategies that would be able to achieve minimum boil-off rates is fundamental, requiring dedicated thermal design solutions that are object of the analysis performed in this work.

1.2. Orbital propellant depots state of the art

In the past years, the concept of space depots and in orbit refuelling has become one of the considered options for long-term space missions, because it allows size and cost savings by a factor up to 10 [10]. This system consists in orbiting tanks expressly designed to support on-orbit refueling to increase the payload capability of launch vehicles.

According to [11], for any mission architecture beyond Low Earth Orbit (LEO), the propellant mass can represent 70% or more of the total mass assembled in orbit. Another advantage that comes with propellant depots is the possibility to support multiple missions with the same station. This solution first of all allows to save mass from the depot assembly in space, because once the station is positioned in orbit, the only action required is to periodically refill it with the needed propellant. Moreover, this also eases the boil-off losses by reducing the storage time between one mission and the other. The higher the number of missions, the less the storage time of the propellant between one mission and the following. In their study, [12] have confirmed that propellant depots are fundamental for the space exploration evolution, as they improve the extensibility and mission payload capability.

The birth of the concept of orbital propellant depots goes back to 1965 [13], when early orbital tanker designs started to be proposed to the scientific community. Ever since, this concept has drawn increasing attention. In 2006, [14] developed a scalable depot sizing tool, and applied it to a Low Earth Orbit (LEO) case study. However, several other locations have been proposed, like for example the Earth-Moon Lagrange points, or even orbits about the Moon or Mars.

The first propellant depot concepts were based on adapting existing launchers and upper stages designs for long-term orbital storage ([15], [16]). This was done to minimize risks and uncertainties. One example is the single-launch LH2/LOX propellant depot shown in Figure 1.2a, which has been developed by the United launch Alliance (ULA) from an existing upper-stage and designed for long-duration missions beyond LEO [16]. This single depot concept, called the Advanced Common Evolved Stage (ACES) depot, can also be included in a cluster of other identical vehicles to improve the overall depot station propellant capability to support interplanetary missions, for example to Mars. This multi-depot concept is shown in Figure 1.2b.

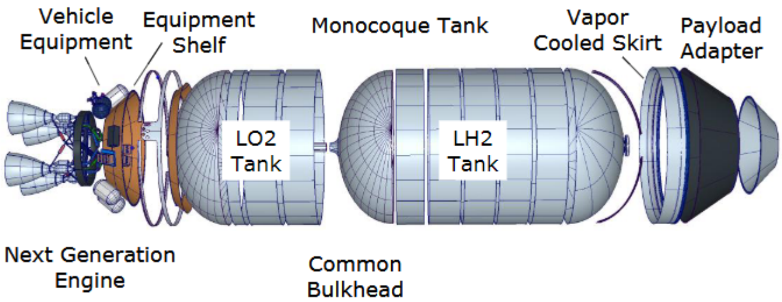

(a) The ACES single depot concept.

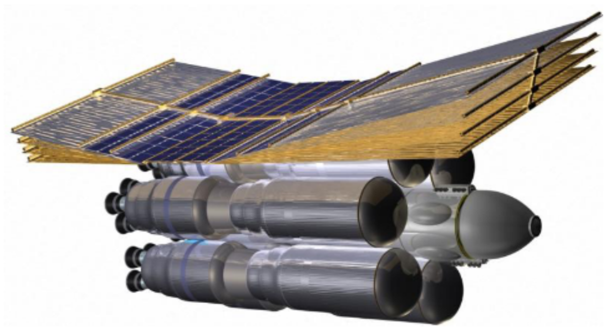

(b) Clustered ACES depots to increase propellant capacity.

Figure 1.2: Advanced Common Evolved Stage (ACES) single and multi-depot concept [16].

Another depot concept has been proposed by [15]. This consists in a single tank depot containing a single fluid (either liquid hydrogen or oxygen), which is assembled on Earth and launched empty to eliminate the need of foam insulation, thereby allowing for a mass reduction. In fact, foam is only properly working in atmospheric environments as its task is to reduce the convective heat transfer [17]. Once in orbit, the depot is protected from the thermal radiation sources with a pneumatically deployed Sun shield, as shown in Figure 1.3a.

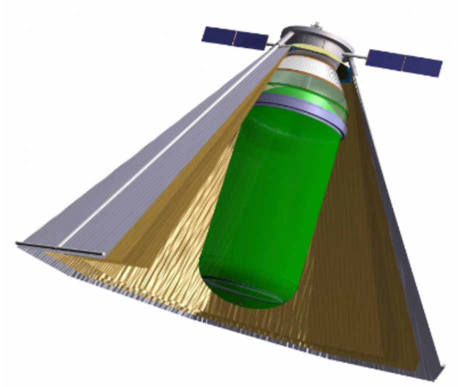

(a) Single tank depot concept protected by Sun shield [15].

(b) Multi-tank orbital depot propellant facility [3].

Figure 1.3: Single and multi-tank depot concepts.

According to [3] and [18], there is also the possibility of pre-positioning the depot in orbit to support multiple missions. The depot is formed by one (Figure 1.3a) or multiple (Figure 1.3b) tanks, and it is assembled in orbit; standardized interfaces allow compatibility with multiple launch suppliers. This solution would decouple the depot itself, which would not depend on the needs and timelines of a specific mission anymore.

In any case, in-orbit refuelling would require orbital propellant depots that are able to store cryogenics for long durations while in orbit: for these systems, boil-off reduction becomes fundamental.
Boil-off reduction can be achieved with both passive and/or active means. Passive thermal control systems involve no mechanical moving parts or fluids, and there is no power consumption, thus ensuring lower mass and cost [19]. Among these, Multi-Layer Insulation (MLI) [20] is the most used technology, and it consists in foils coated with a highly reflective metal and with low thermal conductive spacers placed in between so that they are not in direct contact. On the other hand, active thermal control systems make use of moving fluids, mechanisms or power to transfer heat. Among these, it is worth to mention cryogenic coolers (also called cryocoolers or cryogenic refrigerators) [21]. Cryocoolers are particularly suitable to achieve zero Boil-off (ZBO) designs [19].

A performance study of a cryogenic orbital depot employing both passive and active systems has been proposed by [11]. In particular, the analysis focused on combinations of MLI and cryocoolers for LEO storage of liquid hydrogen (LH2) and oxygen (LOX). Results showed that the ZBO option is only achievable with the employment of cryocoolers; however, the current state of the art of in-space cryocoolers does not include systems powerful enough to achieve ZBO for the hydrogen tank, thus introducing the need to find alternative thermal control solutions that would at least minimize the propellant boil-off losses. Among these, vapor cooled shields (VCS) are of interest to this work. This technique consists in using the boil-off vapors from the ullage to cool down the tank walls before being vented overboard. Studies over VCS have been performed by [22] and [23], and they have both shown that these systems reduce the heat leak into the tank.

1.3. Research plan

To the author's knowledge, no system study assessing the effectiveness of employing VCS on orbital propellant depots currently exists. Furthermore, only few studies assess the performance of multiple combinations of thermal design options for long-term storage, and in most of cases, the tools used for the analysis are not publicly available.
The objective of this study is to develop a propellant depot sizing tool (the "Boil-off tool") which is then applied to some case studies to evaluate different thermal control design options. In particular, a first version of this tool has already been developed in the work of Borst [24], which is thus used as starting point of this research.
Main object of interest is the thermal performance, as it is the driving factor in most studies.

1.3.1. Research questions

This brings to the main research question of this thesis work:
Can successful strategies for applying active and passive cooling methods for in-orbit cryogenic storage be identified in terms of total system mass with focus on a chosen mission?

Which is then detailed into several sub-questions that lead the thesis project:

1. Can a computational tool be developed such that it allows for analysing a space mission and selecting the best design option based on total system mass minimization?

2. Can the importance of tank configuration and location be identified for attaining the lowest mass for a cryogenic propellant depot for a specific mission?

3. Can boil-off venting solutions lead to a system mass reduction for orbital propellant depots?

4. What are suitable mission architectures for this study and why?

5. What is the influence of the thermal environment on the results?

6. Does the outcome of the study change between missions with different architectures and durations?

1.4. Thesis report layout

This chapter has been dedicated to a brief introduction on the topic object of this study and on the research plan linked to this thesis work. In chapter 2, some more background information is given on the main elements object of this study. In particular, the spacecraft external thermal environment and the thermal control technologies currently employed for in-orbit cryogenic storage are described.
Using the information gathered in the literature review phase, chapter 3 follows the methodology adopted in this work. In particular, the approach used to model the thermal environment, and the sizing and thermal analysis tool are described. A sensitivity analysis on the assumptions made and the models described in the Methodology chapter is performed in chapter 4.

Chapter 5 and chapter 6 are then dedicated respectively to the mission architectures definition, and the analysis and discussion of the simulations results. In particular, all the mission architectures identified in chapter 5 are analysed and compared.
Finally, the conclusions and recommendations for future work on the topic of in-orbit cryogenic storage are given in chapter 7.

The results of this thesis work have also been presented at the International Astronautical Congress (IAC) in Paris, 18-22 September 2022. The paper published in the conference proceedings can be found in Appendix C.

2

Literature review

The literature review performed in this chapter gives an overview of the most important boil-off mitigation technologies, with the objective of finding out which methods are the best to be selected for the present work.
Attention has also been focused on the causes of the boil-off phenomenon in cryogenic tanks in space: thermal radiation coming from the Sun and the planets is responsible of the majority of the heat fluxes on the spacecraft. For this reason, a brief description of the source of these fluxes is given with the aim to identify the most critical phases in terms of thermal inputs for a specific mission.

Finally, more information on the Boil-off tool to be used for the analysis are given, together with a summary of the tool extensions this work aims to include.

2.1. Spacecraft thermal environment

Spacecraft in Earth orbits receive radiative energy from three main external sources [17]: direct solar radiation, albedo radiation (sunlight reflected from the Earth) and outgoing long-wave radiation emitted by the planet and its atmosphere (OLR or IR radiation). Moreover, energy could also be absorbed by the spacecraft as a result of internal heat generation by power dissipating electrical components. According to [17], the thermal control of a spacecraft is attained by balancing all the above described incoming heat sources with the energy re-emitted by the spacecraft as infra-red radiation. These different heat sources are shown in Figure 2.1, while their relationship is described by Equation 2.1.

$$\begin{aligned} &Q_{in} = Q_{out} \\ &Q_{absorbed} + P_{dissipated} = Q_{emitted} \\ &Q_{solar} + Q_{albedo} + Q_{IR} + P_{dissipated} = Q_{emitted} \end{aligned} \tag{2.1}$$

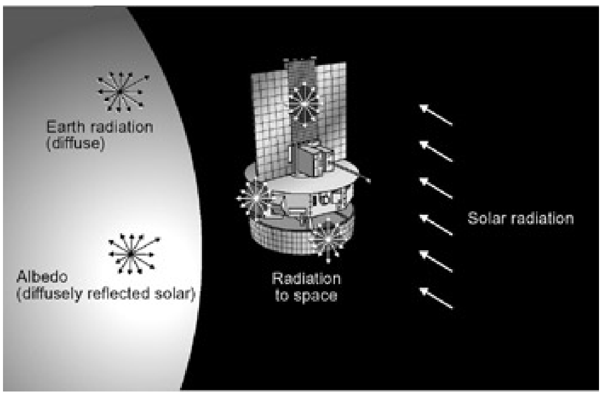

Figure 2.1: Spacecraft thermal environment heat sources [17].

Since the spacecraft is in motion with respect to the planet, it is fundamental to estimate the intensity of the thermal fluxes incoming on its surfaces and their variability over time.

2.1.1. Direct solar radiation

Direct solar radiation is considered the greatest source of heat in Earth orbit, and, being the Sun a stable energy source, its intensity remains always constant within a 1 % fraction [17]. However, what is subject to variations ($\pm 3.5\%$) is the intensity of sunlight reaching Earth due to the slightly elliptical orbit of the Earth around the Sun itself. The most extreme solar flux cases experienced by a spacecraft in Earth orbit (1 AU[1] from the Sun), together with their average value, recommended by the World Radiation Center (WRC) [25], are shown below:

- Hot case: $S_{hot} = 1414\ W/m^2$ (winter solstice)
- Median case: $S_o = 1367\ W/m^2$ (the solar constant[2])
- Cold case: $S_{cold} = 1322\ W/m^2$ (summer solstice)

2.1.2. Planetary albedo

The albedo factor of a planet is defined as the fraction of solar heat flux that is reflected by the planet back into space. Albedo is not a point source, and it varies considerably through the globe because it depends on the position of reflective elements on the planet's surface, such as clouds (that increase albedo) or water surfaces (which reflect less than continental areas). Moreover, this fraction tends to increase with latitude because of snow and ice cover .

It has to be noted that the albedo factor is a reflectivity, and not a flux [17]. Therefore, the albedo heat load on a spacecraft orbiting Earth strongly depends on the relative position between the solar vector and the spacecraft itself. In other words, albedo flux can be zero even when the factor is not, as it happens when the spacecraft is in the planet's shade: the planet is *potentially* able to reflect a part of the sunlight, but there is no sunlight to be reflected at that moment [3]. This effect is expressed in terms of a visibility factor F, which depends on the distance of the spacecraft to the planet and the angle between the local vertical and the Sun rays [27].

The albedo radiation intensity incident on a spacecraft orbiting Earth can then be defined as [27]:

$$q_{\text{albedo}} = \rho_a F S_o \tag{2.2}$$

Where ρ_a and F are respectively the albedo and visibility factor, which both assume values between 0 and 1. In particular, in case one would be interested in the worst hot and cold thermal conditions, the angle dependence of the visibility factor F can be neglected, resulting in $F = 0$ when the spacecraft is in the planet's shadow, and $F = \left(\frac{R_e}{R_e+h}\right)^2$, when the spacecraft is facing the sunlit side of the planet [28]. R_e and h refer respectively to the Earth radius and the orbit altitude.

According to [27], especially in case of complex spacecraft in low planetary orbits, albedo inputs require accurate calculations as function of the orbital position and the spacecraft geometry, which can be performed using dedicated software tools.

2.1.3. Outgoing Long-wave Radiation

Earth emitted radiation is a combination of: radiation emitted in infrared (IR) wavelengths by atmospheric gases and radiation emitted by the Earth's surface and cloud tops (which is partially absorbed in the atmosphere). This radiation is primarily influenced by the temperature of the planet surface and the amount of cloud coverage. In fact, warmer surface regions emit more than colder ones, while an increased cloud cover lowers Earth emitted IR since clouds actually block part of the radiation emitted from the Earth's surface. Nevertheless, according to [17], localized Earth IR radiation variations are less severe than albedo ones.

According to [27], for the thermal design of a spacecraft, it is safe to assume that Earth radiates uniformly from its cross-sectional area with an intensity of $237\ W/m^2$. Therefore, the Earth IR radiation

[1] Unit of length, corresponding to the Sun-Earth distance and equal to about 150 million kilometres.

[2] The definition of solar constant, according to [26], is: *"the radiation that falls on a unit area of surface normal to the line from the Sun, per unit time and outside of the atmosphere, at one astronomical unit (mean Earth - Sun distance)."*

incident on a spacecraft can be calculated as follows:

$$q_{IR} = 237\left(\frac{R_{\text{rad}}}{R_e + h}\right)^2 \tag{2.3}$$

Where R_{rad} is the radius of the effective radiating surface of Earth, which is usually assumed to be the same as the Earth radius R_e. With this assumption, the same visibility factor F identified for the albedo radiation can be used to compute the intensity of planetary IR on the spacecraft.

2.1.4. Thermal environment determination using ESATAN-TMS

The determination of the space thermal environment can be very complex depending on the geometry, attitude, and location of a spacecraft in orbit. However, an accurate estimation of the intensity of the radiation incident on every surface is fundamental for the production of a functional thermal design.
As suggested by [27], the use of a dedicated software would be ideal to get a thermal radiation estimation that is close to the real case and that is able to account for many variable parameters at the same time. Among the currently available state-of-the-art software suites, it is worth mentioning THERMICA®, ESATAN-TMS®, or Thermal Desktop®.
All these tools use the Monte Carlo ray-tracing method[3] (MCRT) to determine the fluxes onto a geometric model given orientation and orbit, which can be also calculated as a function of time in case of not stable conditions (e.g. an orbit with eclipse, or a spacecraft spinning about its axis).
Another option is the Analytical Graphic's System Tool Kit (STK®) software, which has been used to also perform a thermal system analysis for orbital propellant depots [11]. However, the shape of the objects modelled with this tool are limited to spherical and planar only.

The ESATAN Thermal Modelling Suite [29] is a general purpose thermal-radiative software tool, and it is one of the standards used within the space industry. This program allows the user to create a thermal model by defining materials, geometry, optical properties of the finishes used, boundary conditions, and many other parameters needed to perform the thermal analysis.

One important feature of the ESATAN-TMS software, and the one of interest to this work, is the "Mission characterization". This allows to define the space environment the spacecraft depot is in. Orbit and attitude definition can be done by the user, together with the Sun/planet environment characterization. Once the geometry of the depot has been defined, the ESATAN-TMS radiative analysis is able to compute all the heat fluxes coming to the depot during a specific mission, no matter how complex the model geometry might be. In particular, the program returns as output both the incoming fluxes and the absorbed ones. The main difference between them is that the former is generated solely from the depot geometry, while the latter include the effect of the defined thermo-optical properties of the surface, that is they include absorbed and reflected fluxes (if any) between the model faces.

ESATAN-TMS is a powerful tool for thermal design and analysis of objects that operate in the space environment, and it is the software suite used in this work to simulate the external thermal environment in which the propellant depot operates. The main reason behind the choice of ESATAN-TMS over the other tools mentioned above, besides its versatility, is its licence availability for the Delft University of Technology.

Given the stochastic nature of the MCRT method, it is worth to give some information about the accuracy of its results. According to the ESATAN-TMS user manual [29], the estimated values are within a band with a width which is inversely proportional to the square root of the number of rays fired. Therefore, increasing the number of rays indeed also increases the accuracy of the results, but it can comport significantly longer run times for the calculations. Being a deep accuracy study of the tool not among the objectives of this work, the default settings (10,000 rays/face) are used for the radiative computations in ESATAN-TMS.

2.2. Heat transfer mechanisms

Whenever there is a temperature difference between two system, energy is transferred in the form of heat. This can happen in three modes, namely conduction, convection, and radiation [30]. This section describes in more detail each mode, and how they are involved in the thermal definition of a spacecraft.

[3] This is a stochastic method that estimates radiative couplings and thermal fluxes by averaging the results of a ray-tracing procedure which considers the history of a finite sample of rays (or energy packets), from their point of emission to absorption [29].

2.2.1. Conduction

Conduction is defined as the heat transferred because of molecules collisions and diffusion in liquids and gases, and because of the combination of molecules vibration and the energy transported by free electrons in solids [30]. Conduction heat transfer is described by the Fourier's law of heat conduction, which defines the rate of heat conduction as:

$$\dot{Q}_{\text{cond}} = \frac{k \cdot A}{l}\Delta T = -kA\frac{dT}{dx} \tag{2.4}$$

Where k is the thermal conductivity of the medium (W/mK), A is the cross sectional area, l (dx in its differential form) is the conductive path length and ΔT is the temperature difference across the path l. The minus in the differential form of the equation indicates that the direction of conduction heat transfer is opposite to the direction of the temperature gradient in the medium, that is it goes in the direction of decreasing temperature.

2.2.2. Convection

Convection is defined as the heat transfer between a solid surface and an adjacent gas or liquid in motion. That is, convection is a combination between conduction and fluid motion effects [30].
Convection can be forced in case external means such pumps, fans or the wind are used to direct the fluid towards a surface. On the contrary, if the fluid motion is induced by buoyancy forces due to density differences, the convection is called free or natural. Free convection is for example one of the processes involved in the boiling of a liquid.
The rate of convection heat transfer is expressed using Newton's law of cooling [30]:

$$\dot{Q}_{\text{conv}} = h_{\text{conv}}A_{\text{cont}}(T_S - T_{F,\infty}) \tag{2.5}$$

Where h_{conv} is the convection heat transfer coefficient (W/m^2K), A_{cont} is the contact area between solid and fluid, T_s is the temperature of the solid, and $T_{F,\infty}$ is the temperature of the fluid far from the solid surface.
Unlike the thermal conductivity, the convection heat transfer is not a property of the fluid, but it is usually determined experimentally and depends on many factors such as the surface geometry, the fluid flow characteristics, its velocity, and the nature of convection (forced or natural) [30]. For example, a relation to estimate the value of this coefficient for a particular case is given later in this chapter (subsection 2.4.3).

2.2.3. Radiation

Radiation consists in emitted energy in the form of electromagnetic waves due to changes in the electronic configurations of atoms and molecules [30]. In particular, all the bodies that have a temperature above 0 K emit thermal radiation. This is the only form of heat transfer that can happen without the presence of a medium, therefore it is not attenuated in vacuum and is the main form of heat transfer in space.
The radiation emitted by real surfaces is described by the Stefan-Boltzmann law [30]:

$$\dot{Q}_{\text{emit}} = \varepsilon\sigma A_{\text{rad}}T_S^4 \tag{2.6}$$

Where σ is the Stefan-Boltzmann constant ($5.67 \times 10^{-8}\ W/m^2K^4$), A_{emit} is the emitting area, and T_S is the temperature of the surface. As for ε, this is an optical property of the surface called emissivity, and its value is in the range between 0 and 1. In particular, a surface that emits the maximum amount possible of thermal radiation is called blackbody and has an emissivity equal to 1.

Another optical property of a radiating surface is its absorptivity α, which represents the fraction of the total radiation energy incoming on a surface that is actually absorbed by the surface. The thermal radiation that is not absorbed can be reflected and/or transmitted by the surface. The optical properties corresponding to these two effects are respectively the reflectivity ρ and the transmissivity τ, which satisfy the following equivalence: $\alpha + \rho + \tau = 1$.
Finally, emissivity and absorptivity are related by the Kirchhoff's law of radiation, which states that for a given temperature and wavelength: $\varepsilon = \alpha$ [30].

2.2.4. Thermal mathematical model (TMM)

The structure of spacecraft is complex and characterized by many temperature gradients that vary over time and based on the spacecraft location. However, a correct estimation of these temperatures is still fundamental to produce efficient thermal control designs. For this reason, thermal engineers often make use of a simplified representation of the spacecraft structure, known as the thermal mathematical model (TMM) [27].

In particular, this consists in generating a network of discrete regions called *thermal nodes*. The simplification lies in the fact that each node of the network is considered isothermal, meaning that all temperature gradients within the same region are neglected. Furthermore, each node has a temperature, a mass and a heat capacity depending on the material, and it is connected to surrounding nodes through conductive and radiative links, also known as couplings.

With the TMM, the thermal behaviour of the spacecraft is described by a set of non-linear differential equations, in number equal to the total number of nodes in the network. This same approach is used in this work, thus more details about the structure of the non-linear equations for the thermal behaviour of the depot are given later in the Methodology chapter 3.

2.3. Thermal control technologies

As just described above, a cryogenic storage tank in orbit is subjected to different incident fluxes that may vary depending on the tank location and its position in the orbit. For example, in case of LEO, the tank can alternate periods of maximum fluxes (when facing the Sun) to no fluxes (when in eclipse). These variations indeed affect the cryogen boil-off.

Boil-off consists in propellant evaporation in the storage tank due to heat leaks from the surrounding environment. The longer the mission duration, the more the propellant boil-off. This loss needs to be compensated for by loading more propellant on board. However, there is a point where boil-off becomes so severe that cryogenic systems may not represent the best option anymore, because they require to store more propellant than traditional storable systems. Adding passive and active cooling surely allows longer mission durations, however they also add mass to the vehicle. For this reason, the additional dry mass coming from thermal control systems and the actual boil-off mass need to be balanced so to attain the minimum loaded mass.

2.3.1. Multi-Layer Insulation (MLI)

According to [20], Multi-Layer Insulation (MLI) consists of multiple Kapton or Mylar foils placed parallel to each other. The foils are coated with a highly reflective metal, while low thermal conductive spacers are placed in between the foils so that they are not in direct contact. Pictures of the radiation foils and different types of spacers used are shown in Figure 2.2.

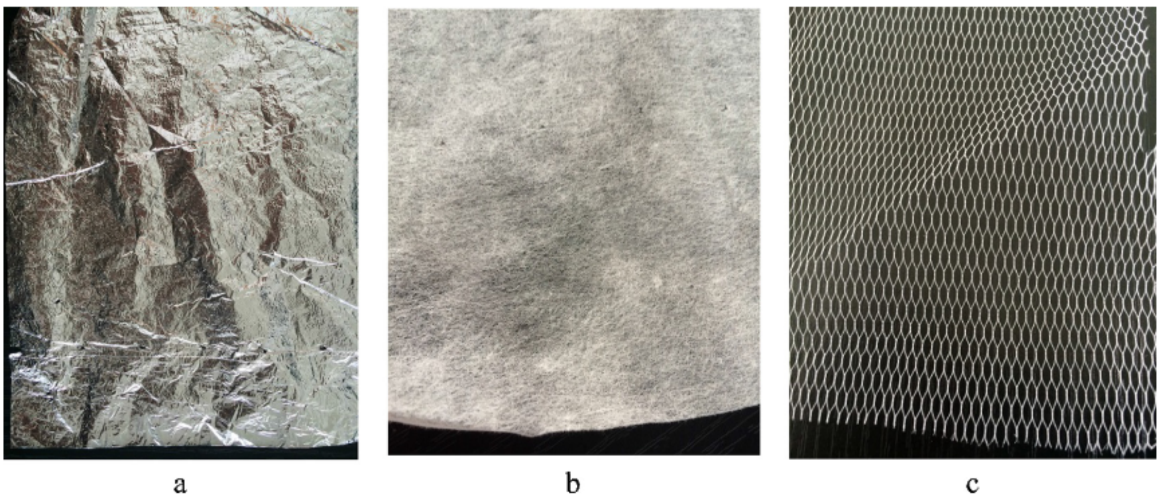

Figure 2.2: Radiation shield and spacers details (a. radiation shield, b. none-woven fiber cloth, c. Dacron net) [31].

A detailed break-down of an MLI system is shown in Figure 2.3a. These systems are capable of maintaining very high temperature gradients across thin insulation (the effective thickness of a typical MLI is few millimeters).

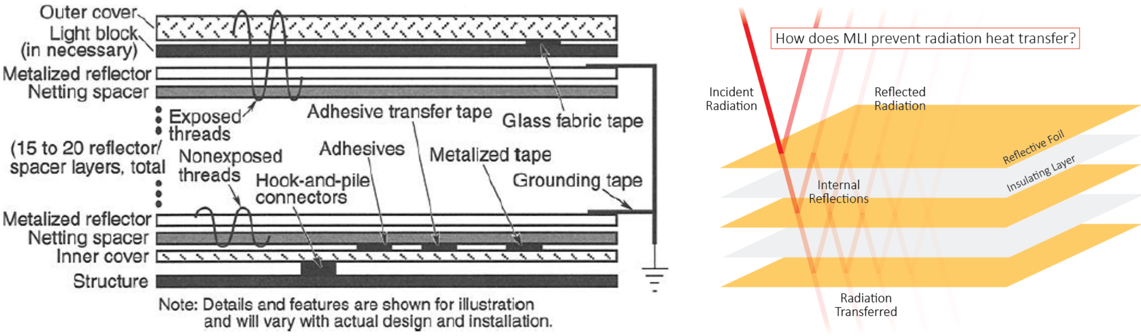

(a) Structure of MLI ([32]).

(b) Schematic of MLI ([33]).

Figure 2.3: Multi-Layer insulation structure and functioning.

The working principle of MLI insulation is shown in Figure 2.3b. When the radiation from space strikes the first MLI layer, a part of it is reflected back, while the other is absorbed by the foil itself, which heats up. This process generates a temperature gradient and heat is transferred to the next foil through solid conduction, gas conduction and radiation. The second foil reflects a part of this radiation, while the remaining energy is transferred to the third foil and so on.
As already mentioned, the main forms of heat transfer that involve MLI are: radiation, solid conduction and gas conduction; several techniques are employed simultaneously in these systems to guarantee that all three forms of heat transfer are reduced. Ideally, a well functioning MLI blanket has as many reflector layers as possible to limit radiative heat transfer (this effect is also shown in Figure 2.3b). To minimize solid conduction, it would be preferable to separate each reflector layer with the least number of low-conductive spacers, however the number of spacers needs to be enough to guarantee no contact between the reflective foils. Lastly, gas conduction is minimized by allowing the MLI system to vent into space any residual gas after launch [17].

MLI is an important insulating material used in the field of cryogenics, and it is the most common thermal control element on a spacecraft [17]. Multiple studies have been conducted to best estimate the MLI performance (some of them are mentioned in [20]), which is affected by several factors such as contact pressure, boundary temperature, interstitial gas and pressure.
Several relations for MLI performance estimation have been developed. For example,[34] has adopted numerical approach called "layer-by-layer", which is able to assess the thermal performance of the MLI through the analytical analysis of each separate layer in the system. However, the complexity of this approach indeed increases with the number of layers considered.

An empirical relation to estimate the thermal performance of MLI without performing the layer-by-layer analysis is the Lockheed model, which has been developed by [35]. In this model all three heat transfer mechanisms are considered. Among the three effects, radiation has been proven to be the most critical in space, where vacuum conditions almost eliminate the gas conduction effect. As for solid conduction, according to [34] this is due to the presence of materials to support and separate the reflector layers; thus, there are some techniques that can be used to reduce, but not totally eliminate, thermal conduction effects. The Lockheed model is shown in Equation 2.7:

$$\begin{aligned} q_{\text{Lock}} &= q_{\text{solid conduction}} + q_{\text{radiation}} + q_{\text{gas conduction}} \\ q_{\text{Lock}} &= \frac{a\left(\overline{N}\right)^{n} T_m \left(T_H - T_C\right)}{N_s} + \frac{b\varepsilon_{\text{in}}\sigma\left(T_H^{4.67} - T_C^{4.67}\right)}{N_s} + \frac{cP^*(x,T)\left(T_H^{(m+1)} - T_C^{(m+1)}\right)}{N_s} \end{aligned} \tag{2.7}$$

Where $\overline{N}$ is the MLI layer density expressed in [layers/cm], T_m is the average temperature between the hot T_H (space side) and cold T_C (tank side) sides of the MLI, N_s is the number of radiative shields, ε_{in} is the inner emissivity of the shields, σ is the Stefan-Boltzmann constant ($5.67x10^{-8}\ W/m^2K^4$), and P^* is the pressure between the insulation layers as a function of the position x and local temperature T. The constants a, b, and c, together with the exponents m and n, are derived from the particular insulation system and interstitial gas, therefore they should be carefully selected in order to get the most accurate MLI thermal performance estimation. Many authors in literature, like [36] and [11] proved that there is a good agreement in terms of heat leak between the traditional layer-by-layer and the Lockheed model.

Multi layer insulation can be placed both on the spacecraft body or on separate components which have the role to put specific areas in the shadow. This second application is also called Sun-shield, and it is very popular among the passive insulation systems that are currently used for space applications. Sun-shields can be shaped in various forms depending on their function and the components that they have to shade. An example of this technology is given in Figure 2.4, where the James Webb Space Telescope is shown together with its 5 Kapton layers fully deployed Sun-shield.

Figure 2.4: James Webb Space Telescope Kapton Sun-shield, courtesy of NASA.

The optical properties of MLI coatings mainly depend on the employed materials. Typical values in the solar spectrum can vary from 0.30 up to 0.80 for the emissivity, and from 0.10 up to 0.45 for the absorptivity [32].

The most traditional structure of an MLI blanket is the Uniform Density MLI configuration (UDMLI). This term is used to indicate MLI insulation structures with a single layers density distribution (N^*). In other words, this means that all the reflector layers forming the MLI structure are equally spaced from each other, with their distance specified by the density value itself.

On the other hand, literature has shown the possibility to vary the MLI layer density distribution within the same insulation structure in order to gain advantages in terms of thermal performance. This design solution is called Variable Density MLI and it has been widely studied in literature. According to [37], the main function of VDMLI is to provide more layers in the warmer (outer) regions of the insulation blanket, and fewer layers in the colder (inner) regions where blocking radiation becomes less important.

[38] experimentally evaluated a VDMLI system formed by three different layers densities sectors, concluding that the variable density helped reducing the insulation mass while improving the thermal performance, thanks to the reduced conduction effects that result from using fewer reflector layers.

2.3.2. Foam Insulation

According to [17], the low thermal conductivity of MLI systems is mainly due to the venting of gases from the interstitial areas between each foil. Therefore, in presence of atmospheric environments, the performance of MLI quickly degrades due to the increased contribution of gas conduction.

For this reason, MLI is usually combined with other passive insulation system specifically designed for in-atmosphere applications. The working principle of these systems consists in creating small volumes in the insulation structure to trap gas particles in order to eliminate conductive heat transfer. The materials employed for these systems are characterized by low conductivities to limit conduction as well.

Several in-atmosphere insulation systems have been proposed by [17], among which foam insulation is worth mentioning.

In particular, Spray-on Foam Insulation (SOFI) would be sprayed on the tank wall and plays a major role in the atmospheric pressure state of every mission, and when conduction is the main way of heat transfer, thus when the spacecraft is still on the ground. Once the system has been placed in orbit, that is in a vacuum environment where radiation is the main heat source, MLI would take over [39].
SOFI systems are generally produced from two-part mixtures of polyisocyanurate or polyurethane materials; these materials have extremely good chemical and mechanical properties, along with the characteristic of being lightweight. The foam is a porous medium containing a great number of holes that do not allow heat to easily conduct through the surface. Figure 2.5 shows the polyuretane foam used on NASA Space Shuttle; in particular, it is possible to identify the porous nature of this type of insulation by looking at the ”high” roughness of the tank surface (Figure 2.5a).

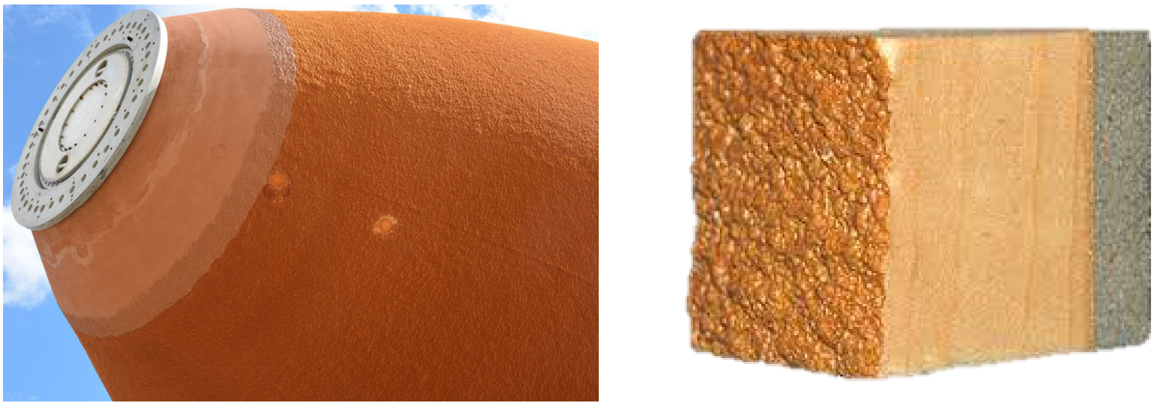

(a) Detail of foam on fuel tank. **(b)** Fuel tank cross section.

Figure 2.5: Spray-on Foam Insulation on NASA Space Shuttle Fuel tank (courtesy of NASA).

The main role of SOFI is to protect the cryogenic tank from the atmospheric thermal environment of a launch vehicle, which is subject to, among other factors, moisture, aerodynamic heating, aerodynamic and acoustic loads, and mechanical loads. Given all these sources of thermal and mechanical stresses, SOFI systems are generally intended for one-time use vehicle tanks [40].

Foams are expected to cover the whole tank surface in order to properly function. Therefore, the bigger the surface to be covered, the heavier is the mass penalty introduced by the foam. For this reason, foams, and more in general in-atmosphere insulation, are employed only when passage through atmospheric environments are necessary, for example in case of rocket stages, landers, or probes.
In case of orbit propellant depots, which are designed to work for in-orbit environments only, foam insulation can be removed to save on system mass by assembling the depot on Earth and filling it with the cryogen only once it is in orbit [15]. This indeed results in a lighter tank insulation structure.

2.3.3. Zero Boil Off (ZBO) systems

For missions longer than one year, technologies that are able to completely eliminate the propellant boil-off are being considered: the zero boil-off (ZBO) performance is usually achieved by using a combination of passive and active thermal control systems. According to [19], zero boil-off involves the use of a cryocooler/radiator system to reject the cryogenic tank heat leaks so that both boil-off and the necessity to vent it to avoid tank over-pressure are not needed.
However, while the ZBO approach has been proven to be successful in case of cryogenics with high boiling points (e.g. 90 K for LOX), no current technology that can operate at LH2 temperatures (20 K) exists yet [9]. NASA has been recently investing in 20 K (hydrogen) and 90 K (oxygen) cryocooler technologies, and even if the results are promising for the 20 W-20 K cryocooler, its dimensions still remain strongly linked to the vehicle's heat load. For example, for an aluminum vehicle structure, heat leakage can easily go over 1000 Watts, requiring unfeasible cryocooler sizes [41].
For the above mentioned reasons, another type of thermal control system has been identified: instead of focusing on zero boil-off technologies, some systems allow a small percentage of boil-off that to be

used mainly for tank cooling, and when possible also for power production and support to other on-board systems. Among these, Vapour Cooled Shields (VCS) are worth mentioning and are described in more detail later in this chapter.

2.4. Tank pressurization, venting and Vapor Cooled Shields

According to [1], the objective of a feed system is to provide a pressure gradient that allows the propellants to move from the storage tank to the thrust chamber. In order to make this happen, a proper tank pressurization system that is able to provide the desired feed pressure is required. These systems can be divided into two main groups: pressurized gas and pumped feed systems. In particular, gas pressurization can be achieved by either using an inert gas, or the evaporated propellant vapors. The described cases are called respectively heterogeneous and autogenous pressurization systems.

According to [42], the use of autogenous pressurization is already common for on ground operations of hydrogen cryogenic tanks. The same does not hold for LOX operations, which still rely on helium as inert pressurization gas. However, helium systems add mass and complexity to any storage system, not to mention that in case of long-term storage of a helium-pressurized cryogenic tank, a helium supply system is needed to guarantee the desired pressure in the tank over time. For this reason, future developments of autogenous pressurization systems, both for LH2 and LOX storage, are fundamental. According to [43], with systems using easily vaporized propellants such as hydrogen, oxygen, or light hydrocarbons, autogenous pressurization could be beneficially applied to long-term missions.

2.4.1. Propellant boiling

Unless the orbital propellant depot also acts as a rocket stage, no engine is connected to the storage tank. This means that the storage of the propellant could indeed be achieved by simply keeping the liquid and ullage in equilibrium at saturation conditions at a specific initial temperature (or pressure) [44].

This however means that the moment any heat leak penetrates the tank, the cryogen starts to boil. As the tank is a closed system, propellant evaporation causes the tank pressure to rise. Therefore, a pressure control system is needed to make sure that the tank pressure does not exceed a specific limit set by the designer to prevent structure failures due to over-pressure.

A schematic of the mean heat and mass exchange processes involved in a LH2 cryogenic tank is shown in Figure 2.6. In particular, $q_{wall \to gas}$ and $q_{wall \to liquid}$ represent the heat fluxes leaking into the tank from the insulation system, while $q_{liquid \to vapor}$ is the heat flux between the bulk liquid and the ullage.

As for the mass fluxes, two of them are related to the boiling of the liquid, namely the boil-off $\dot{m}_{boiloff}$ and venting $\dot{m}_{venting}$ rate. Moreover, a continuous interchange of particles between the vapor and liquid phase happens at the liquid-vapor interface ($\dot{m}_{evap}$) as a consequence of the saturation equilibrium conditions [45]. In particular, this effect becomes important in case the tank is subjected to important pressure variations, for example as a consequence of ullage venting, as it is explained in more detail in the next section.

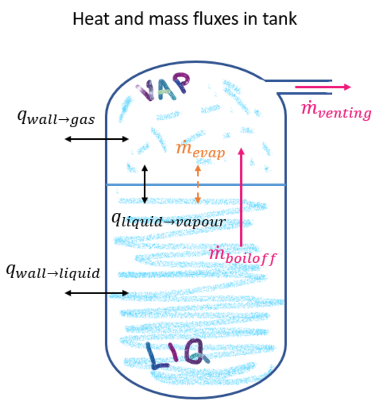

Figure 2.6: Heat and mass exchange processes in cryogenic tank.

For a system like the one shown in Figure 2.6, any heat leak into the tank results in boiling of the liquid. Therefore, the cryogenic fluid boil-off rate ($\dot{m}_{\text{boiloff}}$) can be computed using the total heat leak into the bulk liquid $Q_{leak,liq}$ $[J/s]$ and the latent heat of vaporization L_{vap} $[J/kg]$ at the cryogen's saturation condition [11]:

$$\dot{m}_{\text{boil-off}} = \frac{Q_{\text{leak,liq}}}{L_{\text{vap}}} \tag{2.8}$$

The value of latent heat of vaporization of a substance, as well as other fluid-related properties, can be retrieved from dedicated databases. Several thermophysical property libraries have been identified by [46], with particular attention to REFPROP (REference FLuid Properties) [47], which is a computer program for the calculation of thermodynamic and transport properties of fluids. The only downside of REFPROP is that it is not open-source.
The best option among the state-of-the-art in open-source fluid thermophysical libraries is the CoolProp library [46]. Analogously to REFPROP, CoolProp is a computer program with an interface that can be adapted to different programming languages, such as Microsoft Excel, Labview, Matlab, and Python. Being it open-source, it comes with some limitations, like a restricted selection of fluids and the impossibility to handle mixtures. Nevertheless, CoolProp still provides thermophysical data for 110 fluids, including hydrogen, which is of interest to this work.

2.4.2. Venting process

The venting process starts as soon as the tank ullage pressure has reached the upper design limit. This can be handled in several ways, like through the use of valves or more complex systems like the Thermodynamic Venting System (TVS) [48]. Being this work more focused on the heat exchange processes in the tank, rather than the types of venting systems, the latter have been chosen to not be investigated further.
A schematic of the tank venting mechanism for a liquid hydrogen cryogenic tank is shown in Figure 2.7. This process description is indeed valid for other substances as well.

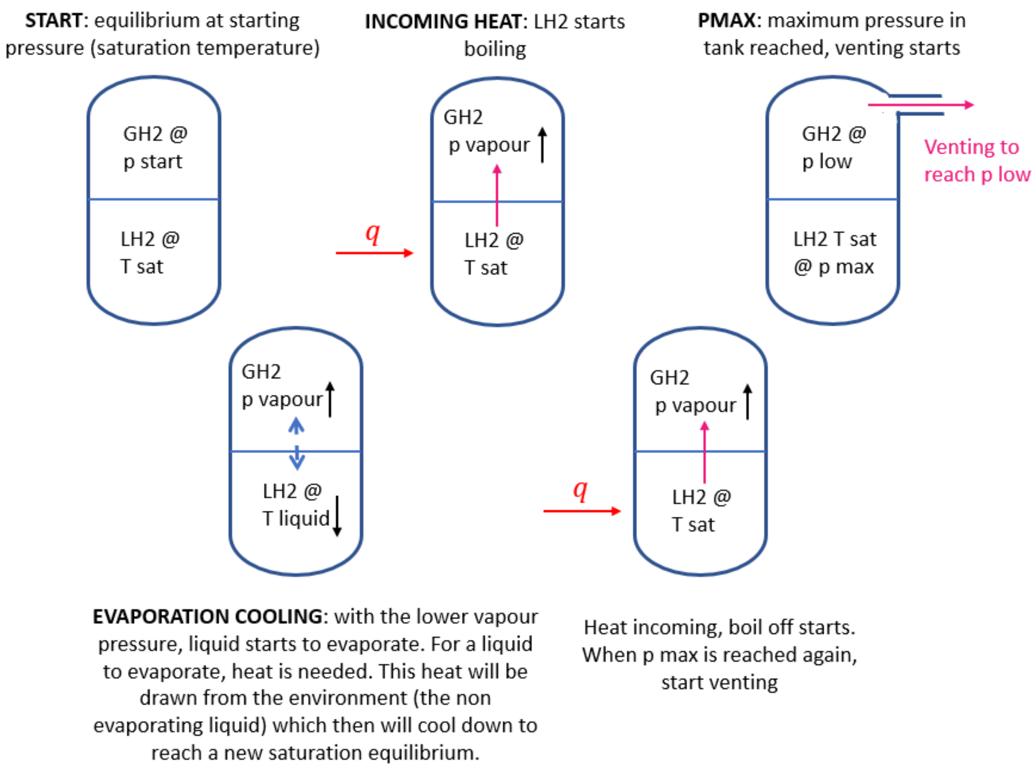

Figure 2.7: Venting process for cryogenic LH2 tank.

In the process shown in Figure 2.7, the tank starts in equilibrium at saturation conditions, which are altered after heat penetrates into the tank structure (here represented by the flux q). As a consequence, boiling of the liquid starts, and the tank pressure and temperature adjust to the new equilibrium conditions, always at saturation. When a maximum value for the pressure in the ullage is reached (p_{max}), some of the vapor is vented over-board until a desired pressure value is reached (here called p_{low}). As a consequence of the pressure reduction, some of the liquid from the liquid-vapor interface evaporates to reach a new saturation equilibrium, cooling down in the process. This process is called evaporative cooling [49].
The above-described process starts again every time the maximum pressure in the tank is reached.

2.4.3. Vapor Cooled Shields

Vapour Cooled Shields (VCS) reduce noticeably the amount of boil-off by making use of the sensible heat of the boil-off vapor. Considering for example a Liquid Hydrogen tank, the vapor is allowed to cool down the outer surface of the MLI blanket before being vented overboard.
The VCS structure consists in a coil of tubes attached to one or more metal shields. The boiled-off vapor from the tank is then sent through the tubes before being vented overboard. This generates a radiation shield which is temperature-controlled by the vented vapor itself, being it at saturation conditions inside the tank [17]. A representation of this structure is shown in Figure 2.8.

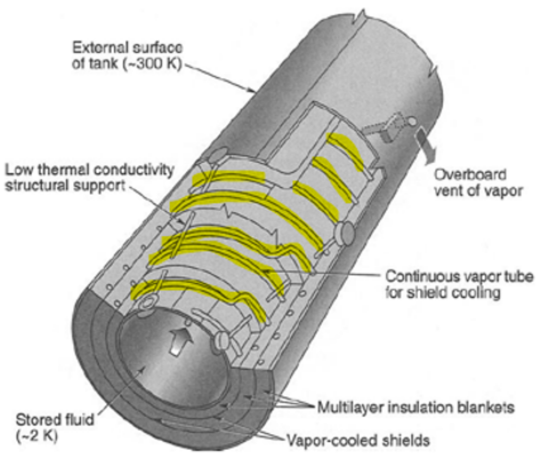

Figure 2.8: Cryogenic tank equipped with vapor cooled shields [17].

A comparison between simple H2 venting and the VCS has been performed by [9], leading to the conclusion that the use of VCS reduces boil-off of a factor of about 6.5 (for a fixed heat load) compared to simple H2 venting.
[50] studied the concept of combining VCS with thermal insulation, showing that a vapour cooled shielded LH2 tank experienced a boil-off reduction up to 62 % with respect to a non-shielded one.
[51] also experimentally investigated the performance of MLI/VCS systems, by comparing them to MLI only, and they showed that VCS improves the thermal performance of the insulation structure, with an heat flux reduction up to 19.6 % in case of a liquid nitrogen (LN2) tank.

According to [52], two VCS layouts resulted from an optimization study: the independent and the integrated configuration. These layouts are both shown in Figure 4.10 for the hydrolox mixture case, where the system is formed by one hydrogen and one oxygen tank both stored at cryogenic temperatures.

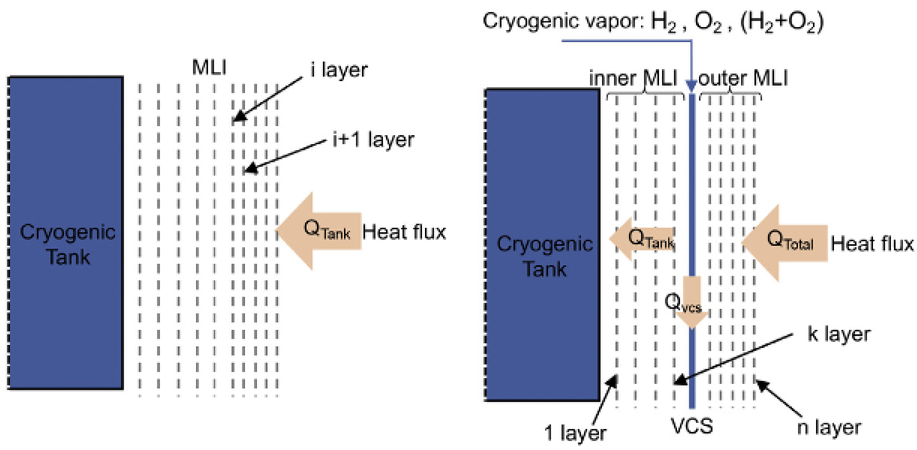

Figure 2.9: Vapor Cooled Shields layout options and comparison with simple MLI system [23].

In case of the independent configuration, both cryogens are used to cool down their own tank, so LH2 with H2 vapor and LOX with O2 vapor. On the other hand, in case of the integral layout, there is the possibility to also use the hydrogen vapors to cool down the oxygen tank. This is possible given the difference in storage temperature between hydrogen (20 K at 1 bar) and oxygen (90 K at 1 bar): even when hydrogen vapors are used to cool down the LH2 tank first, their temperature is still low enough to be able to properly shield the LOX tank. It comes without saying that the opposite is not possible, that is vapor cooled shielding of the LH2 tank can only be achieved using hydrogen vapors.

Several approaches to the modelling of the VCS have been proposed in literature. Nevertheless, all the models share the same heat balance as starting point for the analysis. From Figure 4.10, this balance is written as:

$$Q_{\text{total}} = Q_{\text{VCS}} + Q_{\text{tank}} \tag{2.9}$$

Thus, when the shield is active, the total heat leak into the cryogenic tank Q_{tot} is reduced by the quantity of heat that the shield is able to remove from the system Q_{VCS}. Being the heat exchange in the VCS between a fluid (vented vapors) and a solid (metal tubes and shield), this amount can be calculated using the convective heat transfer equation [23]:

$$Q_{\text{VCS}} = h_{\text{VCS}} A_{\text{cont}} (T_{\text{VCS}} - \overline{T}_F) \tag{2.10}$$

Where A_{cont} refers to the available heat exchange area, and T_{VCS} and $\overline{T}_F$ respectively are the temperature of the VCS shield and the average temperature of the fluid in the VCS tube.
In order to properly model the heat exchange, an accurate estimation of the convective heat transfer coefficient h_{VCS} is needed. This is done using Equation 2.11:

$$h_{\text{VCS}} = \frac{\text{Nu}_{\text{vap}}\, k_{\text{vap}}}{d_{\text{VCS}}} \tag{2.11}$$

Where k_{vap} is the thermal conductivity of the vented vapor, d_{VCS} is the VCS tube diameter, and Nu_{vap} is the Nusselt number of the vented vapor, and it is depending on the flow conditions in the tube. In particular, according to [22]:

$$\begin{aligned} &\text{For Re} < 1960: && \text{Nu} = 3.66 \\ &\text{For } 1960 < \text{Re} < 6420: && \text{Nu} = 0.116(\text{Re}^{2/3} - 125.0)\,\text{Pr}^{0.4} \\ &\text{For Re} > 6420: && \text{Nu} = 0.023\,\text{Re}^{0.8}\,\text{Pr}^{0.4} \end{aligned} \tag{2.12}$$

Where $Pr = C_{p,VCS}\mu_{VCS}/k_{VCS}$ is the vented vapor Prandtl number, while the vented vapor Reynolds number Re is given by Equation 2.13 [22]:

$$\text{Re} = \frac{4\dot{m}_{\text{venting}}}{\mu_{\text{vap}} \pi d_{\text{VCS}}} \tag{2.13}$$

Where μ_{vap} is the dynamic viscosity of the vented vapor, and $\dot{m}_{venting}$ is the ullage venting rate.

2.5. Microgravity and propellant settling

Orbital propellant depots must be designed to allow long-term storage of cryogenic propellants in orbit. According [9], ”long-term” is used to indicate storage durations that range from months to years.
It has been shown that the depot external thermal environment plays a big role in the design of these systems. However, there is another important factor that needs to be considered, that is microgravity. Microgravity (also called zero-gravity) refers to a condition where objects seem weightless, or more correctly, characterized by very small g-forces. In particular, according to [9], the maximum value of g in microgravity is a linear function of the distance from Earth: $|\mathbf{g}| \simeq 3g_0 R_e/R_{\text{orbit}}$. For example, for an object in LEO: $|\mathbf{g}| \simeq 10^{-6} g_0$. In such a reduced gravity environment, the vapor bubbles formed from propellant boil-off do not quickly reach the ullage space as in normal Earth gravity conditions. On the contrary, they slowly grow into bigger vapor pockets, generating complex structures which behaviour is difficult to control [9]. Moreover, heat transfer mechanisms are also altered: low g-forces significantly reduce the effects of gravity-driven free convection (described in subsection 2.2.2), interfering with the thermal balancing between liquid and vapor in the tank [53].

The above-mentioned reasons make zero-g propellant handling a challenge, on which, according to [53], technologies are still at a low Technology Readiness Level (TRL). However, several alternatives for cryogenic fluid manipulation in microgravity have been proposed, which can be all included into the category of ”settled propellant handling” [53]: propulsive, inertial, gravity gradient, and electromagnetic settling. Among these, propulsive settling is the most mature technique, and has already been used for the Saturn V third stage, where the cryogenic vented vapor from the tank was used to provide a slight acceleration (about 10^{-4} to 10^{-5} g) in the form of thrust to the spacecraft, forcing the liquid to settle on one end of the tank during the orbital coasting [9]. This technique allowed to have gas-free liquid at the tank outlet to guarantee a successful engine restart. The settled propellant condition in the tank is shown in Figure 2.10.

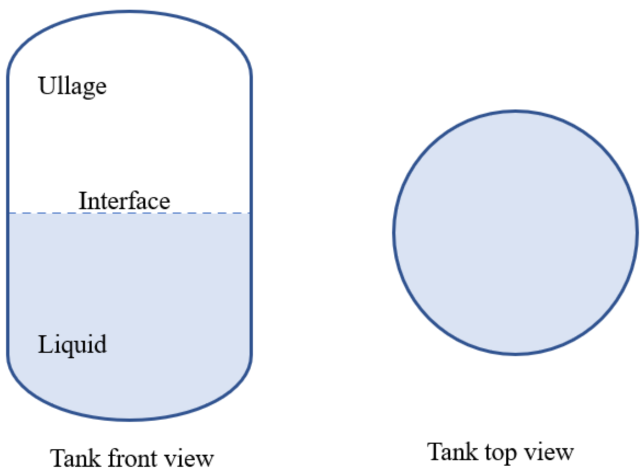

Figure 2.10: Settled propellant condition in tank.

In subsection 2.2.4, the thermal mathematical model (TMM) as a mean to perform a thermal performance study of the depot has been introduced. This is a solution already adopted by other researchers in this field: for example [45] and [54]. In particular, the former developed TankSIM, a TMM that models the interactions between several nodes, each one representing a different interface, such as ullage-tank wall, liquid-tank wall, ullage-liquid, or tank-environment. However, TankSIM is a single-node model, meaning that every interface is always represented by a single isothermal node, regardless the dimensions of the tank.
Even if the single-node model has proven to have a reasonable accuracy, [54] stressed the importance of dividing the tank body in multiple nodes that would represent the liquid and the ullage at different fill

levels. This TMM, also called multi-node model, would in fact predict the heat load distribution around the tank with an increased accuracy with respect to the single-node case. In particular, a multi-node model would be able not only to separately represent the tank area wetted by the liquid and the vapor, but it would also allow to monitor the changes of this area over time. For example, when the cryogenic propellant is stored for long times, the liquid level gradually reduces due to the boil-off, thus increasing the ullage-tank wall interface area (and reducing the liquid-tank wall as a consequence). This effect can be easily modelled with a multi-nodal network, unlike single-node models, which would operate with fixed tank fill levels[4].

2.6. Original and Extended Boil-off tool

The Boil-off tool is a tank sizing computer program that allows to study the effectiveness of the thermal insulation of a cryogenic tank by quantifying the amount of boil-off that occurs during a pre-defined mission duration, and the mass that needs to be allocated for the thermal control system. The first version of this tool has been developed by Borst [24] to solve a thermal mathematical model (subsection 2.2.4) of a cryogenic propellant tank in space.
Based on the literature research just performed, several extensions for the Boil-off tool are proposed to adapt it to the case study of orbital propellant depots. A list of the extensions of the original features of the tool is shown in Table 2.1.

	Borst tool	**Extension**	**Reason**
Nodal structure	Fixed number of thermal nodes (12)	Number of thermal nodes selected by user	Done to allow flexibility in the thermal mathematical model definition (see subsection 2.2.4)
Thermal environment	Simple model based on solar incidence angle	Thermal fluxes from ESATAN-TMS	To account for the effect of many parameters (i.e. attitude, orbit, eclipses) (see subsection 2.1.4)
Fluid properties definition	Manually taken by the user from the NIST Chemistry WebBook [55]	Automatically taken from the CoolProp library [46]	Broader selection of fluid properties and no actions needed from the user (see subsection 2.4.1)
Thermal control design options	MLI, SOFI, cryocoolers	Addition of VDMLI and VCS	Expected improvement of thermal performance (see subsection 2.3.1 and subsection 2.4.3)
Tank pressurization	Heterogenous	Autogenous	Preferred choice for orbital propellant depots (see section 2.4)
Propellant conditions	Settled	Settled	-

Table 2.1: Boil-off tool original and added features.

The original Boil-off tool is written in the Cython[5] programming language [57], which is used to speed up critical parts of the code that, if written in pure Python, may take a very long time to run. The boil-off

[4]The tank fill level is defined as the ratio between the volume of the liquid in the tank and the total tank internal volume (fill level = $V_{\text{liquid}}/V_{\text{tot}}$)

[5]For [56]: "Cython is a Python language extension that allows explicit type declarations and it is compiled directly to C"; that is, this language allows the user to benefit from the C speed and improved performance, while keeping the simplicity of the Python language.

program is based on iterating schemes that are able to evaluate different thermal control options based on the user choice. This indeed would result in a very computationally expensive program that could be improved in efficiency with the use of Cython. Therefore, this language is chosen to continue with on the Boil-off tool extensions, both for speed reasons and compatibility with the original version of the tool. Guidelines on the use of Cython and the Boil-off tool are given in Appendix B.

3
Methodology

The approach taken in this work consists in the development of a propellant depot sizing model (the "Boil-off tool") that allows determining the effect of different thermal control design options, thermal environments, and depot configurations for varying mission duration.
In particular, when setting up a tool for the thermal performance simulation of a depot, two main aspects have to be taken into account: the external thermal environment definition, which is responsible of the surface temperature of the spacecraft, and the tank sizing and thermal model. For this work, the ESATAN Thermal Modelling Suite is selected to model the former, while the sizing and thermal performance estimation is done by a custom-developed tool. In particular, this tool is not designed from scratch, on the contrary it is the result of several design iterations performed on a previously developed version, which is called here the "original Boil-off tool" [24].
This chapter describes the methodology followed to implement the tool extensions identified in the Literature review chapter, which are summarized in Table 2.1.

3.1. Space thermal environment models

The literature research performed has shown how important it is to define the proper thermal environment the depot is in. Indeed, a correct estimation of the incoming heat loads on the depot is important when assessing its thermal performance.
The amount of heat absorbed by the depot depends on several parameters, like its distance from Earth and from the Sun, the depot geometry, orientation and position in orbit, and the optical properties of the depot coating material. Furthermore, the amount of heat reaching the depot can be also influenced by the presence of other objects, like for example in case of stations formed by many tanks grouped together.

In this section, a simple tank environment model is described to improve understanding of the single tank depot case. After that, a more versatile approach taken in this work to model the depot thermal environment is shown.

3.1.1. Simple single tank model

A simple single tank thermal environment model based on the solar incidence angle ϕ [1] has been proposed by Borst [24]. According to this model, the absorbed solar radiation by each node is given by:

$$Q_{\text{solar}} = \alpha \cdot S \cdot max(cos(\phi_M), 0) \cdot A_{\text{frontal}} \tag{3.1}$$

Where α is the (solar) absorptivity of the tank on its outside as determined by the tank material or the optical properties of the material covering the tank, like coatings or MLI. S is the solar constant, usually taken as $1367\ W/m^2$ (see subsection 2.1.1), ϕ_M is the solar incidence angle ϕ after the application of the model shown in Figure 3.1, and A_{frontal} is the frontal area of the node considered. The maximum

[1] The solar incidence angle is defined as the angle between the Sun's rays and the normal on a surface.

function for the cosine is used to make sure that in case of negative values, corresponding to the tank side in shadow, the heat load is set to zero.

The simple tank model is shown in Figure 3.1 for $\phi = 180°$, which corresponds to the solar incidence angle of one of the worst case scenarios for the propellant tank, that is with one of its sides fully illuminated by the Sun.

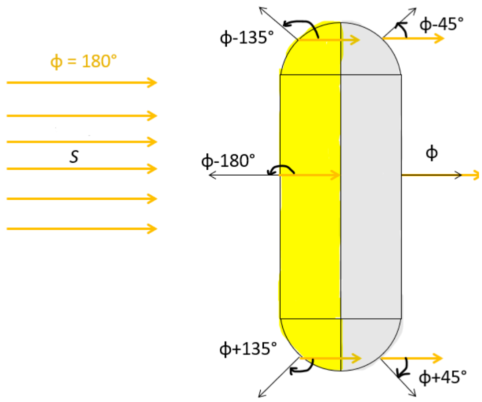

Figure 3.1: Simple thermal model illustration for solar fluxes incoming on tank (yellow: sunlit, grey: shadow).

It has to be noted that the model described above works well for cases characterized by constant fluxes, and it can also be extended to cases with variable fluxes by considering values integrals over time. Furthermore, Figure 3.1 shows only the application of the model to solar fluxes, however the same procedure can be followed for albedo and planetary radiation using a proper incidence angle.

3.1.2. ESATAN-TMS tank model

In subsection 2.1.4 a powerful software for the thermal environment definition of a depot placed in orbit is introduced. This is called ESATAN-TMS, and it is considered more versatile than the simple thermal model because it automatically determines the incidence angles based on the chosen depot attitude, and calculates the intensity of solar, albedo and planetary fluxes, and their variation over time. Furthermore, this software also takes into account the eclipse phase of the depot (if any) during the orbit, and it allows to determine the heat fluxes on the depot also in case of more complex geometries.

The single tank depot introduced in the previous section has been reproduced using ESATAN-TMS and it is shown in Figure 3.2.

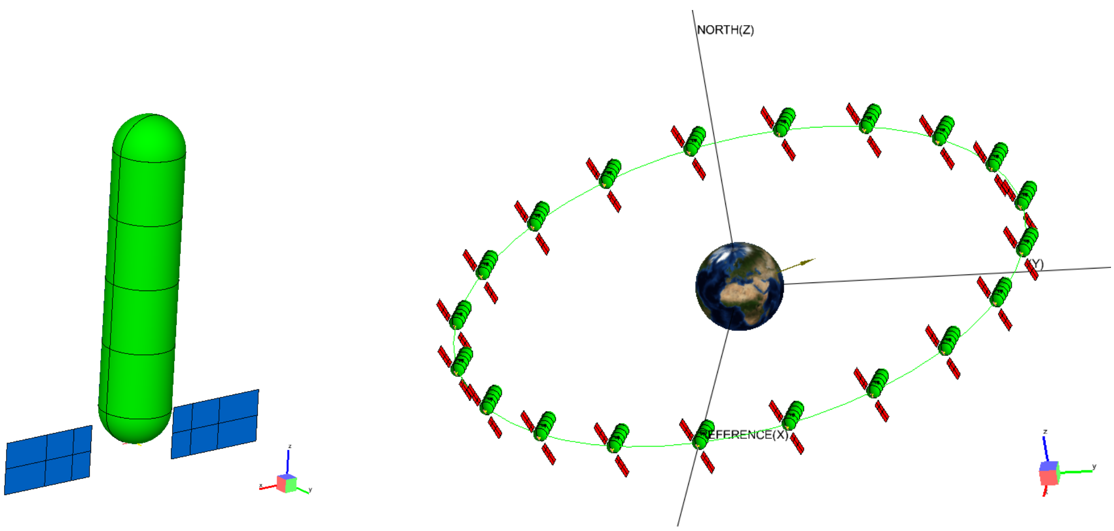

Figure 3.2: ESATAN-TMS single tank model and orbit display, tank left side to Sun. Sun position is indicated by the yellow vector in the figure.

From the left of Figure 3.2 it is possible to notice that ESATAN-TMS allows to divide the tank geometry into a custom defined number of sections. This is usually done to improve the accuracy of the results from the radiative analysis (more details on the selection of the total number of sections are found in section 4.1). In fact, ESATAN-TMS gives as output a file containing all the external fluxes incoming on each section, for a user-specified number of orbital positions, therefore the bigger the number of sections, the more possible is to record different heat load intensities related to the depot geometry.

A Python-based program has been developed to convert the output data given by ESATAN-TMS into compatible inputs for the boil-off model, providing an external tank environment definition which is geometry and time dependant.
In particular, the model is able to build a matrix storing the thermal fluxes on each section the tank is divided into. A schematic of the matrix generation model is shown in Figure 3.3.

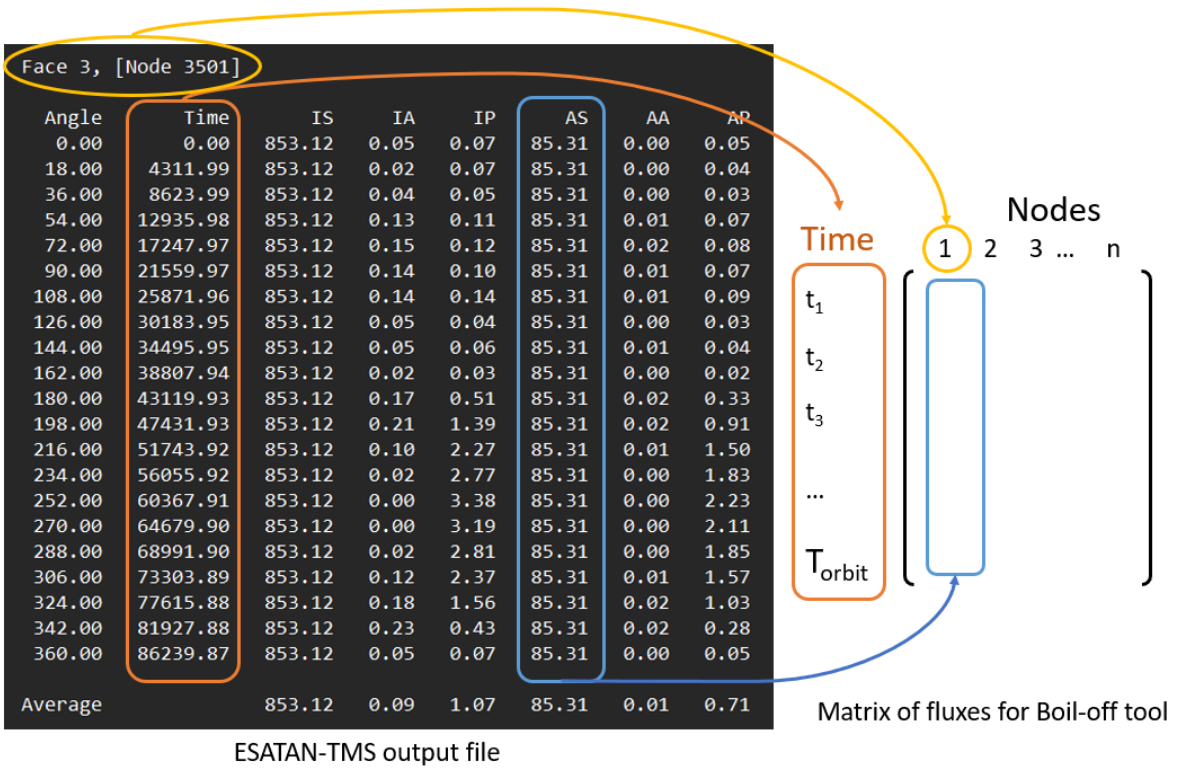
Face 3, [Node 3501]

Angle	Time	IS	IA	IP	AS	AA	AP
0.00	0.00	853.12	0.05	0.07	85.31	0.00	0.05
18.00	4311.99	853.12	0.02	0.07	85.31	0.00	0.04
36.00	8623.99	853.12	0.04	0.05	85.31	0.00	0.03
54.00	12935.98	853.12	0.13	0.11	85.31	0.01	0.07
72.00	17247.97	853.12	0.15	0.12	85.31	0.02	0.08
90.00	21559.97	853.12	0.14	0.10	85.31	0.01	0.07
108.00	25871.96	853.12	0.14	0.14	85.31	0.01	0.09
126.00	30183.95	853.12	0.05	0.04	85.31	0.00	0.03
144.00	34495.95	853.12	0.05	0.06	85.31	0.01	0.04
162.00	38807.94	853.12	0.02	0.03	85.31	0.00	0.02
180.00	43119.93	853.12	0.17	0.51	85.31	0.02	0.33
198.00	47431.93	853.12	0.21	1.39	85.31	0.02	0.91
216.00	51743.92	853.12	0.10	2.27	85.31	0.01	1.50
234.00	56055.92	853.12	0.02	2.77	85.31	0.00	1.83
252.00	60367.91	853.12	0.00	3.38	85.31	0.00	2.23
270.00	64679.90	853.12	0.00	3.19	85.31	0.00	2.11
288.00	68991.90	853.12	0.02	2.81	85.31	0.00	1.85
306.00	73303.89	853.12	0.12	2.37	85.31	0.01	1.57
324.00	77615.88	853.12	0.18	1.56	85.31	0.02	1.03
342.00	81927.88	853.12	0.23	0.43	85.31	0.02	0.28
360.00	86239.87	853.12	0.05	0.07	85.31	0.00	0.05
Average		853.12	0.09	1.07	85.31	0.01	0.71

Figure 3.3: Python-based ESATAN conversion: fluxes matrix generation. Optical properties used (MLI) [32]: $\alpha = 0.10, \varepsilon_{IR} = 0.66$.

This picture shows the fluxes acquisition process relative to a single section of the ESATAN-TMS depot model. Each row in the matrix (orange in the figure) corresponds to the time that the depot takes from the start of the orbit to reach a specific position (indicated by the value "Angle"). As for the columns (yellow in the figure), each one corresponds to a specific tank section (also called node).
It is up to the user to choose which kind of thermal flux to save in the matrix, which can be Solar (S), Albedo (A), or Planetary (P). The starting letters I and A stand respectively for "Incoming" or "Absorbed" fluxes. In this example, the acquired values (blue in the figure) are the ones corresponding to the "Absorbed Solar fluxes", hence the AS acronym. It is of course possible to create multiple matrices in case all the fluxes need to be saved and exported to the Boil-off tool. More details on the matrix generation process can be found in Appendix B.2.1.

The absorbed fluxes given by ESATAN-TMS are then converted into their respective heat loads. This is done by the Boil-off tool, which calculates the absorbing surface area of each tank section and multiplies it by the heat fluxes provided in the thermal environment model. Afterwards, the following heat balance is performed:

$$
\begin{aligned}
Q_{\text{in}} &= Q_{\text{out}} \\
Q_{\text{abs}} + P_{\text{diss}} &= Q_{\text{emit}}
\end{aligned}
\tag{3.2}
$$

Assuming that there is no internal power generation ($P_{\text{diss}} = 0$), combining the heat balance in Equation 3.2 with the thermal radiation equation (3.3) allows to compute the depot surface temperature (also called hot temperature T_H).

$$Q_{\text{emit}} = \varepsilon_{\text{IR}} \sigma A_{\text{emit}} T_H^4 \tag{3.3}$$

Where ε_{IR} is the infra-red emissivity of the chosen tank coating material, σ is the Stefan-Boltzmann constant, and A_{emit} is the depot emitting surface area.

3.2. Sizing and thermal analysis tool

Following the characterization of the thermal environment, the thermal performance of the tank can be determined. This section describes the methodology followed and the design choices made to develop the Boil-off tool.

3.2.1. Multi-nodal thermal analysis

The Boil-off tool is designed to study the propellant in the tank under settled conditions (see section 2.5). This means that there is a net separation between ullage and liquid, which are positioned on opposite ends of the tank and have a liquid-vapor interface corresponding to a circle with a radius equal to the tank internal radius (see Figure 2.10). In case of settled propellant, the liquid and ullage volume can be easily computed using the tank fill level, which in its turn varies over time depending on the amount of propellant boil-off in the tank.

In section 2.5, multi-nodal thermal models have been identified as the best option to accurately model the heat exchange in the cryogenic tank, since they allow to account for tank fill level variations over time. For this reason, also the Boil-off tool has been developed as a multi-nodal thermal model.
In particular, the Boil-off tool tank has been split along its longitudinal direction into six sections, each one corresponding to a specific fill level ratio as shown in Figure 3.4.

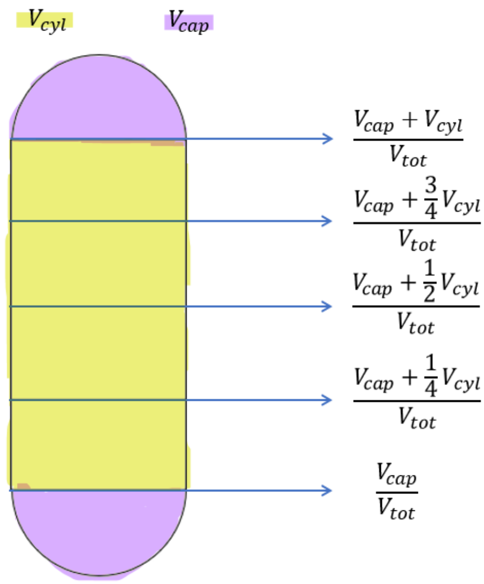

Figure 3.4: Tank fill level for different tank sections. V_{cap}= volume of a single end-cap, V_{cyl} = volume of cylindrical body, V_{tot} = total tank volume

A sensitivity analysis performed by Borst has shown that the solution calculated by the Boil-off tool depends on the number of sections the tank is divided into, with an accuracy that is increasing with the number of sections [24].
For the analysis presented in this work, the same number of sections selected by Borst (shown in Figure 3.4) is used. Although this has not been proven to be the optimum amount of sections, Borst

has shown that this arrangement represents a good compromise between accuracy of heat flow values and computational time (which also increases with the number of sections).

3.2.2. Tank nodal structure

Combining the multi-nodal model shown in Figure 3.4 with the previously introduced thermal environment model (Figure 3.1) results in the tank nodal structure shown on the left of Figure 3.5.
In particular, the complete Boil-off tool thermal network is developed in two different dimensions: a main nodal network to take into account of the effects of fill level and thermal radiation variations, and a sub-nodal network that looks at the heat load and temperature distribution through the insulation structure as a consequence of the incoming external heat fluxes.
In practice, the main nodal network is generated by dividing the entire tank structure into multiple sections (left of Figure 3.5), while the sub-nodal network comes from further dividing each tank node based on the thermal insulation structure (right of Figure 3.5).

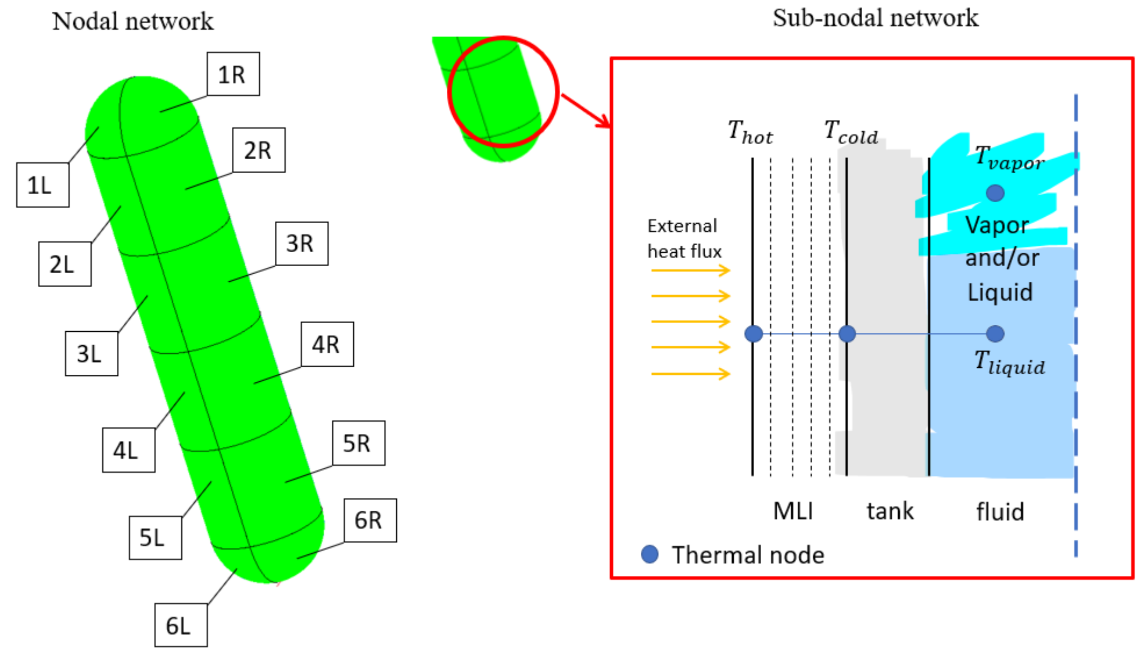

Figure 3.5: Boil-off model tank nodal network (left) and sub-nodal network (right) division.

The main nodal partition concerns the entire tank structure. In this regard, it is up to the user to decide the number of sections the tank is divided into, based on the desired accuracy. As already stated in subsection 3.2.1, for a heat-leak focused analysis like the present one, the same number of nodes selected by [24] is used, which is equal to 12. In particular, the tank is split along its axis into two sides (see left side of Figure 3.5): the left part (L) and right part (R), to be able to separately analyse the sunlit and shadow tank areas.
It has to be noted that the nodes are assumed to be isothermal, meaning that the temperature does not change within the same node (see subsection 2.2.4). Therefore, in case one would be more interested in detailing the thermal stratification of the tank, it is advised to increase the number of thermal nodes.
The sub-nodal thermal network is variable based on the type of thermal control system chosen. However, a baseline structure can be identified, and it is shown on the right of Figure 3.5: MLI blanket, tank wall, and fluid stored (further divided into bulk liquid and vapor). In this regard, the following remarks are made:

- The MLI blanket is equivalent to two thermal nodes, one to account for the hot temperature side (space side), and the other for the cold one (tank side).
- No foam between the MLI and the tank is present. The use of foam is in fact recommended only in the presence of an atmosphere (see subsection 2.3.2). The propellant depot is launched empty

and assembled in space, thus eliminating the mass penalty introduced by foams.

- No thermal node is assigned to the tank wall, meaning that its temperature is equal to the one of the cold side of the MLI. This can be assumed in this case for two main reasons. First of all, the tank wall thickness is relatively small (in the order of millimeters up to one centimeter) compared to the other insulation so that it is safe to assume that the temperature gradient through the tank thickness is negligibly small.
  Furthermore, materials used for cryogenic storage are usually metals like aluminium alloys, stainless steel and titanium, which are characterized by high thermal conductivities. Other alternatives like carbon fibers or composites have been proposed to replace metals to improve the tank performance ([58],[59]), however this mainly concerns structural matters and does not influence the thermal protection given by the tank material itself.

3.2.3. Heat balance

Using the thermal network just described, the main function of the boil-off tool is to perform an heat balance between the heat loads incoming and leaving each node, to then use the heat capacity equation to compute the respective temperature. This procedure is shown in Equation 3.4.

$$\begin{aligned} Q_{\text{net}} &= Q_{\text{N,prev}} + Q_{\text{N,next}} + Q_{\text{N,opp}} + Q_{\text{S,prev}} + Q_{\text{S,next}} \\ \frac{dT_{\text{node}}}{dt} &= \frac{Q_{\text{net}}}{MC_p} \end{aligned} \tag{3.4}$$

In particular, the forward Euler method (see Appendix A.1) is chosen to numerically solve the partial differential equations.

Each node exchanges heat with adjacent nodes (previous $Q_{\text{N,prev}}$, next $Q_{\text{N,next}}$ and opposite $Q_{\text{N,opp}}$). In addition, heat is exchanged with the adjacent sub-nodes as well, corresponding to the interactions within the insulation layers (heat from previous $Q_{\text{S,prev}}$ and next $Q_{\text{S,next}}$ sub-nodes). Once the net heat leak Q_{net} into the node is computed, the heat capacity equation is used to calculate the temperature increase. In order to do this, the heat capacity C_p and the mass M of the insulation considered have to be known.
An example of this process for the 4L node is shown in Figure 3.6.

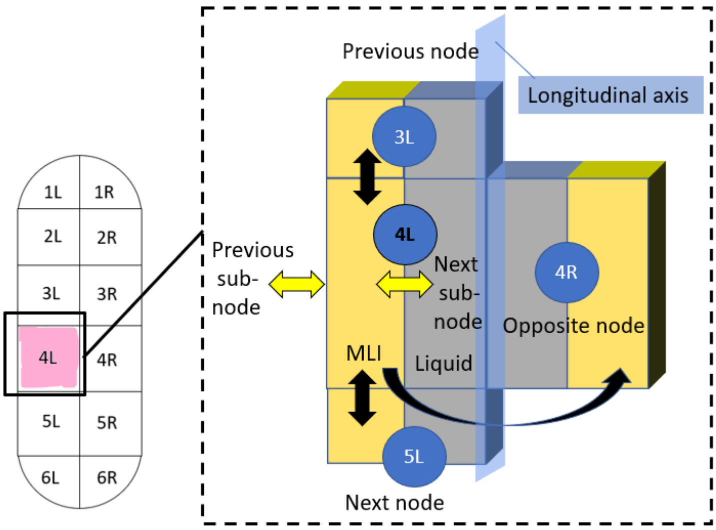

Figure 3.6: Heat balance calculation procedure for nodal and sub-nodal analysis.

For example, the MLI section of node 4L exchanges heat with the MLI sections of the previous node ($Q_{\text{N,prev}} = Q_{3L}$), the next node ($Q_{\text{N,next}} = Q_{5L}$), and the opposite node on the tank right side ($Q_{\text{N,opp}} = Q_{4R}$). Moreover, the MLI is also in contact with the outer space ($Q_{\text{S,prev}}$), which corresponds to its previous sub-node, and the fluid in the tank (dark section in Figure 3.6), corresponding to its next

sub-node ($Q_{S,next}$).
All the heat exchanges between adjacent nodes are through conduction, being the insulation type the same. On the other hand, the sub-nodal structure represents different insulation types, therefore the heat exchange is computed accordingly (either using radiation in case of MLI or convection in case of the fluid).

The complete nodal network built with the Boil-off tool to perform the analysis in this work is shown in Figure 3.7. As indicated in the legend below, different heat transfer mechanisms are identified with different line styles. Moreover, the curved lines represent the conductive link between opposite tank nodes, which are in contact because of the rotational symmetry of the cylindrical tank.
While each tank section has its own node, the bulk liquid and ullage are chosen to be represented by single nodes. This is a safe assumption to the means of this analysis, where the boil-off of the liquid, which involves the entire liquid block, is of interest (also confirmed by [60]). In case one would be focused on the tank thermal stratification, or on the micro-scale physics of the liquid itself, a proper model of the liquid and ullage system is required (an example has been given by [45]).

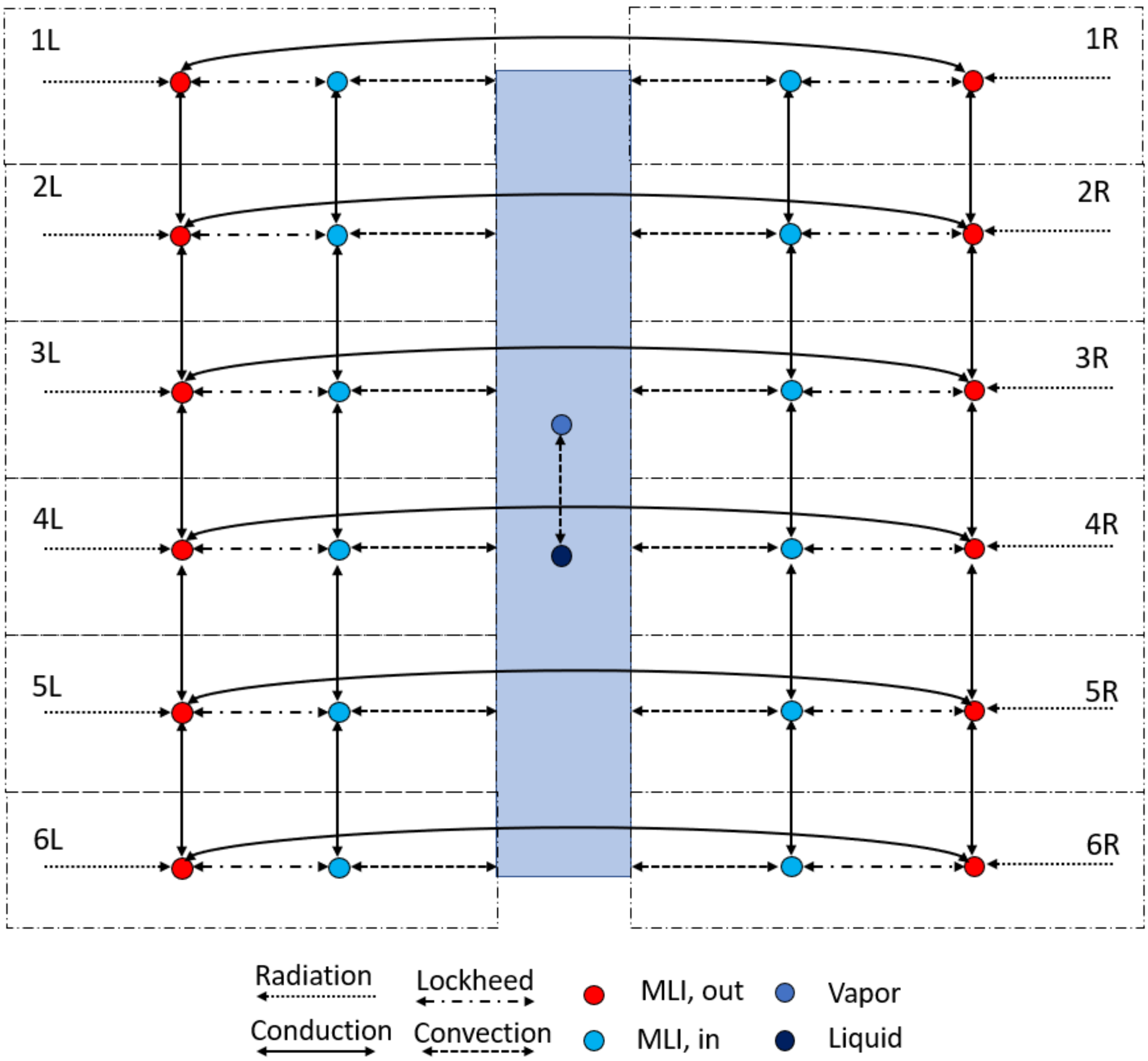

Figure 3.7: Complete tank nodal network used in the Boil-off tool.

3.3. Thermal control options modelling

This section is dedicated to the approach followed to model the different thermal control options integrated in the Boil-off tool.

3.3.1. Uniform and Variable Density Multi-Layer Insulation

Subsection 2.3.1 introduces an empirical model, called Lockheed equation, which is able to estimate the thermal performance of MLI. In particular, the Lockheed model requires several empirical constants to be tuned-in depending on the materials and interstitial gases employed in the insulation system.

On this regard, [36] proposed what has been named the *Modified Lockheed Model* (Equation 3.5), which can be used in case of perforated aluminized shields and Dacron net spacers. This model, and as a consequence the insulation structure that it implies, is chosen to perform the analysis in this work.

$$q_{\text{Lock}} = \frac{2.4 \cdot 10^{-4}\left(0.017 + 7 \cdot 10^{-6}(800 - T_m) + 0.0228 \ln(T_m)\right)\left(\overline{N}\right)^{2.63}(T_H - T_C)}{N_s} + \frac{4.944 \cdot 10^{-10} \varepsilon_{\text{in}}\left(T_H^{4.67} - T_C^{4.67}\right)}{N_s} + \frac{1.46 \cdot 10^{4} P^{*}\left(T_H^{0.52} - T_C^{0.52}\right)}{N_s} \tag{3.5}$$

Where T_H and T_C are the temperatures (in K) of respectively the hot and cold side of the MLI, T_m is the MLI average temperature ($(T_H + T_C)/2$), N_s is the number of layers, $\overline{N}$ the layer density (in layers/cm), ε_{in} is the inner emissivity of the reflector layers, and P^* their interstitial pressure (in torr), which reaches values of 10^{-5} torr (about 10^{-8} bar) in highly evacuated MLI systems [17].

The (modified) Lockheed equation can be used to calculate the heat leak through the MLI both in case of uniform and variable density of the layers. In the second case, each MLI segment characterized by the same layer density requires a separate Lockheed equation. Assuming that interstitial pressure $P*$, total number of layers N_s and layer density N^* have been set for each VDMLI section, Equation 3.5 can be written as function of the hot and cold side temperatures only: $q_{Lock} = q_{Lock}(T_H, T_C)$.
Using Figure 3.8 as reference, it is therefore possible to write the following relations for the net heat loads to each MLI subnode:

$$\begin{aligned} q_{\text{net,outer}} &= q_{\text{in,external}} + q_{\text{Lock}}(T_{\text{out}}, T_{\text{mid}}) \\ q_{\text{net,middle}} &= q_{\text{Lock}}(T_{\text{out}}, T_{\text{mid}}) + q_{\text{Lock}}(T_{\text{mid}}, T_{\text{in}}) \\ q_{\text{net,inner}} &= q_{\text{Lock}}(T_{\text{mid}}, T_{\text{in}}) + q_{\text{tank}} \end{aligned} \tag{3.6}$$

According to [36], it is possible to find the temperature of each VDMLI sector by iteratively solving a system of nonlinear equations based on the thermal balance between the heat fluxes through the sections, which have the same magnitude and direction when assuming steady-state conditions.

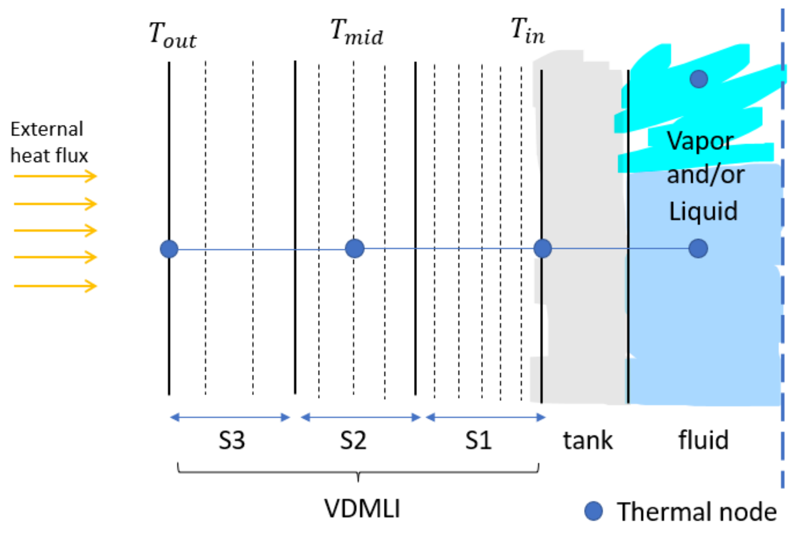

Figure 3.8: Variable Density MLI schematic and nodal structure.

When using a VDMLI structure, the number of possible combinations of number of layers and layers density becomes high. It is thus necessary to perform a preliminary selection based on data existing in literature in order to identify the most efficient VDMLI configurations to be applied to this analysis. [31] presented and validated through experiments a practical method to optimize any VDMLI configuration. Results showed that the best thermal performance in terms of lowest heat leak is given by the configuration pictured in Figure 3.9, which corresponds to a density of the middle (S2) and inner (S1) MLI sector which is respectively 2/3 and 1/3 of the outer one (S3).

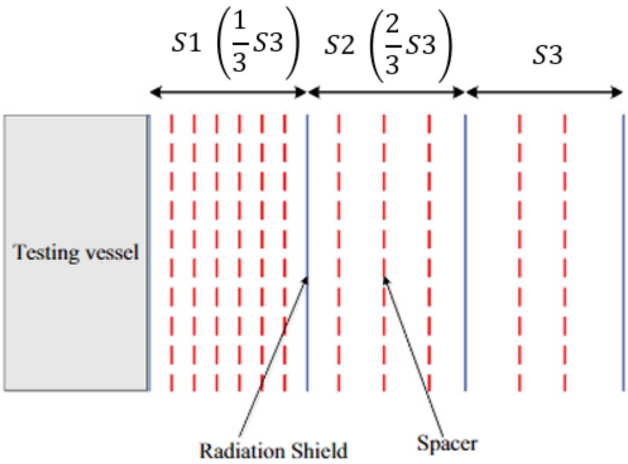

Figure 3.9: Optimized variable density MLI configuration [31].

Once the optimal layers density distribution has been defined, it is necessary to identify a relation that is able to define the number of layers per sector based on a given density distribution. This is necessary in order to gather all the inputs needed by the Boil-off tool, which are, in case of the MLI, the layers densities and the number of layers per sector. The procedure followed is explained hereby.
The thickness of any MLI sector characterized by a layer density $\overline{N}$ can be written as:

$$t_{MLI} = \frac{N_s}{100\overline{N}} \tag{3.7}$$

Where N_s is the total number of reflector layers, and the layers density $\overline{N}$ is expressed in layers/cm (hence the factor 100). In particular, in case of VDMLI, the following relation holds:

$$t_{VDMLI} = \frac{N_{s3}}{100\overline{N}_{s3}} + \frac{N_{s2}}{100\overline{N}_{s2}} + \frac{N_{s1}}{100\overline{N}_{s1}} \tag{3.8}$$

Equation 3.8 has four unknowns: the three layers numbers (N_{s1}, N_{s2} and N_{s3}), and the VDMLI total thickness t_{VDMLI}, meaning that three more equations are needed to find a solution.
The first equation can already be found by knowing that the sum of the layers numbers of each VDMLI sector has to be equal to a total number of layers chosen by the user.
As for the remaining two equations, they can be written by assuming that all the VDMLI sectors have the same thickness. This is in fact a common practice when using VDMLI structures, and it has already been done by [23] and [61].

Applying the considerations made above and manipulating a bit the equations, system 3.9 is found:

$$\begin{cases} N_{s3} = \dfrac{N_{s,tot}/100\overline{N}_{s1}}{\frac{1}{100\overline{N}_{s3}} + \frac{1}{100\overline{N}_{s1}} + \frac{\overline{N}_{s2}}{100\overline{N}_{s3}\overline{N}_{s1}}} \\ N_{s2} = \frac{\overline{N}_{s2}}{\overline{N}_{s3}} N_{s3} \\ N_{s1} = N_{s,tot} - N_{s3} - N_{s2} \end{cases} \tag{3.9}$$

With the algorithm in Equation 3.9 it is thus possible to calculate the number of layers of each sector in a 3 segment VDMLI system, given the total number of layers and the layer density distribution. It can happen that the solution of Equation 3.9 corresponds to non-integer numbers of MLI layers. This is a consequence of assuming that all the VDMLI sectors have the same thickness. In practical applications, it is of course necessary that each VDMLI sector has an integer number of MLI layers. For this reason, in this work N_{s3} and N_{s2} are rounded to the smallest integer that is greater than or equal to the non-rounded value, and then N_{s1} is computed using the last equation in 3.9. The single thicknesses of the VDMLI sectors are adjusted accordingly and therefore they might not be the same in some cases, as it is shown in Table 6.4.

Finally, for the mass estimation of each MLI segment, the relation from [11] is used:

$$M_{\mathrm{MLI}} = \left[\rho_m + \frac{\rho_s}{t_s}\left(\frac{1}{100\overline{N}} - t_m\right)\right] N_s A \tag{3.10}$$

Where ρ_m and ρ_s are the specific weights of the reflectors and spacers respectively, while t_m and t_s are their respective nominal thicknesses, and A represents the tank surface area.
Equation 3.10 has been obtained by directly looking at the structure of the MLI blanket; in particular, the relation shown above is applicable only when each sheet of separator material covers the same surface (A) as each reflector layer. In case other separation techniques are employed, like for example bumper stripes [34], a different relation to estimate the mass contribution of the spacers should be used.

3.3.2. Propellant boil-off and venting process

As already discussed in section 2.4, the cryogen is stored in the tank at its saturation temperature and pressure, and there is no other gas in the ullage except for the cryogen vapor phase. This means that any heat leak into the tank would result in the liquid boil-off.
The more the fluid evaporates, the more the tank pressure increases; when the tank pressure design limit is reached, a venting process is activated to ensure that the pressure is kept under control. However, this also means that the boil-off vapors vented overboard are permanently lost.

The model used for the boil-off process, at each time-step (dt), is shown in Equations from 3.11 to 3.14, and the detailed procedure is explained hereby.
First, the boil-off rate of the liquid is computed and multiplied by the time-step to calculate the actual boil-off mass (Equation 3.11). It has to be noted that the prefix d refers to the variation of the value it is attached to. Therefore, dQ, dm, dT, dp are respectively the heat leak, mass increase (or decrease), temperature and pressure variations of the liquid and vapor at each time-step.
Once the boil-off mass is calculated, this adds up to the total vapor mass (Equation 3.12), which is then used to calculate the temperature (Equation 3.13) and pressure (Equation 3.14) increase of the vapor in the ullage. In particular, the temperature increase (dT_{vapor}) is computed using the heat capacity equation, while the pressure increase (dp_{vapor}) is calculated using the same approach as Borst [24]. According to this approach, the pressure increase of the ullage is given by two contributions: the pressure rise due to the boiled-off vapor (first term on the RHS), and the thermal expansion of the already existing vapor (second term on the RHS).

$$dm_{\text{boiloff}} = \frac{dQ_{\text{leak,liq}}}{L_{\text{liquid}}} dt \tag{3.11}$$

$$m_{\text{vapor}} = m_{\text{vapor}} + dm_{\text{boiloff}} \tag{3.12}$$

$$dT_{\text{vapor}} = \frac{dQ_{\text{vapor,net}}}{c_{\text{p,vapor}} m_{\text{vapor}}} dt \tag{3.13}$$

$$\frac{dp_{\text{vapor}}}{dt} = \frac{R_G m_{\text{vapor}}}{M_{\text{m, vapor}} V_{\text{vapor}}} dT_{\text{vapor}} + \frac{R_G T_{\text{sat}}}{L_{\text{liquid}} V_{\text{vapor}} M_{\text{m, vapor}}} dQ_{\text{leak,liq}} \tag{3.14}$$

In the equations above, m refers to the mass measured in kg, while M corresponds to the molar mass of the substance considered, measured in kg/mol. The liquid and vapor thermo-physical properties are taken from the open-source CoolProp library [46].

A tank pressure check is then performed to verify that the ullage pressure is still lower than the maximum allowed value p_{max}. If the pressure in the ullage exceeds this threshold, the venting process

is started until a target venting pressure is reached.
Once the excess vapor has been vented outside the tank, the remaining ullage undergoes an expansion process inside the tank caused by the pressure reduction. According to [1], for operations that run only for a limited amount of time (i.e. a few minutes), the expansion process in the tank can be considered adiabatic, that is during the expansion very little heat transfer happens between the vapor and the environment. Being venting a quick process (all the excess vapor is immediately discharged), the adiabatic expansion assumption can be considered valid. This means that the Poisson's equation[2] can be used to calculate the temperature of the vapor left in the ullage after venting (Equation 3.15).
The new ullage vapor temperature and pressure are then used to compute the vapor mass in the ullage (Equation 3.16), which in its turn is used to assess the quantity of vapor mass that has been vented (Equation 3.17). Dividing this quantity by the time-step yields to the venting rate (Equation 3.18).

$$T_{\text{vap,fin}} = T_{\text{vap,in}} \left(\frac{p_{\text{vap,in}}}{p_{\text{vap,fin}}} \right)^{1-\gamma/\gamma} \tag{3.15}$$

$$m_{\text{vap,fin}} = \frac{p_{\text{vap,fin}} V_{\text{vapour}} M_m}{R_G T_{\text{vap,fin}}} \tag{3.16}$$

$$dm_{\text{vent}} = m_{\text{vapour}} - m_{\text{vap,fin}} \tag{3.17}$$

$$\dot{m}_{\text{venting}} = \frac{dm_{\text{vent}}}{dt} \tag{3.18}$$

The venting procedure explained above has been applied to a single tank depot case in GEO (45 layers with a density of 16 layers/cm) to verify that the model is working properly. In particular, liquid hydrogen is initially stored in the tank at its saturation temperature at 1.3 bar pressure. Boil-off of the liquid causes the ullage pressure to rise up to a maximum value of 3 bar, after which the vapor is vented back to the pressure of 1.3 bar.
A total storage time of 60 days is considered, however only the pressure and temperature data after 20 days are shown here to allow the values to settle from their initial guesstimates, being this a steady-state analysis. The pressure and temperature profiles of the ullage and liquid in the tank for different venting cycles are shown in Figure 3.10.

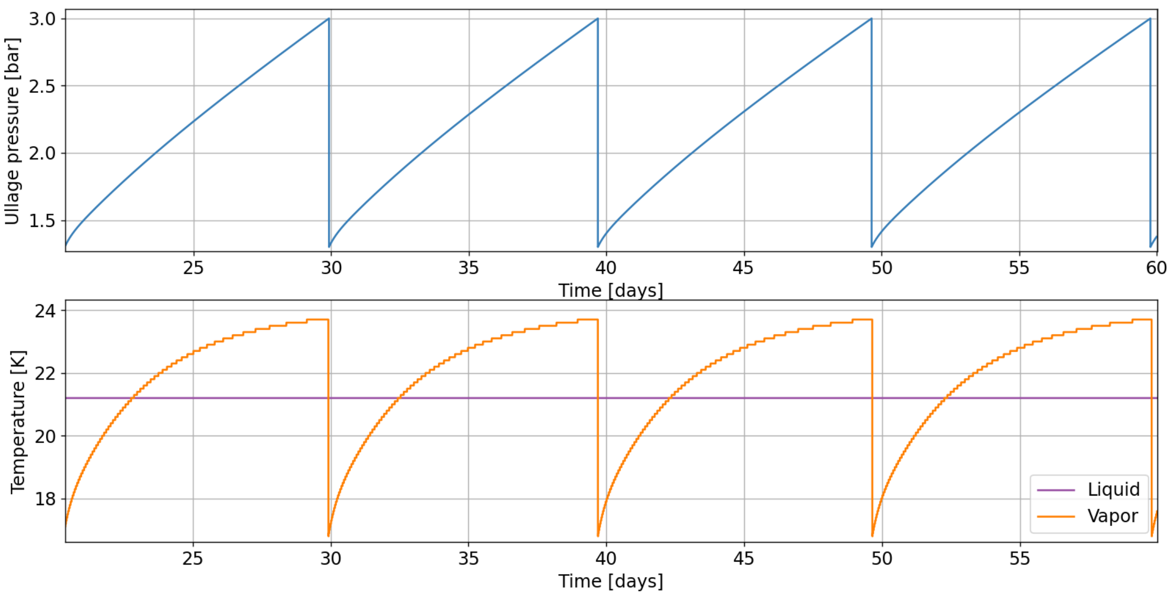

Figure 3.10: Tank pressure and temperature over time, including the effect of venting cycles.

As expected, the ullage pressure is oscillating between the venting target pressure (1.3 bar) and the maximum tank pressure (3 bar). The vertical lines in the plots correspond to the venting phase, in

[2] pV^{γ} = const, with γ representing the isentropic expansion coefficient [1]

agreement with the assumption of immediate discharge of the excess vapor. In particular, the ullage pressure decreases as a result to the gas release, while the temperature of the ullage gas decreases as a consequence of its adiabatic expansion (Equation 3.15) in the tank after the venting. Once venting is over, ullage pressure and temperature start to gradually increase again as a result of the heat penetration and the liquid boil-off in the tank. Being the stored liquid at saturation, any heat penetration results in its boil-off. For this reason, the liquid temperature is set to the saturation temperature at the target venting pressure (1.3 bar) and does not vary during the venting process.

In addition, the vapor mass over time in the ullage is shown in Figure 3.11. The venting cycles correspond to the vertical lines in the plot, that indeed show a decrease of the vapor mass in the ullage. Furthermore, between one venting cycle and the next, the vapor mass is gradually increasing due to the boil-off of the bulk liquid, which adds to the vapor in the ullage. The longer the cryogen is stored, the more the liquid boils: this effect is shown in an overall increasing trend of the vapor mass in the ullage. In fact, already in Figure 3.11 it can be noticed that, as the storage duration increases, the peaks in the plot keep reaching higher values.

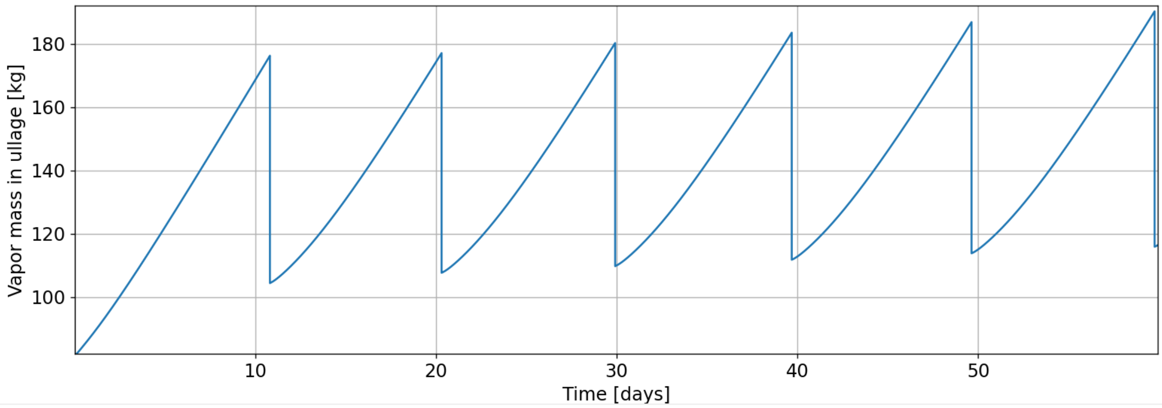

Figure 3.11: Vapor mass in ullage over time, including the effect of venting cycles.

3.3.3. Vapor Cooled Shield (VCS)

The vented gases can either be sent directly into space, or, being them still relatively cold (around saturation temperatures), they could be allowed to exchange heat with the tank system, thus making use of their cooling potential. This thermal control technique goes by the name of Vapor Cooled Shield (VCS).

The VCS is modeled as a high thermal conductive metal shield with a spiral flow tube through which the venting gas flows [22]. One important assumption in the modelling of the VCS is the temperature uniformity of the shield. A schematic of the VCS structure can be found in Figure 3.12a, while a detailed architecture and principal heat flows occurring are shown in Figure 3.12b.

According to [22], placing the shield between two MLI segments (with same or varying layers density) achieves the most efficient cooling performance of the VCS. Indeed, other configurations are possible, such as placing the vapor cooled shield directly in contact with the tank wall [52]. This solution is not however very advantageous (as it is investigated later in subsection 4.2.2), because the temperature measured on the tank wall is very close to the one of the vented vapor in the shield (which is the saturation temperature of the cryogen at the ullage pressure), thus bringing less heat leak reduction into the tank.

(a) Schematic of vapor cooled shield system [51].

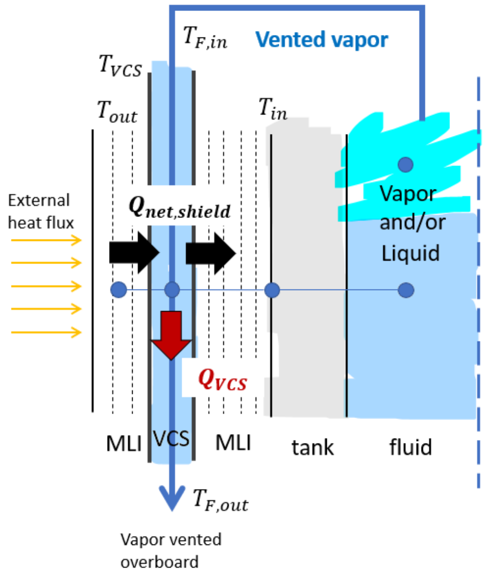

(b) Vapor cooled shield system main parameters and heat balance.

Figure 3.12: Vapor Cooled Shield structure and heat balance.

In this work, the vapor cooled shield has been modelled as a solid-vapor heat exchanger between the vented gases and the shield itself, that is the heat load subtracted from the VCS vapors is computed using the convective heat transfer correlations. After that, it is possible to use the net heat leak into the shield to compute its temperature, and the heat load absorbed by the fluid to find its outlet temperature at the end of the spiral path.

The main equations used to model the heat exchange process in the VCS shield are shown hereby:

$$Q_{VCS} = h_{\text{VCS}} A_{\text{cont}} (T_{\text{VCS}} - \overline{T}_F) \tag{3.19}$$

$$\frac{dT_{\text{VCS}}}{dt} = \frac{Q_{\text{net,shield}} - Q_{\text{VCS}}}{M_{\text{shield}} C_{\text{p,shield}}} \tag{3.20}$$

$$T_{\text{F,out}} = T_{\text{F,in}} + \frac{Q_{VCS}}{\dot{m}_{\text{vent}} C_{\text{p,vent}}} \tag{3.21}$$

Where Q_{VCS} is the heat absorbed by the fluid (also shown in Figure 3.12b), $Q_{net,shield}$ is the net heat load into the shield; T_{VCS}, T_F and $\overline{T}_F$ are the temperatures of respectively the VCS shield, the vented gas and the average temperature of the fluid in the VCS tube.
$C_{p,shield}$ is the heat capacity of the shield and it mainly depends on the material it is made of, while M_{shield} refers to the shield mass, here simply computed using the shield thickness and material properties. Moreover, A_{cont} refers to the available heat exchange area, and it is calculated using the VCS tube diameter and total length. As for the fluid, $\dot{m}_{vent}$ is the venting rate of the vapor in the ullage, and $C_{p,vent}$ is the heat capacity of the vented gas.
The convective heat transfer coefficient h_{VCS} is modelled using the procedure shown in subsection 2.4.3. All the fluid related properties have been computed according to their temperature and pressure using the open-source library CoolProp [46].

In order to calculate the shield and fluid temperatures of the VCS system, the partial differential equations problem described by Equation 3.19, 3.20 and 3.21 has to be solved numerically. The method chosen for the numerical integration is forward Euler (see Appendix A.1).

The algorithm used for the VCS case is shown in 3.22:

$$\begin{aligned} Q^i_{\text{VCS}} &= h_{\text{VCS}} A_{\text{cont}} \left(T^{i-1}_{\text{VCS}} - \frac{T^1_F + T^{i-1}_F}{2} \right) \\ T^i_{\text{VCS}} &= T^{i-1}_{\text{VCS}} + dt \frac{Q^i_{\text{net,shield}} - Q^i_{\text{VCS}}}{M_{\text{shield}} c_{\text{p,shield}}} \\ T^i_{\text{F,out}} &= T_{\text{F,in}} + \frac{Q^i_{\text{VCS}}}{M_{\text{vent}}/dt \cdot c_{\text{p,vent}}} \end{aligned} \tag{3.22}$$

Where i is used to indicate the current integration step.
The VCS is however not always active, but its functioning depends on the venting system. In fact, vapors are vented from the ullage only in case the maximum allowed pressure in the tank is reached. When this happens, the VCS loop is activated.

Again the single tank depot case in GEO has been analysed to verify the proper working of the model. In this case, a Variable Density MLI blanket with a VCS shield in the middle sector is considered. The VCS shield temperature over time, together with the ullage pressure profile to indicate the venting process, are shown in Figure 3.13. Here it is shown that after the venting process, the VCS shield reaches a temperature close to the one of the stored cryogen, to then gradually increase again until another venting process is started.

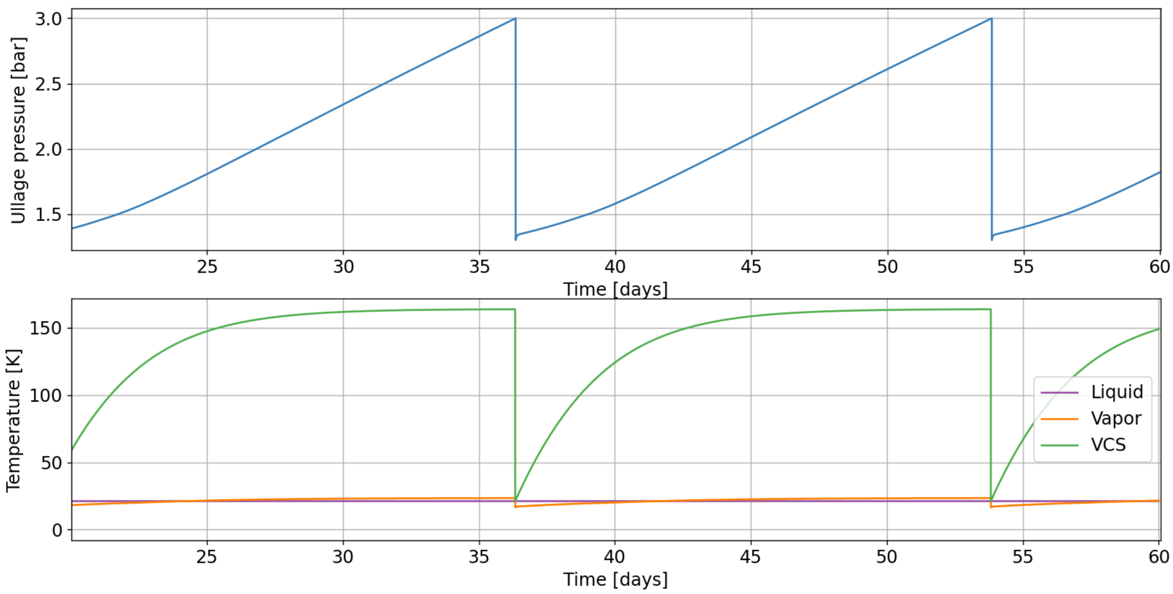

Figure 3.13: Tank pressure and temperature over time, including the effect of venting cycles and a Vapor Cooled Shield.

It has to be noted that the heat exchange model used for the VCS requires a relatively small time-step in order to return a solution which is free of numerical instabilities. In particular, the model has shown to be working for time-steps in the order of 1e-4 seconds. This value however does not agree with the time-step selected for the boil-off tool simulations, which is set to four seconds. In order to make the two models compatible, a multi-time step analysis is performed, using the bigger time step for all the computations in the tool and switching to the smaller one only in case the VCS is activated. This way, the heat exchange reaches solution convergence and return a steady-state shield temperature value.

3.4. Boil-off tool structure

Putting together all the elements just described in this chapter, it is possible to finally build the complete structure of the Boil-off tool. This is shown in the Boil-off tool block diagram (Figure 3.14).

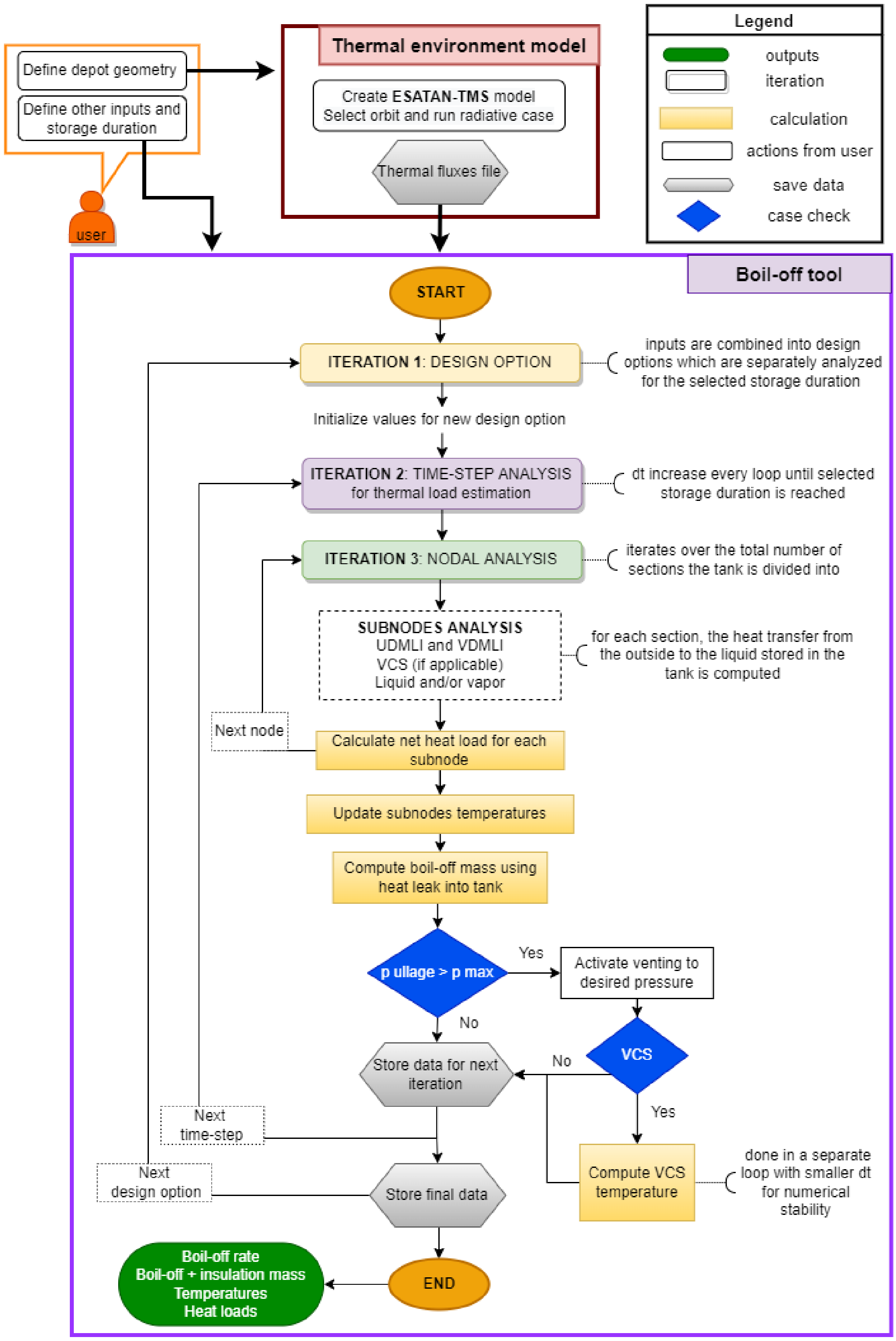

Figure 3.14: Boil-off tool block diagram.

The Boil-off tool requires two main sources of inputs before running the simulations, them being the thermal environment data from ESATAN-TMS, and the other parameters chosen by the user. A summary of all the required inputs for the Boil-off tool is given in Table 3.1.

Table 3.1: Boil-off tool inputs list.

Mission time [months]	Total duration, time-step for the analysis
Thermal environment	Thermal fluxes data file from ESATAN-TMS T_{space}, gravity
MLI	Layer density Number of layers VDMLI structure (if applicable) Layer specific weight, nominal thickness, conductivity, heat capacity Inner and outer optical properties Spacer specific weight, nominal thickness
VCS	Tube diameter and length Shield material, density, thickness, heat capacity Time-step for analysis
TANK	Radius, tank head type (sphere or ellipsoid) Propellant mass, fill level Storage pressure and temperature, maximum pressure Desired venting pressure Material, wall density and thickness (if applicable)

The main function of the Boil-off tool is to thermally solve the tank nodal network shown in Figure 3.7. In particular, the tool structure is organized into three main iteration loops:

1. **DESIGN OPTION**: each iteration in this loop analyses a different thermal control option for the depot.
   For example, the user can choose to study a single tank depot in Low Earth Orbit covered in MLI with a uniform density. This configuration corresponds to different design options with varying number of MLI layers and their density distribution, which are chosen by the user and combined by the tool. For example, choosing two densities and four different total number of layers corresponds to a total number of eight design options analysed by the tool.
2. **MISSION DURATION**: this is the time-step analysis of the forward Euler method used to compute the heat balance and temperature distribution of the nodes in the thermal network. Each iteration corresponds to a time increase equal to a user-defined time-step dt. The loop continues to run until the desired storage duration (specified by the user in the inputs) is reached.
3. **NODAL ANALYSIS**: this iteration is only done to allow the user to choose the number of sections the tank is divided into. The heat balance of the tank nodes is analysed in this loop. In particular, every iteration deals with a single tank section, and the reason behind the use of a loop is so that the user can decide the number of tank sections. For each iteration, the heat transfer through the sub-nodes of the insulation structure is computed.

Once the heat balance of every node in the tank thermal network is complete, the heat loads are used to update the temperatures of the nodes following the procedure shown in Equation 3.4. After that, the boil-off mass and other parameters related to the stored cryogen are calculated (Equations from 3.11 to 3.14), and the ullage pressure is checked. If a maximum pressure is exceeded, the venting process is started (Equations from 3.15 to Equation 3.18). If the user chose to include the VCS in the analysis, the VCS algorithm shown in Equation 3.22 is run to compute the temperature of the shield.
Heat load and temperature data are stored in matrices and vectors to be used in the calculations of the next time-step. Once the desired storage time is reached, the data are stored for one last time, and the next design option is analysed following the procedure just described. Once all the design options have been simulated, the tool stores the data in a single output file.

4

Sensitivity analysis

In this chapter, a sensitivity analysis on both the assumptions and the design choices made to build-up the Boil-off tool is performed. According to [62], the main objective of a sensitivity analysis is to determine the variation of a system in response to a variation of specific inputs. In the process of developing a computer program, sensitivity analyses are used for diagnostics, allowing the designer to assess the robustness of specific design choices.

The analysis in this chapter can be divided into two main groups based on the specific area of interest: thermal environment definition, and nodal structure. In addition, a comparison with a propellant depot case study found in literature is also performed.

4.1. Thermal environment definition

In subsection 3.2.2, the tank structure to be analysed in this work has been defined. Furthermore, it has been mentioned that ESATAN-TMS allows the user to define the number of sections the model is divided into. An example of this is given in Figure 4.1 where two tank models formed by 12 thermal nodes are given: on the left, the single tank has been divided into as many sections as the number of thermal nodes; while on the right each node has been further divided into a user chosen number of sections (here five).

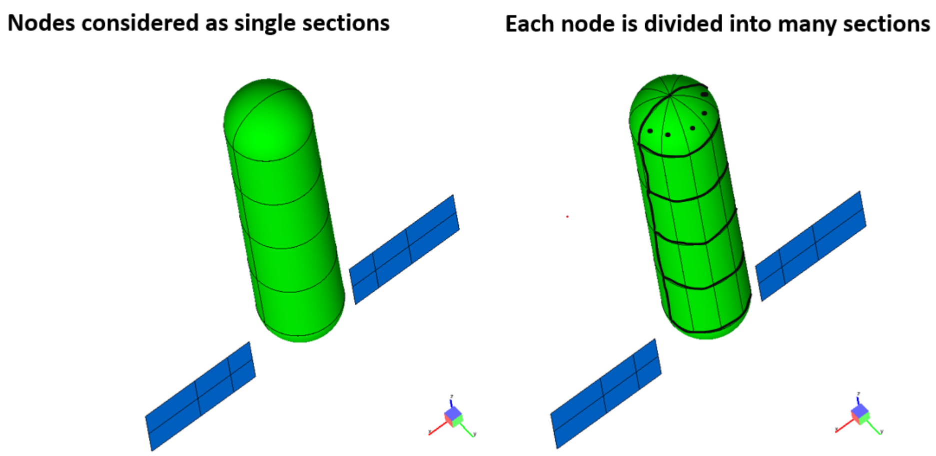

Figure 4.1: Examples of two different versions of ESATAN-TMS single tank model: one section per node (left), five sections per node (right).

The reason why one would want to increase the number of sections is to increase the accuracy of the heat fluxes calculation. In fact, ESATAN-TMS returns the average solar flux for each section in which the model is divided into. Being the tank surface curved, the incoming heat load is dependant on the position of the section with respect to the solar vector. An example of this effect is shown in

Figure 4.2, where it is possible to notice that the intensity of the flux vector perpendicular to section B (which is directly facing the Sun), is higher than in sections C and A. In particular, the more the section is titled with respect to the Sun vector, the less heat flux it receives.

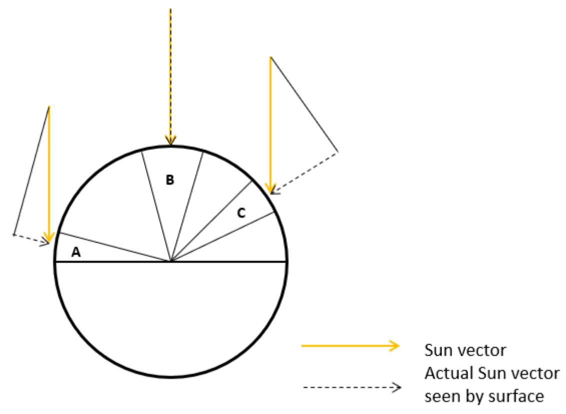

Figure 4.2: Propellant tank sections viewed from above.

However, increasing the number of sections per node comes with a cost: not only computational times in ESATAN-TMS are longer, but also the number of heat flux data to elaborate increases, since the program returns one flux value per section per orbital position. For example, the model shown on the right of Figure 4.1 has five sections per node. The entire tank is divided into 12 nodes, meaning that the total number of sections in the whole model is 60, which corresponds to the number of heat fluxes values given by the program for each orbital position. This number is definitely greater than the 12 heat fluxes that are found by considering each node as a single section, like the model on the left of Figure 4.1.

In this section, the effect of varying the number of tank sections on the heat loads is first assessed. To do so, the simple tank model described in subsection 3.1.1 is compared to the ESATAN-TMS model. After that, the number of sections per node is increased to assess whether considerable changes could be noticed in the incoming heat load. The effect of different depot attitudes and configurations on the thermal fluxes on the depot is also studied.
As already mentioned in section 2.1, any object orbiting Earth is subjected to three main sources of heat fluxes: solar, albedo (from Earth itself), and infra-red (IR) planetary radiation. In particular, the solar flux is never negligible for objects orbiting Earth, while albedo and IR radiation start to become less intense as the objects moves away from the planet. For example, in case of a GEO depot, planetary and albedo represent less than 2% the total heat load incoming on the spacecraft [17].
For simplicity, only the solar fluxes have been considered for this analysis. Therefore, a GEO orbit is more suitable for the comparison.

4.1.1. Effect of changing tank sections number

The comparison between the simple and ESATAN-TMS models can be found in Figure 4.3, separately for the cylindrical body and the spherical end-caps. In particular, the values on the X axis correspond to the number of sections each node has been further divided into; since the simple model only works with one section per node, the comparison is only done for this case, which corresponds to the value ”1” on the X axis. The heat loads shown in the plots are a result of radiation which is directly incident on the faces of the model, thus no optical properties of the coating surface are needed. In case one would be interested in the absorbed heat, this can be calculated by multiplying the values in Figure 4.3 by a chosen absorptivity.
Figure 4.3a shows a good agreement between the simple and ESATAN model on the estimation of the heat loads on the tank cylindrical body, with differences not bigger than 2 %. Furthermore, the effect of changing number of sections on the total heat load is negligibly small.

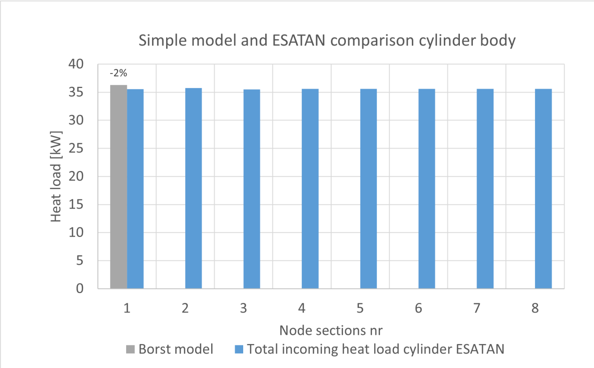

(a) Tank cylindrical body.

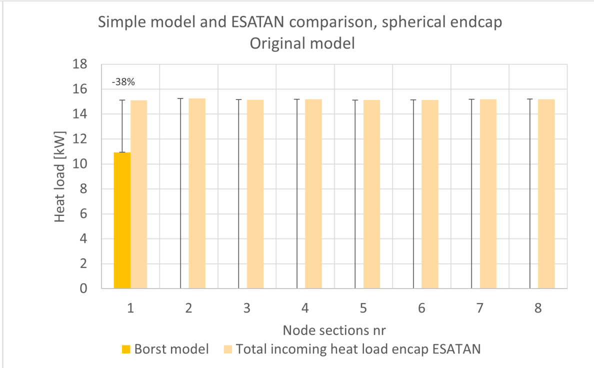

(b) Tank spherical end-caps.

Figure 4.3: Sensitivity analysis on ESATAN-TMS thermal model sections number and comparison with simple model for GEO case.

On the other hand, when performing the same calculations for the spherical end-caps (Figure 4.3b), the differences between the simple model and the ESATAN-TMS model increase up to 40%. This is due to an incompatibility between the selected incidence angle and frontal area for the end-caps in the model shown in Figure 3.1. In fact, here the considered frontal area is the one of half a circle with the same radius as the tank radius; therefore, tilting the Sun vector of $45°$ leads to an underestimation of the incoming thermal flux on the node. For this reason, a new solar incidence angle thermal model is proposed in Figure 4.4a, and it proved to match the heat loads of the ESATAN-TMS model also for the spherical end-caps (see Figure 4.4b).

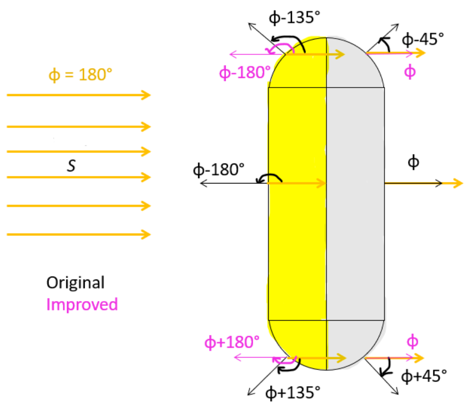

(a) Original (black) and improved (purple) thermal environment models.

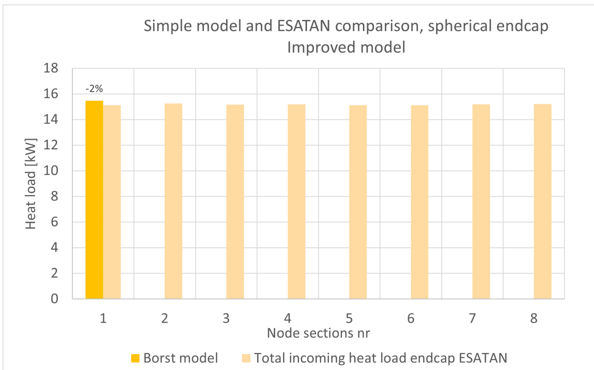

(b) Tank spherical end-caps improved model and ESATAN-TMS comparison.

Figure 4.4: Improved simple thermal model and comparison with ESATAN-TMS for the spherical end-cap sections.

In conclusion, a good agreement between the simple and ESATAN-TMS models has been found for the single tank GEO depot, with differences in the incoming fluxes that do not go over 2 %. Furthermore, Figures 4.3a and 4.4b show that increasing the number of sections per node in the ESATAN-TMS model has no effect on the intensity of the heat loads, both on the tank cylindrical body and the spherical end-caps. This means that the ESATAN-TMS model can be simplified by selecting a number of sections that is equal to the number of nodes without losing in accuracy of the thermal fluxes estimation.

4.1.2. Depot attitude study

Figure 4.5 shows the total solar energy received by the single tank model in GEO for three different depot attitudes: tank left side to Sun (sunlit side colored in yellow in the figure), tank end-cap to Sun (sunlit side colored in light blue), and tank longitudinal axis aligned with Nadir (shown in Figure 4.6).

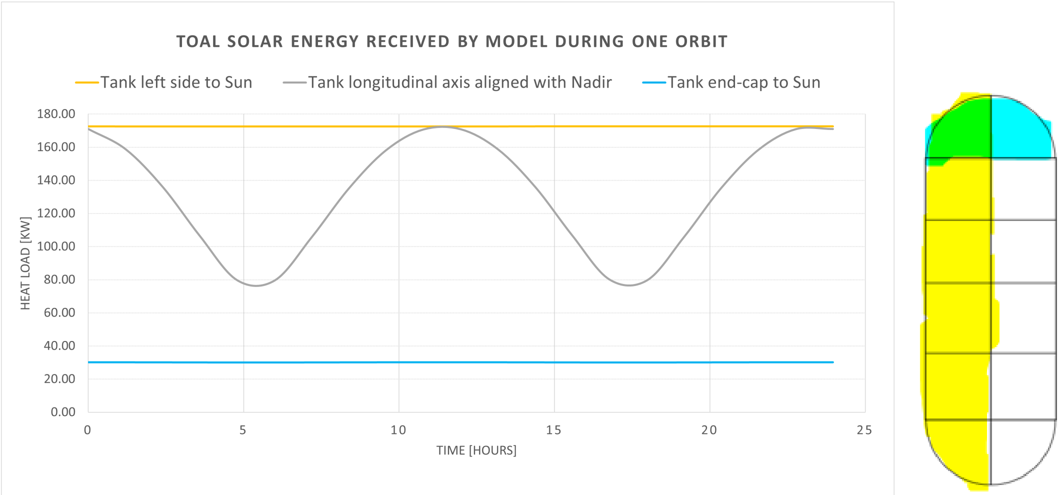

Figure 4.5: Total solar heat load received by the model in one orbit for different depot orientations.

It can be noticed that aligning the tank axis with Earth Nadir results in variable heat loads on the depot along the orbit. In particular, the values oscillate between a minimum and maximum based on the position of the tank in the orbit (maximum corresponds to tank side facing the Sun, while minimum is for the end-caps).

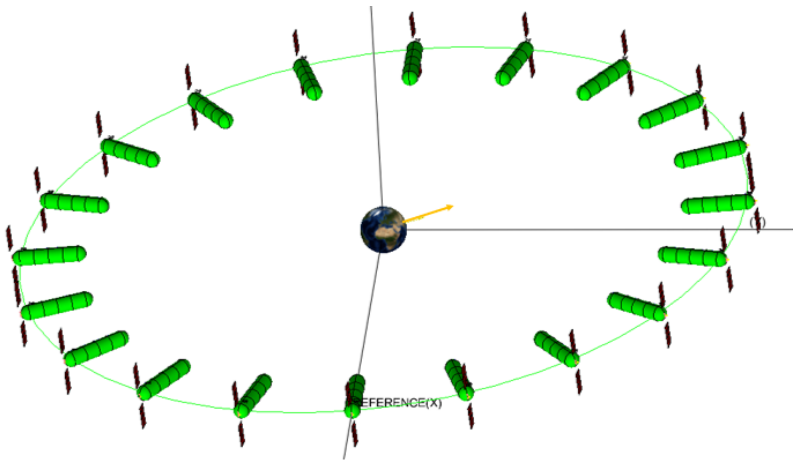

Figure 4.6: ESATAN-TMS orbit display of single tank GEO depot with longitudinal axis aligned with Nadir.

In conclusion, heat load variability over time can depend both on the orbit and the attitude chosen, therefore a proper thermal environment model should also be able to track the radiation intensity over time. This is not only valid for the GEO case just analysed, but it can also be applied to orbits characterized by daily eclipses (i.e. LEO), where heat load variations can indeed be more critical (see subsection 5.2.3). The ESATAN-TMS model chosen in this work is able to assess these changes, being them because of the specific orbital position or the spacecraft's orientation.

4.1.3. Multi-tank models: effect of reflected heat

Orbital propellant depots can also be grouped in what are called multi-tank structures, as previously shown in section 1.2. An example is given by [3], which proposed the eight tank depot station shown in Figure 4.7.

The Boil-off tool is only able to perform the thermal analysis for a single tank. Nevertheless, in this case the tool can still be used to study one tank as part of a multi-tank group.

However, the analysis of the single tank as part of a multi-tank group may require a new thermal environment definition: when many tanks are grouped together, there might be additional fluxes absorbed due to heat being reflected from other tanks onto this one tank considered. This effect does not concern the single tank model as in that case all the reflected fluxes go into space, but it may be important in case of more complex tank structures like the one in Figure 4.7. Therefore, a sensitivity study on the effect of reflected fluxes on the results is performed hereby.

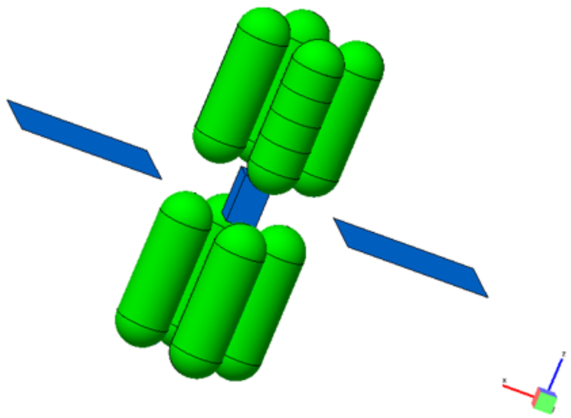

Figure 4.7: Eight tank depot station from [3] modelled in ESATAN-TMS (tank support elements have not been included in the preliminary sketch).

Figure 4.9 shows the total heat loads on each node of the tank, for both the single and the eight tank depot configuration. In particular, for the multi-tank model, the analysis has been focused on only one tank of the group, indicated in Figure 4.8. This tank is subjected to the worst case scenario in terms of fluxes, that is with one side fully facing the Sun, making a fair comparison with the single tank model.

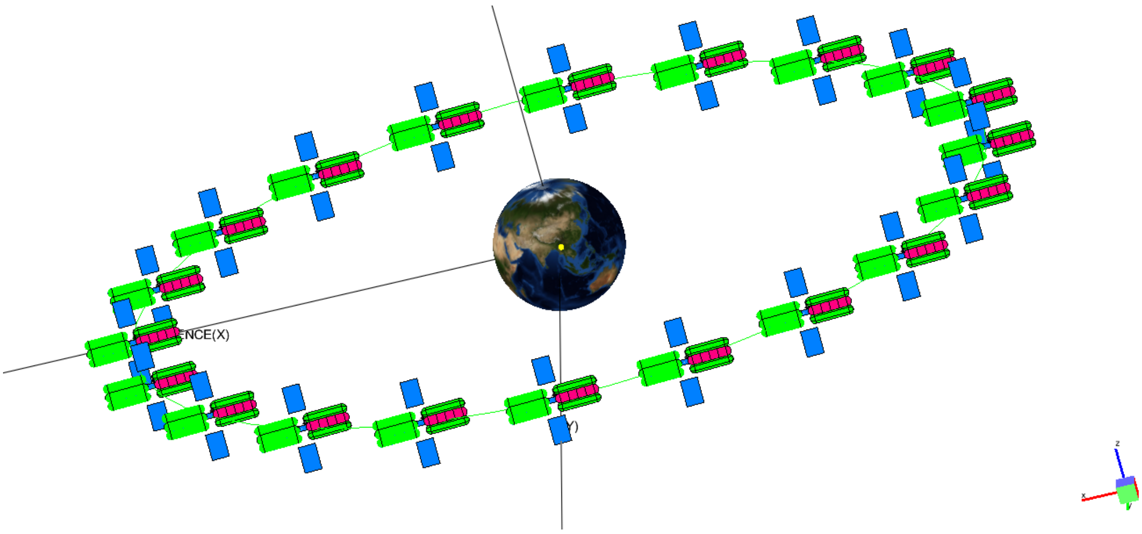

Figure 4.8: Eight tanks model orbit display, analysed tank in purple, reader looking from the Sun's side.

As already mentioned before, the effect of reflected heat can be neglected for the single tank case. In fact, Figure 4.9 shows that all the heat loads absorbed by the single tank depot are concentrated on its left side (nodes with the "L" label), that is the sunlit part of the depot; on the other hand, no incoming heat loads are recorded on the shadow side (nodes with the "R" label).

The effect just explained above does not apply for the eight tank model, where heat loads on the shadow sides of the tank exist as well (circled in black in Figure 4.9). In particular, these additional heat loads correspond to about 30 % of the total power received by the tank.

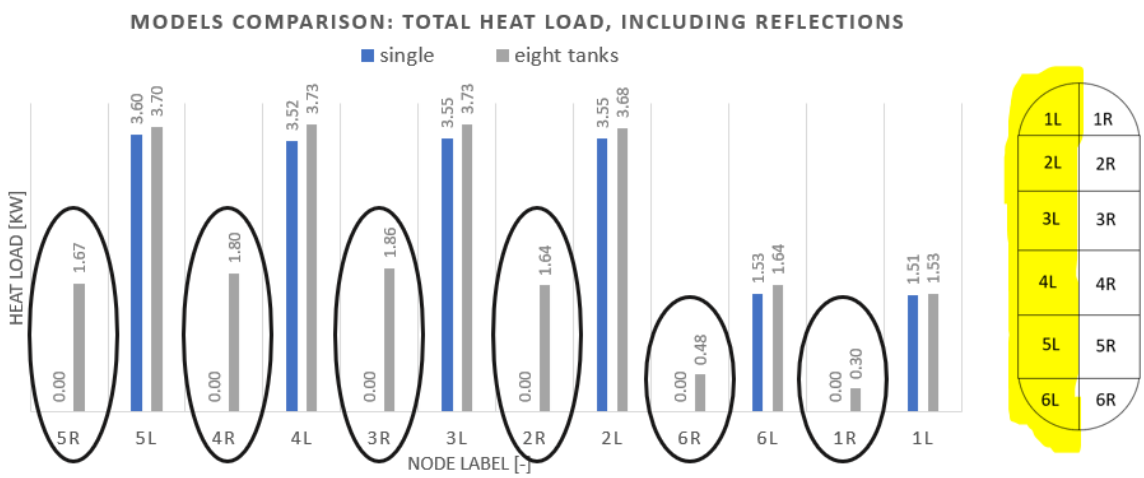

Figure 4.9: Total heat load (including reflections) on different GEO depot configurations. Sunlit side of tank highlighted in yellow.

The two depot configurations just studied have been applied to a case of three month storage of 34.6 mT of LH2 in GEO orbit in order to assess the effect of reflections on the hydrogen boil-off. The results are shown in Table 4.1.

Table 4.1: Effect of reflected fluxes on monthly boil-off for 34.6 mT of LH2 storage in GEO (45 MLI layers, 16 layers/cm).

	Single tank	**Eight tank model**
No reflections	0.69	0.69
Reflections	0.69	1.13
Increase	0 %	+ 64 %

As expected, including the effect of reflections does not change the monthly boil-off rate of the single tank design. On the other hand, in case of the eight tank depot, neglecting the reflected fluxes would bring to an underestimation of the monthly boil-off rate of about 70 %.
From these results, one could conclude that it is not convenient to use multi-tank structures as they result in a reduced thermal performance. However, they bring several other benefits to a depot system, for example the possibility to store more propellant than single tanks, thus supporting multiple missions. For this reason, a broader analysis on advantages and disadvantages of these depot structures should be performed to build a fair comparison with the single tank models. This is not done here due to time constraints, however some recommendations on how to proceed with the analysis are given in chapter 7.

4.2. Sensitivity analysis on nodal structure

When developing the boil-off tool (section 3.2), several assumptions regarding the nodal structure have been made. The aim of this section is to assess what is the influence of these choices on the results. In particular, attention is focused on the influence of adding the tank wall thermal node and the effect of changing the VCS position. Finally, a case study comparison is also performed.

4.2.1. Effect of adding tank wall node

When designing the nodal structure for the Boil-off tool, it has been chosen not represent the tank wall with a thermal node (see subsection 3.2.2). Nevertheless, it is worth to assess what the effect of adding a tank node is on the tool itself and its influence on the results.

Cryogenic propellant tanks are mainly made using materials such as Aluminium, Stainless steel or Titanium alloys (also confirmed by [63]). Therefore, these three material options are selected for the tank node analysis. The case study used is again the storage of 34.6 mT of liquid hydrogen in GEO. The complete thermal network, including the tank wall node, can be found in Appendix A.2. The results in terms of monthly boil-off for different designs are shown in Table 4.2.

Table 4.2: Monthly boil-off rates (wrt initial mass) for different numbers of MLI layers (16 layers/cm) and different tank materials, 34.6 mT of LH2 storage in GEO.

MLI	**BO rate [%initial mass/month]**				
	No tank node	Titanium 5 mm	Titanium 1 cm	Steel 1 cm	Aluminium 1 cm
45	0.69	0.67	0.66	0.64	0.66
55	0.56	0.55	0.55	0.53	0.54
65	0.50	0.49	0.48	0.46	0.48
75	0.44	0.43	0.41	0.40	0.41

From Table 4.2 it is possible to notice that including a tank wall node causes variations in the monthly boil-off rates that do not go over 5 %. More in detail, neglecting the tank node leads to an overestimation of a maximum of 10 kg of boiled-off mass per month. Although this value is low and not giving particular concerns, this effect should be known when simulating long storage times (i.e. after 10 months there is a difference of 100 kg and so on). Moreover, it is also possible to notice that by halving the tank wall thickness (done for the Titanium case), the resulting boil-off rates in the tank remain mostly unchanged.

Given the results, one may wonder why one would want to neglect the tank wall node in the nodal analysis. The answer to this question is shown in Table 4.3, where more details about each tank material option are shown.

Table 4.3: Tank material options and impact on Boil-off tool simulation time.

	Thickness	**Heat capacity**	**Thermal conductivity**	**dt**	**Runtime***
No tank node	-	-	-	4 s	5 minutes
Titanium Ti-6Al-4V	5 mm - 1 cm	526 J/kgK	6.7 W/mK	1 s	10 minutes
Stainless Steel 316	1 cm	500 J/kgK	16.3 W/mK	1 s	10 minutes
2195-T8 Aluminium	1 cm	900 J/kgK	130 W/mK	0.1 s	2 hours

*For 1 month of storage simulation and one design option

In particular, it can be noticed that the inclusion of the tank wall node increases the program run-time from 5 minutes in case of no tank node up to 2 hours of simulation for design option (for 1 month storage). This is absolutely not ideal, as a relatively short computational time is desired to be able to simulate multiple storage durations for many design options.

The different program run-times are a result of the time-steps that each option requires (second to last column of Table 4.3), which in their turn depend on the stability conditions of the numerical model used in the Boil-off program (see section A.1). Neglecting the tank wall node could considerably reduce the computational time of each design option while introducing a relatively small mass inaccuracy. Moreover, removing the tank node allows to rule out the tank material selection from the inputs list, thus broadening the applicability of the Boil-off program results to a wide variety of material options.

4.2.2. Effect of changing VCS position

As already mentioned in subsection 3.3.3, placing the vapor shield within the VDMLI minimizes the heat leak entering the cryogenic tank. To support this statement, a comparison of two VCS layouts is performed here. In particular, the vapor shield is first positioned within the VDMLI (case also identified as ”middle shield”), and then it is moved to the outside of the VDMLI, next to the tank wall (case also identified as ”inner shield”). The two configurations are shown in Figure 4.10.

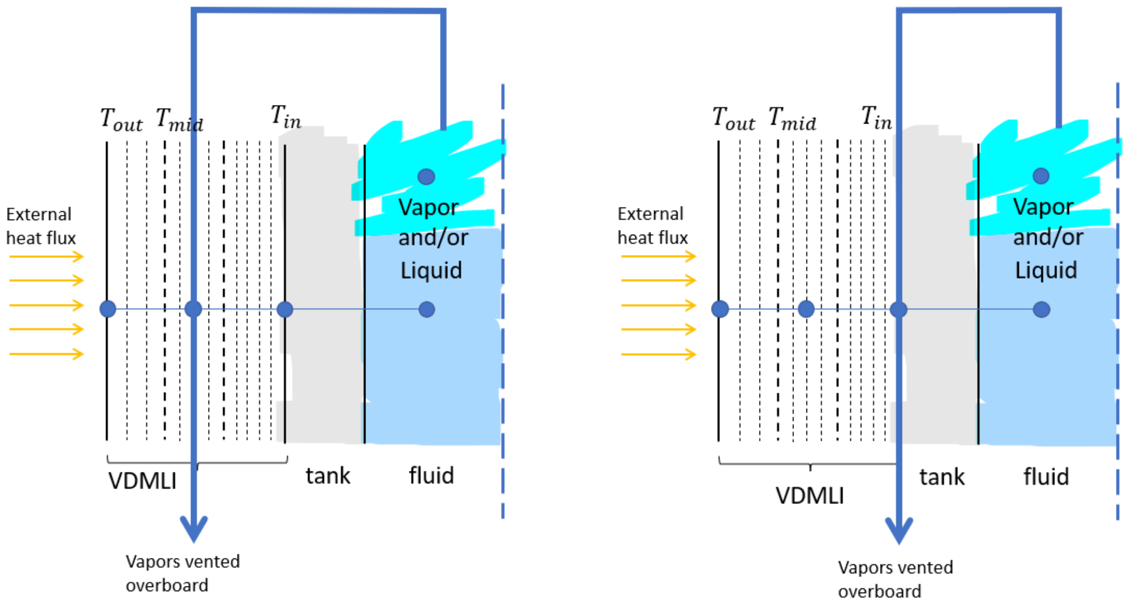

(a) Vapor shield placed within the VDMLI (Middle vapor shield). **(b)** Vapor shield placed outside the VDMLI (Inner vapor shield).

Figure 4.10: Proposed Vapor Cooled Shields layouts for sensitivity analysis.

The storage of 34.6 mT of LH2 has been selected for this analysis. The depot geometry consists in a single tank with one side continuously facing the Sun, and the other in shadow. The GEO orbit is selected for this case, however the results are applicable to all orbit types.

The comparison of the two different VCS layouts has been performed for different numbers of MLI layers. The outer layer density of the VDMLI is fixed to 16 layers/cm, while the middle and inner densities are determined using the procedure explained in subsection 3.3.1, and they are respectively 11 layers/cm and 5 layers/cm. The results are shown in Table 4.4, together with a graphical representation in Figure 4.11.

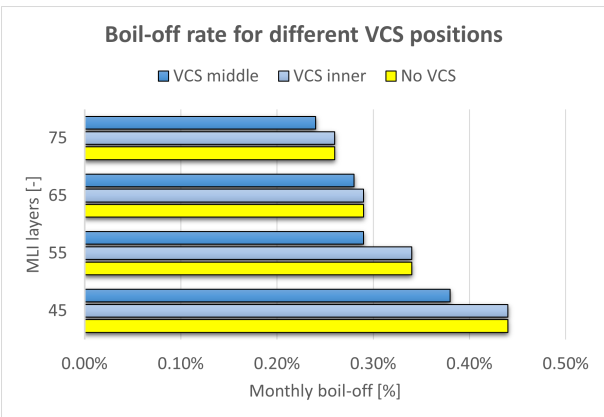

Figure 4.11: Plot of monthly boil-off for different MLI layers numbers and VCS positions.

MLI	BO rate [%initial mass/month]		
	No VCS	Inner shield	Middle shield
20	1.01	1.00	0.92
45	0.44	0.44	0.38
55	0.34	0.34	0.29
65	0.29	0.29	0.28
75	0.26	0.26	0.24

Table 4.4: Effect of different VCS locations on monthly boil-off, 34.6 mT of LH2 storage in GEO.

For all design cases analysed it is possible to notice that placing a vapor cooled shield next to the tank wall does not improve the boil-off rate in the tank with respect to the case where no shield is used. On the other hand, as expected, placing the vapor shield within the VDMLI structure reduces the monthly boil-off of more than 10 %, thus confirming this as the best solution between the two in terms of thermal performance.

The reason why a middle VCS shield would perform better than an outer one is because of the temperature difference between the shield and the fluid: by looking at Equation 3.19, it comes without saying that, the bigger this temperature difference, the more heat the shield removes from the insulation structure. The temperature distribution of the VDMLI structure for one of the cases analysed above is shown in Figure 4.12, both for the shadow (Figure 4.12a) and sunlit side (Figure 4.12b) of the tank.

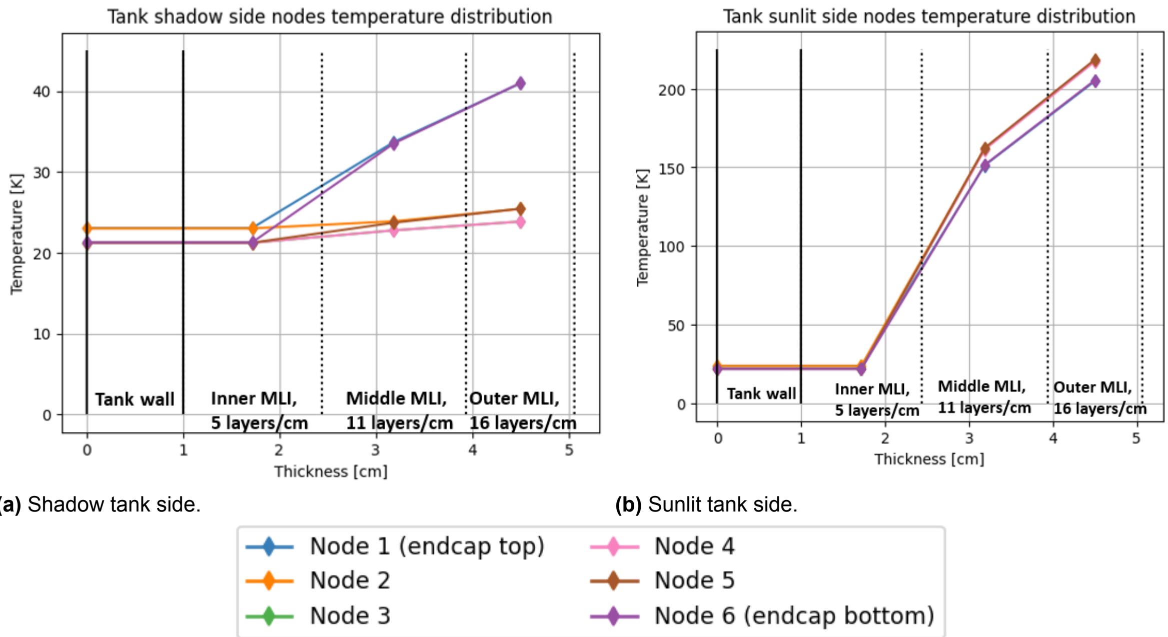

(a) Shadow tank side.

(b) Sunlit tank side.

Figure 4.12: Variable Density MLI temperature distribution. Total number of layers: 45.

Here it is noticed that, for both tank sides, the inner MLI layer has the same temperature of the tank wall, which is also close to the one of the fluid inside the tank (which is around 21 K). This effect is a consequence of the assumption that no tank wall node is used (see subsection 4.2.1).
On the other hand, the middle MLI layer temperature is about 35 K for the tank shadow side, and goes up to 160 K for the sunlit side. These higher temperatures, especially for the sunlit side, increase the temperature difference in Equation 3.19, making the middle vapor shield more effective than the inner one.

One last detail that can be noticed in Table 4.4 is that the differences in boil-off between the three cases reduce with increasing number of MLI layers. This is because the effectiveness of the MLI increases with the number of layers used, therefore one could ideally replace the complex VCS structure with a simple MLI blanket with more reflector layers. However, due to manufacturing complexity reasons, there is a limit on the maximum number of MLI layers that can be used (usually 80, according to [11]), thus making the use of VCS a very attractive solution to reduce the total number of MLI layers while keeping a low propellant boil-off rate.

4.3. Case study comparison

In this section, the Boil-off tool is used to reproduce the results of the cryogenic propellant depot analysis performed by Chai [11].

It has to be noted that a complete Boil-off tool validation is not achievable as data on the analysis of the thermal performance of propellant depot is currently lacking in literature. However, some similarities between this work and the one of Chai have been found, which has been deemed the most suitable to perform a partial validation of the Boil-off tool. The term "partial" refers to the fact that the only parameters compared are the monthly boil-off rate, which is indeed one of the main outputs this work is focusing on.

4.3.1. Chai case study: neutral surface spherical isothermal node

Before proceeding with the comparison, a brief background on the cases studied by Chai [11] is given. The thermal environment definition has been performed by Chai with the support of the Analytical Graphic's System ToolKit (STK) software and its built-in space Environment and Effect Tool (SEET). In particular, this tool is able to represent any spacecraft as a single isothermal node, and to calculate its temperature based on the optical properties chosen by the user. However, this tool is limited to either spherical or planar objects.

STK's depot shape limit is the reason why the case study performed by Chai considers a single, spherical propellant depot. The tank is thus represented by a single isothermal spherical node with neutral surface properties ($\alpha = 1$, $\varepsilon = 1$), placed in a 400 km circular orbit around Earth (LEO) at 28.5 degrees of inclination. Using this information, the orbit has been reproduced with ESATAN-TMS as shown in Figure 4.13.

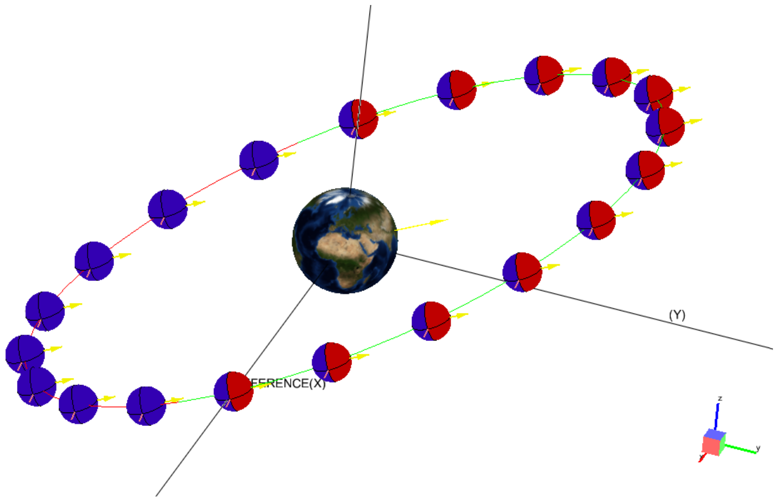

Figure 4.13: ESATAN-TMS orbit display, spherical isothermal node in LEO.

It has to be noted that the radius of the depot shown in Figure 4.13 is not important to the scope of this representation, but it becomes important for the heat load calculation and needs to be adjusted accordingly. In fact, when computing the node surface temperature from the heat balance between absorbed and emitted heat of a sphere, the value of the radius is divided out:

$$\begin{aligned} &Q_{\text{abs}} = Q_{\text{emit}} \\ &(q_{\text{solar}} + q_{\text{albedo}} + q_{\text{IR}}) \cdot \pi R^2 = (\varepsilon_{\text{IR}} \sigma T^4) \cdot 4\pi R^2 \\ &T = \frac{q_{\text{solar}} + q_{\text{albedo}} + q_{\text{IR}}}{4\varepsilon_{\text{IR}}\sigma} \end{aligned} \tag{4.1}$$

The value of the radius is thus not important for the calculation of the node surface temperature, which depends only on the incoming solar, albedo and planetary fluxes, which in their turn depend on the chosen orbit, the attitude, and the geometry of the depot. On the other hand, the value of the radius becomes relevant for the heat loads, which are computed by multiplying the fluxes by the depot frontal area.

To correctly reproduce the heat load profile provided by Chai (Figure 4.14a), a trial and error analysis has been performed. This consists in guessing several options for the sphere radius, which are then used to compute the heat loads on the sphere in LEO using ESATAN-TMS. Once the heat loads, and as a consequence the heat fluxes, are known, these can be used to verify that the maximum and minimum node temperatures comply with the values provided by Chai.
The heat load resulting from the trial and error analysis, together with the corresponding surface temperatures, are shown respectively in Figure 4.14b and Table 4.5. In particular, the depot that returned a good agreement with both heat loads and temperatures from Chai corresponds to a spherical node with a radius of 0.3 m.

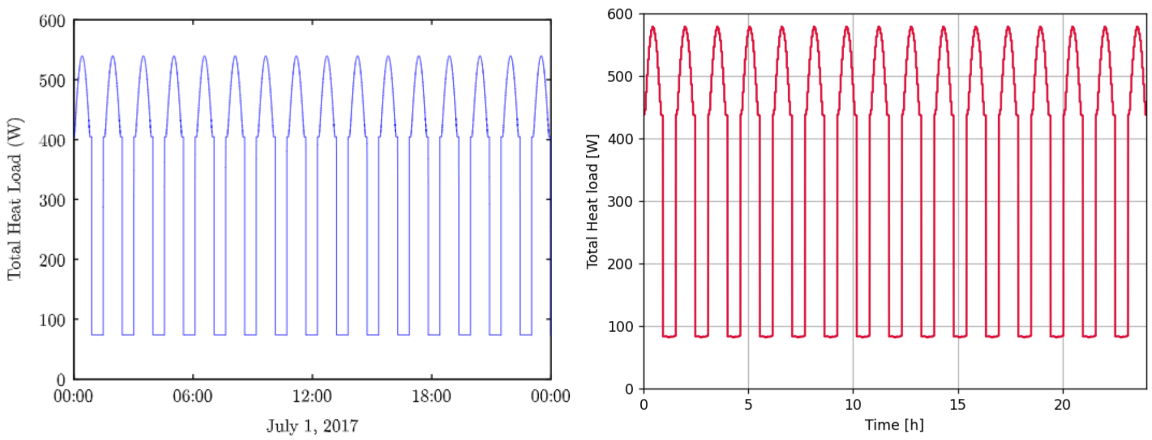

(a) Heat load profile of spherical isothermal node in LEO from Chai[11].

(b) Heat load profile of spherical isothermal node in LEO reproduced using ESATAN-TMS.

Figure 4.14: Heat load profiles comparison for spherical node in LEO.

Table 4.5: Maximum and minimum temperature and heat load for neutral isothermal spherical node, comparison with Chai [11] case study.

	Maximum		**Minimum**	
	Chai	BO tool	Chai	BO tool
Temperature (K)	319	310	190	188
Heat load (W)	590	580	74	80

The spherical tank depot has then been used by Chai to perform a thermal analysis,taking as main figures of merit the boil-off of the cryogenic fluid and the system mass of the thermal management system. Both liquid oxygen and hydrogen have been studied, however the comparison performed here only concerns the hydrogen tank. In particular, the depot is placed in the same LEO orbit as analysed above, with the only difference given by the propellant capacity, which has been set to 32 mT for liquid hydrogen. The considered storage duration is 1 Earth year.
To comply with the propellant capacity requirement, a new tank radius needs to be defined: no details on this regard are given by Chai, however assuming a storage pressure of 1.3 bar and a tank fill level of 0.9, 32 mT of liquid hydrogen can be stored in a spherical tank with a 5 metres radius. As already proven before, this new radius value only affects the heat loads on the tank, leaving the surface temperature unchanged. The heat load profile for the 32 mT LH2 tank is shown in Figure 4.15.

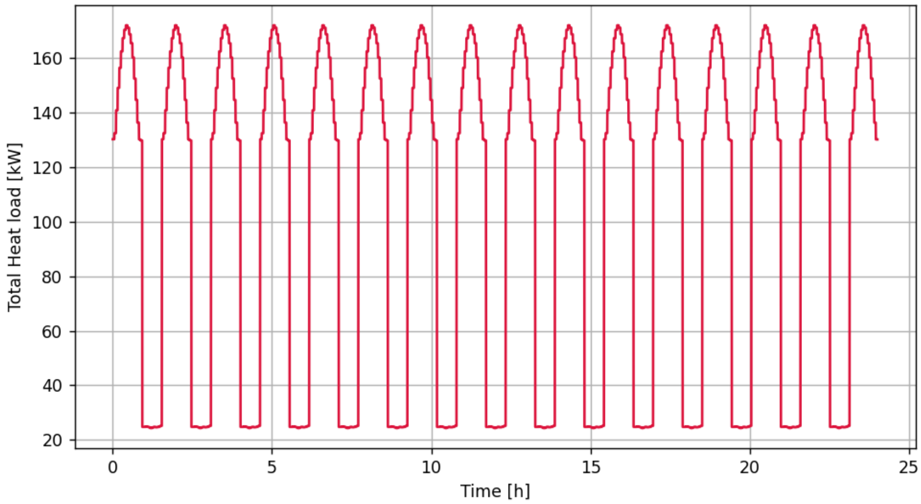

Figure 4.15: Heat load profile of spherical isothermal node for 32 mT of LH2 storage in LEO.

	Maximum	Minimum
Temperature (K)	314	192
Heat load (kW)	172.1	24.3

Table 4.6: Maximum and minimum temperatures and heat load for neutral isothermal spherical node, 32 mT of LH2 storage in LEO.

Unfortunately, there are no heat load profiles provided by Chai for the 32 mT LH2 tank to perform a comparison, however the values in Figure 4.15 have been found using the same heat fluxes as the case in Figure 4.14b. Furthermore, Table 4.6 shows that the node temperatures are almost unchanged with respect to the previous case, confirming their independence from the sphere radius.

4.3.2. Chai case study of LH2 tank and comparison with the Boil-off tool

The just described case of 32 mT of liquid hydrogen storage in LEO has been simulated using the Boil-off tool for a storage duration of 1 Earth year. In particular, the only thermal control system used is the MLI, which has been analysed for several numbers of reflector layers.
The resulting monthly boil-off (Figure 4.16b) and the comparison with Chai (Figure 4.16a) are shown for the 20 layers/cm layer density case.

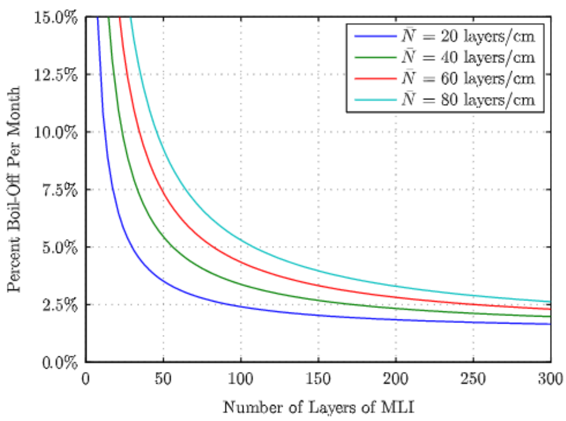

(a) Results from [11].

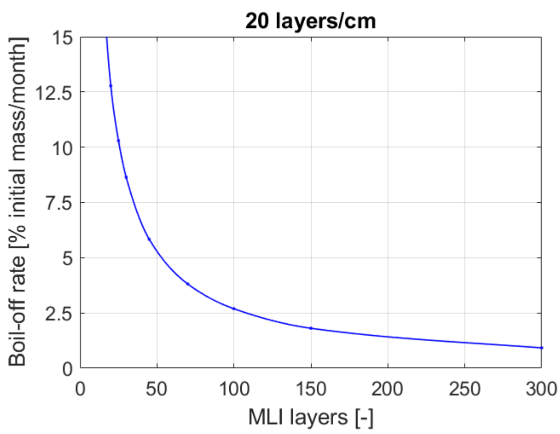

(b) Results from Boil-off tool.

Figure 4.16: Monthly boil-off as a function of number for MLI layers for 32 mT of LH2 storage in LEO.

Boil-off rate [% initial mass/month]							
# MLI	25	30	45	70	100	150	300
Chai	6	5	3.75	2.75	2.5	2	1.5
Boil-off tool	10.3	8.6	5.8	3.8	2.7	1.8	0.9

Table 4.7: Monthly boil-off rates comparison between Chai and Boil-off tool for different MLI layers, 20 layers/cm density.

In particular, a good agreement in terms of trends can be noticed between the Chai and Boil-off tool cases. As for the boil-off rate values, some differences can be found in Table 4.7, which tend to decrease with increasing number for MLI layers.
This difference can be attributed to many causes. First of all, it is not sure what is the tank size selected by Chai for the analysis, as it was guessed here based on the hydrogen mass. The same holds for the storage pressure and temperature. Both these factors may affect the boil-off rates, causing the differences noticed in Figure 4.16.
In addition, it has to be noted that the Boil-off tool always makes a distinction between sunlit and shadow parts of the tank, and this influences the heat loads distribution on the depot. In fact, in case of a single node (as assumed by Chai), the thermal environment definition tool returns an average value of the heat load over the whole surface, including both sunlit and shadow sides. On the other hand, in case two different nodes are used (as assumed by the Boil-off tool), there are two heat load values based on the tank section considered, and they are averaged over a reduced tank surface (half sphere). This means for example that the heat loads on the shadow tank side do not influence the ones on the sunlit side, which as a consequence increase in intensity, resulting in slightly higher boil-off rates.

Last but not least, it can be noticed that for designs with more than 150 MLI layers, the boil-off rates calculated with the Boil-off tool seem to decrease more rapidly than the ones reported by Chai.
This may be attributed to the fact that, when a considerable number of MLI layers is used (more than 100), the conduction effects between reflector and spacers may become so severe to not bring improvements in the propellant boil-off rate anymore. This effect is not accounted for in the Boil-off tool as rarely more than 80 layers are used, while it could be the reason of the ”plateau” in the values from Chai for high layers numbers.

The same comparison as above can be done for the boil-off and MLI mass after one Earth year of storage. This is shown in Figure 4.17. Also in this case a good agreement between the two models has been found. However, it has to be noted that the MLI mass has been calculated using the same relation as [11]. Therefore, the comparison in Figure 4.17 has been done to verify whether the boil-off mass resulting from one Earth year of storage was in agreement with the values reported from Chai. Regarding the differences between the two cases, the considerations made before still apply.

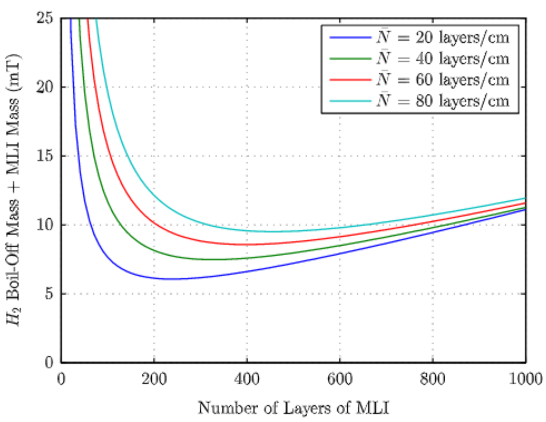

(a) Results from [11].

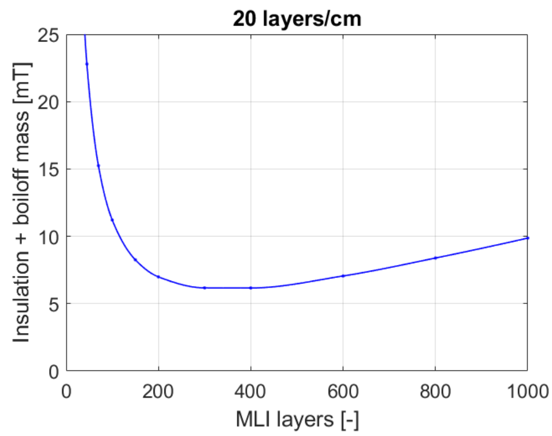

(b) Results from Boil-off tool.

Figure 4.17: Monthly boil-off + MLI mass as a function of number for MLI layers for 32 mT of LH2 storage in LEO.

5

Propellant depot architectures

This chapter is dedicated to the selection of the propellant depot architectures to be analysed in chapter 6. This is done by making combinations of potential depot locations (orbits) with different depot configurations. On the orbit definition side, a brief summary of the propellant depot area of operation in space is first given, to then proceed with the description of the main characteristics of each selected orbit. After that, a selection of propellant depot configurations relevant to the current analysis is made. Finally, the identified options are combined for the final depot architectures definition.

5.1. Cis-Lunar Space

The literature review performed in section 1.2 has pointed out how the selected area of operations for most of the depot-based architectures is the cis-lunar space. This can be defined as the region of space that lies between the Earth and the Moon, including the Moon orbits.
According to [64], this area is the only one considered so far because of two main reasons. First of all, no manned missions have gone beyond this area up until now, and the latest efforts in the space exploration industry are currently focused on going back to the Moon. Second, the LEO-to-GEO region is where most of the satellites and more in general the interest of the space community is focused. Therefore, both these points make the cis-lunar space a particularly suitable location for orbital propellant depots.
A graphical representation of the cis-lunar space is given in Figure 5.1.

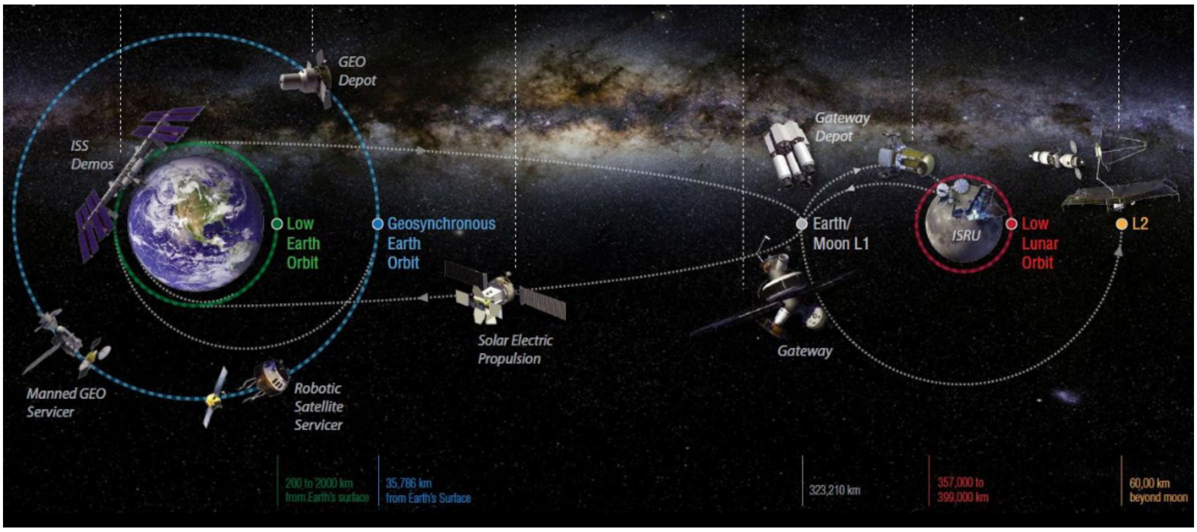

Figure 5.1: Main orbits belonging to the cis-lunar space [65].

In particular, the following main cis-lunar destinations were identified by [66]:

- **Low Earth Orbit (LEO)**. This is the closest orbit to the Earth's surface and a good point of departure for any future deep space mission.
- **Geosynchronous Orbit (GEO)**. These are 24-hours orbits where most of communication satellites operate. GEO satellites are usually first delivered to a Geostationary Transfer Orbit (GTO) by their launcher and then move autonomously to the final orbit.
- **Lagrange Points (L1 and L2)**. These are equilibrium points of the Earth-Moon system that are particularly suitable for cryogenic storage thanks to the cold environment they provide. Moreover, these points are considered gateways to the Solar System because objects placed here are characterized by energies very close to the one needed to escape the Earth's gravitational influence.
- **Low Lunar Orbit (LLO)**. These orbits are more specific for Lunar exploration, as they are used to support operations on the surface of the Moon, such as sample return missions or in-situ propellant production.

For the current analysis, the first three orbits are considered, while the investigation of LLO depots is left for future research. The reason behind this choice is that the selected orbits can be used as support of several space missions with different objectives, thus allowing a broad area of applicability of the results, while Low Lunar Orbits are specific to the Moon's surface operations and their results are therefore applicable to a restricted group of case studies.

A Δv map showing all the velocity changes needed to reach several locations of the cis-lunar space can be found in Figure 5.2. In particular, the most demanding orbit in terms of Δv (around 9.5 km/s) is the LEO. After that, variations in the order of 5 km/s are needed to reach other locations in cis-lunar space. This effect is due to the proximity of the LEO to the Earth surface, which makes the gravitational influence of the Earth on any spacecraft in this orbit particularly strong.

Another important detail is that a transfer to GEO requires more velocity change than the one needed to reach the Earth-Moon L1 point, despite the fact of being the closest between the two. For this reason, sometimes L1 depots could be preferred because of the lower propellant effort needed for station delivery into orbit.

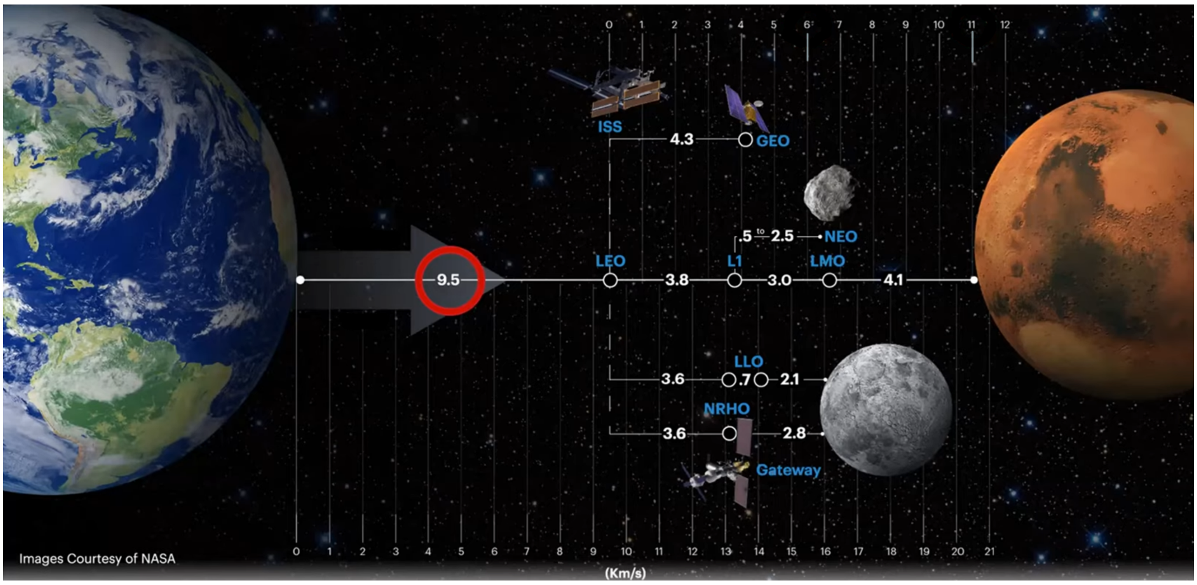

Figure 5.2: Δv map of the cis-lunar space (courtesy of NASA).

5.2. Orbit definition

The orbit definition is an important step to make to correctly define the space thermal environment to be used in the Boil-off tool analysis. It is therefore necessary to determine the required orbital data to be given as input to ESATAN-TMS for the thermal environment characterization. In particular, in order to sufficiently define a mission, the following steps must be followed:

1. **Define the Sun/planet environment**. Some time-dependent parameters like Sun-planet distance, solar declination and Sun's right ascension can be set by defining the mission start date and time. The Sun/Earth environment is the only system considered in the current analysis, however ESATAN-TMS also allows to select any other planet of the Solar System.

2. **Define the orbit**. This is done by setting the following orbital parameters:

   - Inclination $i_{\textbf{orbit}}$
   - Right ascension of the ascending node Ω
   - Argument of periapsis α_p
   - Altitude of perigee H_p and apogee H_a (or eccentricity of the orbit e and Semi major axis a)

3. **Define the spacecraft attitude**. This can be set on ESATAN-TMS by the user. Some examples of different depot attitudes can be found in subsection 4.1.2 for a single tank depot case.
   For the analysis performed here, the depot orientation is defined using pointing vectors and directions. In particular, the depot is first aligned with a primary pointing vector, and then rotated about this vector to best align with a second pointing vector. Both vectors are chosen by the user and they allow to reproduce any depot orientation in orbit.

5.2.1. Low Earth Orbit (LEO)

Low Earth Orbits are usually placed at altitudes that are less than 2000 km above the Earth's surface [17]. They can be either circular or elliptical, with inclinations that vary between 0 (equatorial) and 90 degrees (polar). Inclinations greater than 90 degrees are also possible, and in that case the spacecraft starts to orbit in a direction opposite to Earth's rotation, generating what is called a retrograde orbit. However, these orbits are incredibly demanding in terms of Δv as any spacecraft headed there needs to overcome an eastward velocity component given by the Earth's rotation around its axis.
Another particular class of low Earth orbits is called sun-synchronous, and it is achieved by keeping the orbit plane always at a fixed angle relative to the Sun, so that the spacecraft is always seeing points on Earth with the same local time. For this reason, sun-synchronous orbits are usually used for imaging or weather observations [17]. Being relatively close to the Earth's surface, low Earth orbits have short orbital periods in range of 1.5 to 2 hours.

Because of the high velocity change required to reach LEO (about 9 km/s), these orbits are among the best qualified for a propellant depot placement for cis-lunar operations: this way, the launch vehicle is only loaded with the amount of propellant needed to reach LEO, where the spacecraft is then refuelled to reach farther destinations. Moreover, refueling missions in LEO are also the easiest to accomplish.
For example, [11] already proposed a mission architecture for a manned mission to a Near-Earth Asteroid using a LEO propellant depot. Analogously, [3] identified a LEO propellant depot as an important mission architecture component to enable a permanent human settlement on the Lunar surface.
However, many sources in literature (for example [67]) have pointed out LEO as the worst orbit for a propellant depot operation in terms of thermal environment due to the influence of albedo and planetary fluxes, which increase in intensity with decreasing orbital altitude.

Figure 5.3 shows a representation of the LEO orbit chosen for the space environment analysis, along with its orbital parameters in Table 5.1. Of course, other values for the parameters can be selected as long as they comply with the LEO characteristics, however the choice made here already allows for demonstrating the capabilities of the tool developed.

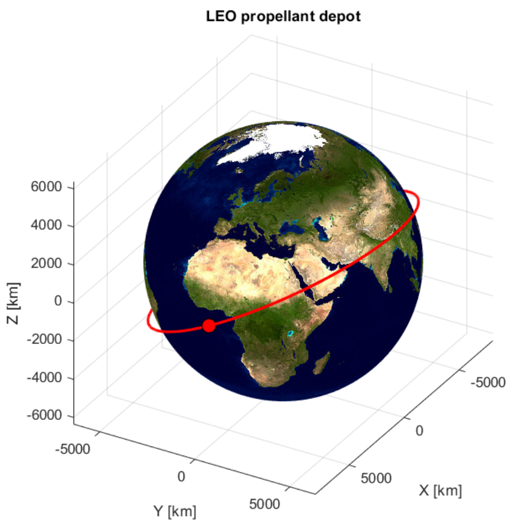

Figure 5.3: Representation of orbit for LEO propellant depot.

Orbit parameter	Value	Details
i_{orbit}	5°	Launched from Guiana Space Centre, Kourou, French Guiana
Ω	0°	Chosen for simplicity
α_p	0°	Not relevant for circular orbit
H_a	400 km	LEO (circular orbit)
H_p	400 km	LEO (circular orbit)

Table 5.1: Orbital parameters for LEO depot.

5.2.2. Geostationary orbit (GEO)

Geostationary orbits have an altitude of 35,786 km, which makes them the highest common type of Earth orbits [17]. They are circular orbits with very low inclinations[1] (less than 10 degrees), and a period equal to the Earth's rotation around its axis, that is 24 hours. This detail makes Geostationary orbits particularly suitable for communication satellites applications.
Figure 5.4 shows the representation of the a GEO orbit, together with its orbital parameters in Table 5.2.

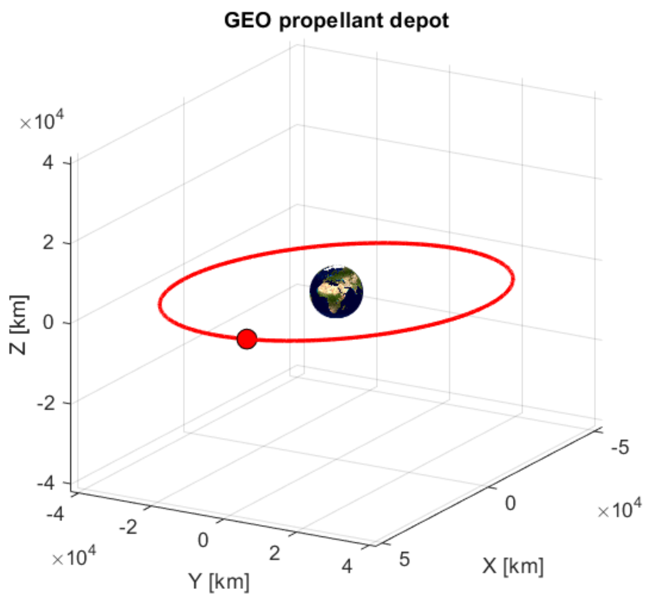

Figure 5.4: Representation of orbit for GEO propellant depot.

Orbit parameter	Value	Details
i_{orbit}	5°	< 10°
Ω	0°	Chosen for simplicity
α_p	0°	Not relevant for circular orbit
H_a	35'786 km	GEO (circular orbit)
H_p	35'786 km	GEO (circular orbit)

Table 5.2: Orbital parameters for GEO depot.

5.2.3. GEO and LEO thermal environments

An example of the thermal environment of the two orbits just described can be found hereby. To the scope of this analysis, the worst-case scenario in terms of heat loads incoming on the depot has been selected, that is when one of the tank sides is continuously oriented towards the Sun. This attitude has been graphically reproduced using ESATAN-TMS and it is shown in Figure 5.5.

[1]Other orbits very similar to GEO are the Geosynchronous Orbits (GSO), which have their same characteristics, but they can have any inclination.

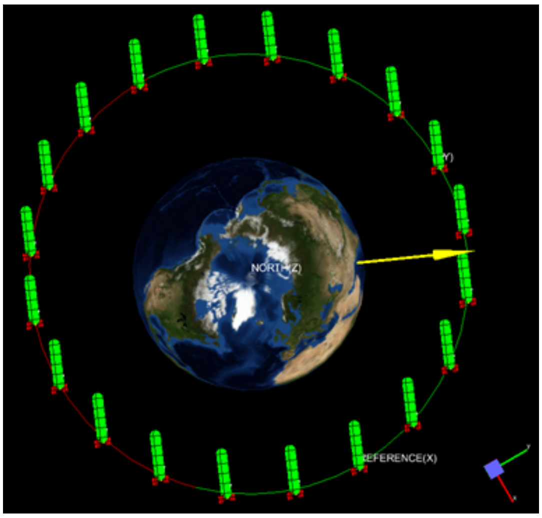

Figure 5.5: Single tank depot orientation along orbit, yellow arrow is pointing at the Sun.

The thermal environments corresponding to this attitude are generated using ESATAN-TMS both for the GEO and LEO orbits defined respectively in Table 5.2 and Table 5.1. The resulting heat loads on the depot are plotted in Figure 5.6 for a total duration of 24 hours, corresponding to one orbit around Earth in GEO and about sixteen in LEO.

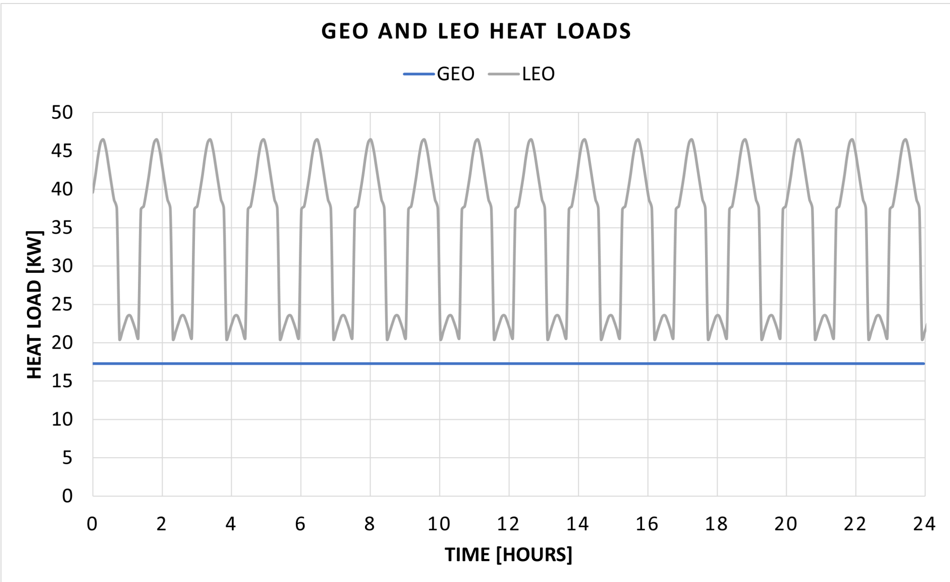

Figure 5.6: GEO and LEO absorbed heat load for single tank depot (optical properties $\alpha = 0.10$, $\varepsilon_{IR} = 0.66$).

For the selected depot attitude, the GEO case is characterized by a constant heat load throughout the orbit, hence the “flat” line. In fact, for this case only the solar radiation has been considered, since planetary and albedo represent less than 2% the total incident heat [17]. The intensity of the solar flux depends in its turn on the planet-Sun distance, which will of course stay constant throughout the orbit. The only way solar heat loads in GEO could change in intensity is either because of the tank orientation (more details are given in subsection 4.1.2), or eclipses. The latter, given the very low inclination of GEO orbits, happen only in specific times known as ”eclipse seasons”, which usually correspond to vernal and autumnal equinox, and for very short times (about 1 hour) [17]. For this reason, eclipses have not been considered in the GEO thermal environment definition, and it is expected that including their effect would further reduce the heat loads on the depot: therefore, the thermal environment definition done in this work can be considered conservative.

On the other hand, the heat loads in LEO orbit are a result of the combined solar, albedo and planetary fluxes on the tank body, and they vary throughout the orbit according to the relative position between the Earth, the Sun and the depot. In particular, this depot in LEO is subjected to daily eclipses, which are represented by the ”dips” in the graph in Figure 5.6.

5.2.4. Earth-Moon Lagrange point L1

The Libration points (also called Lagrange points) are equilibrium positions where the secondary mass of a restricted three-body problem [2], if not subject to other forces, would appear permanently at rest with respect to the other two main bodies [68].
The location of the five Lagrange points of the Earth-Moon system can be found in Figure 5.7. Being these points are fixed relative to the Earth and Moon, they follow circular orbits around the Earth with the same period as the Moon.

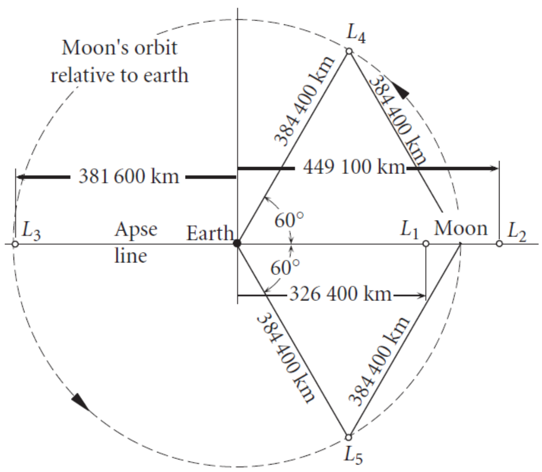

Figure 5.7: Location of the five Lagrange points of the Earth–Moon system. [68]

Placing the depot at the Earth-Moon Libration points comes with several advantages. First of all, the Lagrange points are positions of unstable equilibrium, meaning that every space object reaching those points also leaves them immediately unless it is stabilized by a proper system. This means that the depot would have its neighborhood cleaned up by any object that could potentially disturb its orbit. Moreover, objects located at these points are close to Earth's escape energy, which makes it easy for the spacecraft to leave Earth's gravitational influence. In particular, the L1 point provides global lunar access with no temporal restrictions or the typical Earth departure windows [18], while the L2 point is often considered as a ”gateway” to the Solar System [16].
Finally, the Lagrange points are thermally ideal for a propellant depot location, since the only flux to take into account is the solar one, given the considerable distance from the Earth's surface.
The Earth-Moon Lagrange point L_1 has been deemed particularly suitable as location for orbital propellant depots supporting missions to the lunar surface or to the other planets of the Solar System, such as Mars (examples are given by [16] and [18]). Therefore, this point has been selected for the current analysis.

Figure 5.8 shows the representation of the L1 and L2 orbits for a propellant depot, while the L1 orbital parameters are shown in Table 5.3.

[2]According to [68], a restricted three-body problem is characterized by two bodies m_1 and m_2 in space moving under the action of only their mutual gravitation, and a third body of mass m which is considerably small compared to the primary masses, such that it is safe to assume that this body has no effect on the motion of the primary ones.

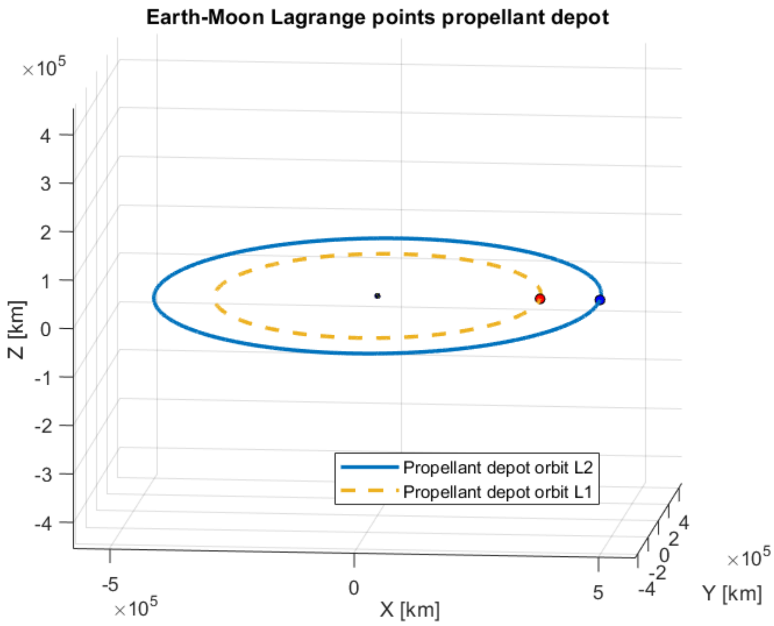

Figure 5.8: Representation of orbits for L1 or L2 propellant depot.

Orbit parameter	Value	Details
i_{orbit}	5.145°	From [69]
Ω	0°	Chosen for simplicity
α_p	0°	Not relevant for circular orbit
H_a	323'210 km	L1 point(circular orbit)
H_p	323'210 km	L1 point(circular orbit)

Table 5.3: Orbital parameters for L1 depot.

Also for the L1 depot case, a radiative case of the single tank thermal environment is simulated using ESATAN-TMS. The results show heat loads matching the ones already obtained for the GEO depot case (Figure 5.6). This was expected as both for the GEO and the L1 case, given the great depot distance from the Earth, the only relevant external flux is the solar, which has about the same intensity for both GEO and L1 orbits. Moreover, both the heat load profiles are constant throughout one orbit, as none of them experiences eclipses during one period.

The similarity found between the GEO and L1 orbits thermal environments brings a great point of advantage for the analysis performed in this work. In fact, this means that all the results found for the GEO case could also be applied to the L1 depot. In other words, the thermal behaviours of the same depot configuration placed in GEO and L1 are alike.
The reason why one should select one location with respect to the other would then depend on the specific requirements of the mission, and on the means available to place the depot in orbit.

5.3. Depot configuration

Once the depot location options are defined, it is possible to proceed with the depot configuration definition. As already described in section 1.2, many depot configurations exist, and their structure mainly depends on the mission requirements (i.e. number of refuelings, mission duration, propellant type). More in particular, two main groups of propellant depots can be identified in literature:

1. **Single tank depot facility**.
   Formed by one fuel and one oxidizer tank, it can be also combined with a propulsion stage [11]. The tank dimensions are chosen depending on the propellant mass that needs to be stored, which in its turn depends on the mission requirements (i.e. Δv to be achieved) and on the O/F ratio of the propellant mixture used.

2. **Propellant multi-tank depot facility**.
   Tank dimensions are ”standardized” at a given volume, and tank number is adjusted in order to meet the O/F requirements [3]. In particular, a quick estimate for the LOX/LH2 tank number ratio can be done. According to NIST [55], at 1 bar, the densities of hydrogen and oxygen at the respective cryogenic temperatures are: $\rho_{LH2} = 71.3\ kg/m^3$ (at 20 K) and $\rho_{LOX} = 1142.1\ kg/m^3$ (at 90K). Taking an O/F ratio of 6 (conservative estimate since it is usually 5.5), it is possible to calculate the number of LH2 tanks for every LOX tank:

$$O/F = \frac{V_{tank}\rho_{LOX}}{n_{LH2}V_{tank}\rho_{LH2}} \longrightarrow n_{LH2} = \frac{\rho_{LOX}}{6\rho_{LH2}} = 2.669 \approx 3$$

   Thus, to keep an O/F ratio of 6, for every liquid oxygen tank, 3 liquid hydrogen tanks need to be allocated, assuming that all the tanks have the same volume.

Following the reasoning above, it comes without saying that there is a huge number of possible configurations that a propellant fuel depot can have. To the scope of the analysis performed in this work, three of them are selected and designed using ESATAN-TMS. The selection of these specific designs has been done by looking at already available options in literature.

The preliminary models of the three designs are shown in Figure 5.9. All the depots are designed for the storage of the hydrolox (LH2/LOX) mixture, and an O/F ratio of 6.

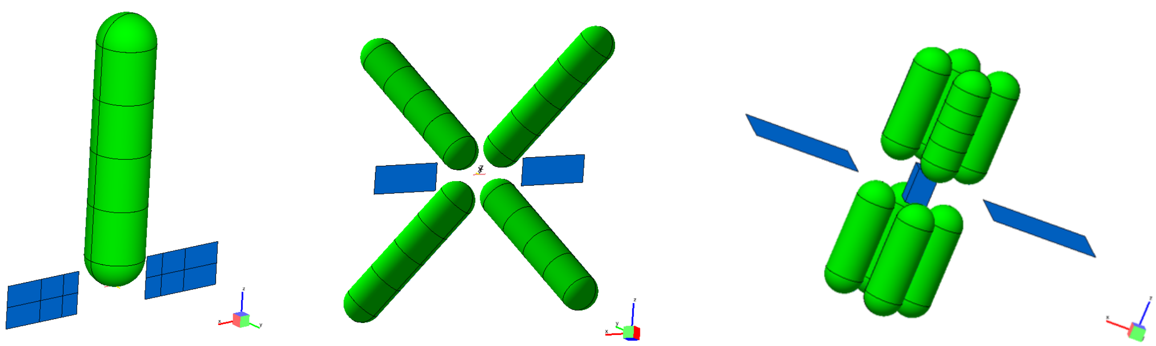

(a) Single tank model. **(b)** Cruciform tank model (4 tanks) **(c)** Eight tank model.

Figure 5.9: Different designs of propellant orbital depot for cryogenic storage of LH2/LOX.

In particular, the single tank model (Figure 5.9a) has been widely studied in literature, two examples are [15] and [11]. The design is usually based on a cryogenic upper stage where the propulsion system is excluded in case the depot itself does not require it, and is able to support one mission at time. It has to be noted that in the ESATAN-TMS model shown here only the hydrogen tank is represented as it is the one object of the analysis, however in the real case this is always coupled with a LOX tank.

A cruciform-like depot station has been proposed by [53], to which the model in Figure 5.9b is inspired. In this case, all the tanks are included in the system, which are 3 for hydrogen and one for oxygen. To the scope of this analysis, the tank dimensions are kept the same as the single tank case, therefore the cruciform tank model is capable of supporting a total of three missions with the same propellant requirements as the single tank model.

Finally, [3] provided a design of a more complex propellant depot station, which is shown in Figure 5.9c. This station is formed by a total of 8 tanks (6 for hydrogen and 2 for oxygen), which are gathered in two groups of four tanks each. Again, each tank of the eight tank model has the same dimensions as the single tank case, meaning that this depot station is capable of supporting a total of six missions with the same propellant requirements as the single tank model.

More details on the three depot station configurations can be found in Table 5.4. The tank capacity and dimensions are taken from the work of [11].

Table 5.4: Orbital propellant depot station details

	Single tank	Cruciform model	Eight tank model
Propellant mass (one mission) LH2 mass (one mission) O/F	225,000 kg 36,600 kg 6		
LOX tank(s) LH2 tank(s)	1 1	1 3	2 6
LH2 tank dimensions LOX tank dimensions	$L = 20\ m,\ D = 5.4\ m$ $L = 4.6\ m,\ D = 5.4\ m$	$L = 20\ m,\ D = 5.4\ m$ $L = 20\ m,\ D = 5.4\ m$	

5.4. Architecture selection

The propellant depot options identified above are combined into architectures shown in the option tree of Figure 5.10. In particular, the they are generated based on combinations of depot locations and configurations. This is needed in order to define the tool ”boundary condition”, which is in this case the thermal environment model generated using ESATAN-TMS.

Once this has been set, the Boil-off tool can be used to analyze the thermal performance of the tank for a specific architecture. It has to be noted that, whenever the user wishes to change the thermal environment, or the depot geometry and orientation, the ESATAN-TMS model should be adapted accordingly.

Figure 5.10 shows that the available depot locations and configurations generate four final distinct architectures, them being LEO and GEO single and multi-tank depots. The ”reduction” of study cases shown in the option tree can be related to the fact that some of the options above can be coupled thanks to similarities.

In particular, it has already been explained that the same thermal environment definition holds for the GEO and L1 orbits when only solar fluxes are considered. This assumption therefore allows to group together these two depot locations, which share the same results from the thermal simulations.

As for the depot configuration, ESATAN-TMS has shown agreement between the heat load profiles on the single tank model (Figure 5.9a) and on each tank in the cruciform model (Figure 5.9b), for any depot location. This agreement stands only in case the same depot orientation is considered for both models, and it allows to perform one single architecture analysis for both the cruciform and single tank depots.

On the other hand, different locations within the eight tank depot results in different heat loads incoming on the tanks. A specific architecture study is thus been dedicated to this specific depot configuration in order to study the thermal behaviour of each tank of the assembly.

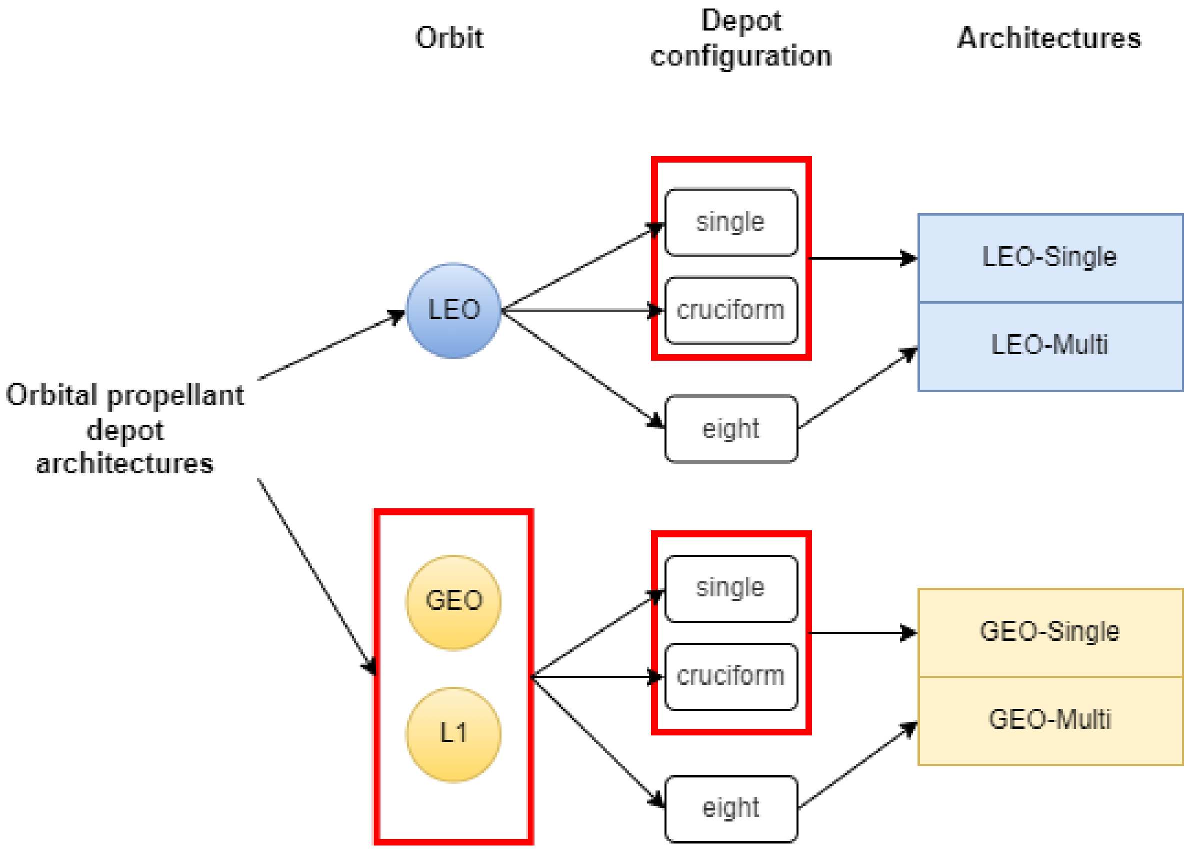

Figure 5.10: Propellant depot architectures option tree.

6 Architectures analysis and results

This chapter is dedicated to the analysis of the mission architectures selected in section 5.4. The two parameters investigated for each architecture are the monthly boil-off rate, and the combination between insulation and boil-off mass for different mission durations. The objective of the analysis is to identify the design option that returns the most mass efficient values.
It is noted that the tank mass is not included in the analysis as it can be added once the simulations are done. In fact, as already explained in subsection 4.2.1, it is safe to remove the tank wall thermal node from the nodal network without losing in accuracy, thus allowing the applicability of the results to different tank materials without the need to perform separate simulations for each option.
Therefore, once the tank mass is removed, the components that contribute to the majority of the depot station total mass are, as already said, the insulation mass, and the propellant boil-off mass. In particular, the latter is important because it determines the availability of the propellant in the tank after a specific time in orbit, and therefore the payload capability that the depot itself is able to offer to any spacecraft that needs to be refueled.

The analysis in this chapter is set as follows: first the single tank model in Geostationary orbit is studied for several thermal control design options, all defined in chapter 3. The same procedure is then applied to the Low Earth Orbit depot case, and a comparison between the two architectures is made. In addition, a multi-tank depot case is analysed. In this regard, the eight tank model is of particular interest because of the potential shadowing effect that specific tanks could receive from the others in the depot.

6.1. GEO propellant depot: single tank model

The first object of the analysis is the single tank depot with one of its sides continuously facing the Sun during the orbit. This case is selected because it represents one of the most critical cases in terms of incoming heat on the hydrogen tank, as proven in subsection 4.1.2.
The depot is designed for the storage of 34.6 mT of hydrogen, which is the propellant capability expected to be required for a manned mission to a Near Earth Asteroid (NEA) [11]. This propellant capacity has only been chosen to the scope of the thermal analysis to be performed here, and it can be changed based on the mission requirements.
The tank structure is formed by a cylindrical body with spherical end-caps, with a radius of 2.7 m and a total height of 25.8 m. The depot structure and orientation are graphically represented in Figure 6.1 using ESATAN-TMS.

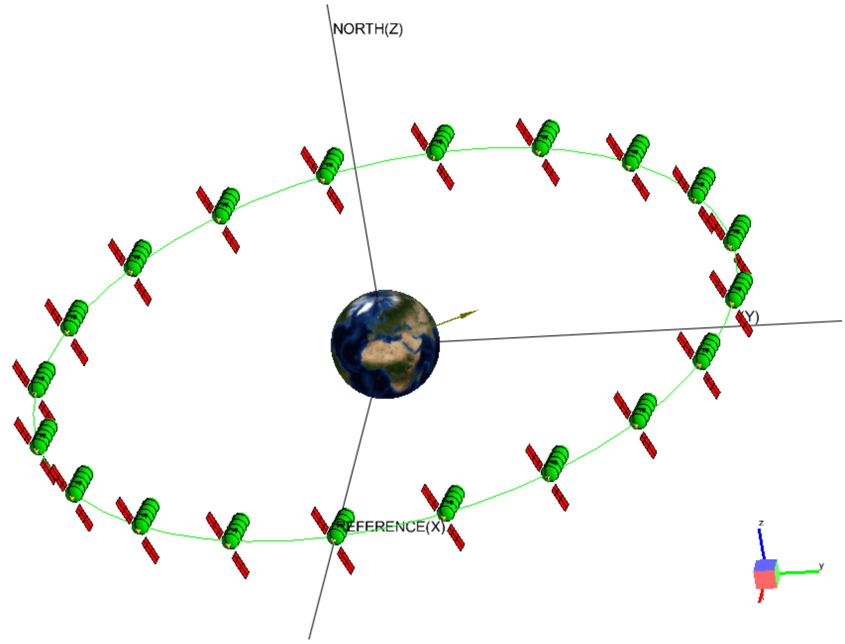

Figure 6.1: ESATAN-TMS orbit display, tank left side facing the Sun. Sun position is indicated by the yellow vector in the figure.

A more detailed list of all the inputs is given in Table 6.1, where MLI and tank data are taken from [37]. Storage duration considered in the analysis is from 1 month up to 12 months of continuous storage (without any refuelling) in orbit, as these are expected storage durations for orbital propellant depots according to [9].

Table 6.1: GEO single tank analysis program inputs

Storage of	34.6 mT, Liquid Hydrogen 1.3 bar @ saturation conditions, 21 K max 3 bar	
MLI	Unperforated, double Aluminized Mylar shield with Dacron net spacers Mylar shield $\rho_m = 0.00881\ kg/m^2$, $t_m = 0.0064\ mm$ Spacer $\rho_s = 0.00635\ kg/m^2$, $t_s = 0.16\ mm$ Optical properties : outer $\alpha = 0.10$, $\varepsilon = 0.66$, inner* $\varepsilon = 0.03$	 [11] [11] [32]

* defined by [32] as the typical value of the IR emittance of a single reflector layer. This holds within the temperature range of $20\ K$ to $370\ K$ (continuous) or $425\ K$ (intermittent)

6.1.1. First run: Uniform-Density Multi-Layer Insulation (UDMLI)

For the Uniform-Density MLI case, it is first chosen to study the thermal performance of a tank covered by a number of MLI layers that goes from 10 to 150, with layer densities of 16 layers/cm and 40 layers/cm. These different densities also affect the thickness of the MLI according to Equation 3.7. This effect is shown in Table 6.2.

Figure 6.2 shows the percent of monthly boil-off (with respect to initial stored mass) as a function of the number of MLI layers and for the two different layer densities previously indicated, together with the total insulation and boil-off mass after 1 Earth year of storage in Geostationary orbit.

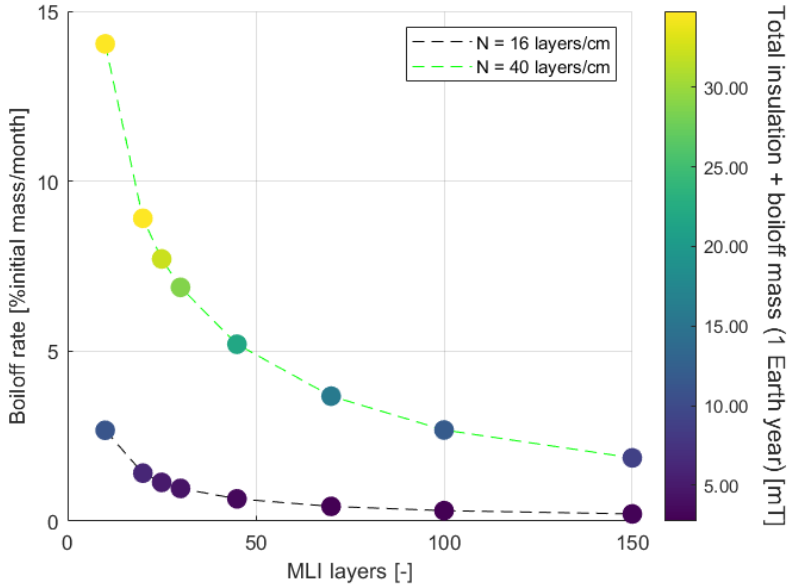

Figure 6.2: Monthly boil-off (wrt initial mass) and insulation + boil-off mass (after 1 year) vs number of MLI layers and MLI density for 34.6 mT of LH2 storage in GEO.

# MLI layers	MLI thickness [mm]	
	40 layers/cm	16 layers/cm
10	2.5	6.25
20	5	12.5
25	6.25	15.6
30	7.5	18.75
45	11.25	28.1
70	17.5	43.75
100	25	62.5
150	37.5	93.75

Table 6.2: Details on MLI thickness vs number of MLI layers for two layer densities.

As expected, reducing the layer density indeed results in lower boil-off rates for the liquid hydrogen. This is because using a lower layer density reduces the conductive heat transfer between the single layers, being them in this case more distant from one another [11]. However, a lower layer density also creates more thickness for the MLI and hence a different outer dimension for the depot. According to [70], for the boundary temperatures of liquid hydrogen storage (between 20 K and 300 K), an efficient thermal insulation is achieved with layer densities of about 20 layers/cm. Therefore, the density of 16 layers/cm is chosen to continue with in this analysis.

From Figure 6.2, it also is possible to notice that the heaviest designs are located on the left side of the plot, which correspond to the designs with the least number of MLI layers. While having less MLI layers would be beneficial in terms of insulation mass, the same does not hold for the boil-off mass. In fact, less MLI layers would allow more external thermal radiation to penetrate into the tank, thus increasing the heat leak and the boil-off. On the other hand, it would not be beneficial as well to use too many MLI layers, as this would result in a system with a huge insulation mass penalty. It is thus necessary to identify an optimal combination of number of MLI layers and boil-off that would return the lowest mass value.

This mass comparison is done in Figure 6.3 for the 16 layers/cm density case, where the total insulation and boil-off mass is plotted as function of the number of MLI layers for different storage durations of liquid hydrogen, from 1 up to 6 months.

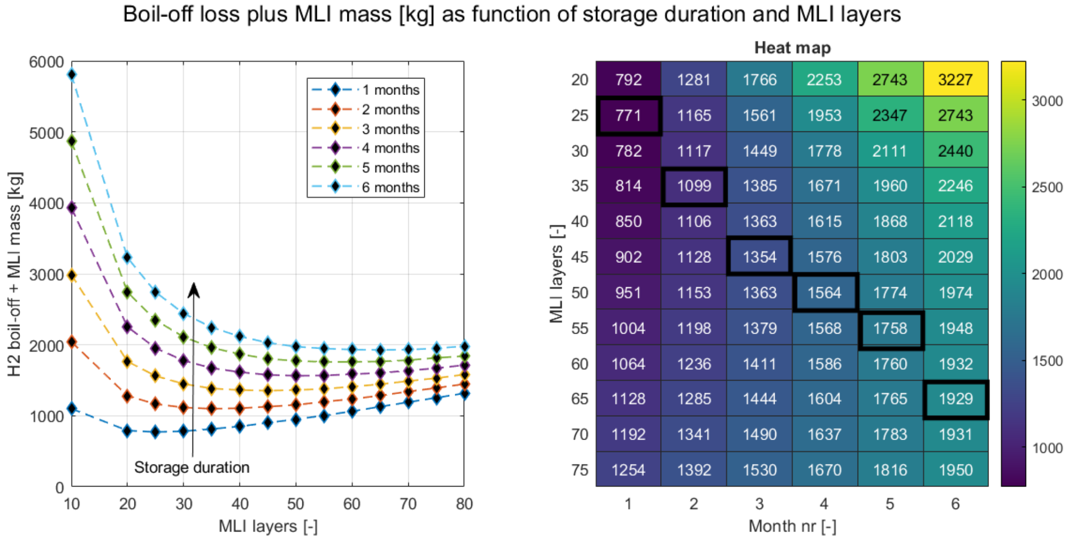

Figure 6.3: Boil-off + insulation mass vs number of MLI layers and storage duration, layer density of 16 layers/cm, 34.6 mT of LH2 storage in GEO.

From Figure 6.3 it is noticed that each curve has a minimum, corresponding to the most mass efficient design, and that this minimum slowly shifts to the right as the storage duration increases. This ”shift” is also confirmed in the heat map on the right of Figure 6.3, where it is clear that the darker region is moving downwards (increasing number of MLI layers) when moving from the left to the right side of the plot (increasing storage duration). In particular, the designs that correspond to the lowest mass are highlighted.

The previous analysis is also performed for a storage duration of 1 Earth year. The boil-off and MLI mass contributions are separately shown in the bar graph of Figure 6.4, together with intermediate values corresponding to the boil-off mass after 1, 3, and 6 months of storage.

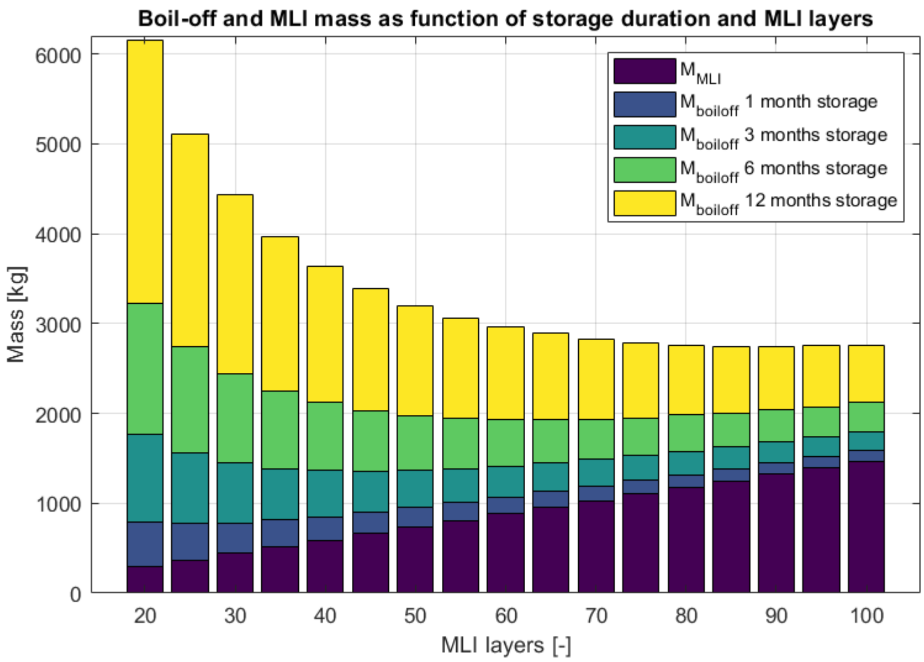

Figure 6.4: Bar graph insulation and boil-off mass vs number of MLI layers, layer density of 16 layers/cm, 34.6 mT of LH2 storage in GEO.

The bar graph clearly shows that the MLI mass increases with increasing number of layers, whereas the boil-off mass reduces. For the 12 months storage duration, the most mass efficient design is achieved with more than 80 number of layers. However this is not investigated further as the MLI number of layers is usually limited to 80 because of manufacturing difficulties. This was confirmed by [71], according to whom there is no documented literature showing MLI blankets that employ more than 80 layers.

A summary of the most mass efficient designs, together with their monthly boil-off rates, based on storage duration in orbit can be found in Table 6.3.

Table 6.3: Most mass efficient designs for storage of 34.6 mT of LH2, GEO depot, UDMLI, 16 layers/cm.

Storage duration [months]	1	2	3	4	5	6	12
# MLI layers	25	35	45	50	55	65	80
MLI thickness	15.6 mm	21.8 mm	28.1 mm	31.2 mm	34.4 mm	40.6 mm	50 mm
MLI mass [kg]	368	515	662	735	809	956	1177
Boil-off mass [kg]	403	584	692	829	949	973	1585
Insulation + boil-off mass [kg]	**771**	**1099**	**1354**	**1564**	**1758**	**1929**	**2762**
Monthly boil-off rate [wrt initial mass]	1.17 %	0.83 %	0.67 %	0.60 %	0.55 %	0.47 %	0.38%

6.1.2. Second run: Variable-Density Multi-Layer Insulation (VDMLI)

The UDMLI design options are now applied to the Variable Density MLI case. In particular, all the design options corresponding to the 16 layers/cm density are converted to their respective optimized VDMLI case following the procedure explained in subsection 3.3.1. An example of the structure of the different variable density MLI designs is shown in Table 6.4. It can already be noticed that, for the same total number of MLI layers, the VDMLI configurations correspond to thicker designs than the UDMLI (see Table 6.3 for comparison), as a consequence of the reduced density of the middle and inner MLI sectors.

Table 6.4: Optimal Variable Density MLI cases, with 16 layers/cm as outer layer density.

Tot # layers	20	25	30	35	40	45	50	55	60	65
Outer layer density	16 [layers/cm]									
# outer MLI layers	10	13	15	18	20	23	25	28	30	33
Outer MLI thickness [mm]	6.25	8.13	9.38	11.25	12.50	14.38	15.63	17.50	18.75	20.63
Middle layer density [layers/cm]	11 [layers/cm]									
# middle MLI layers	7	9	10	12	13	15	17	19	20	22
Middle MLI thickness [mm]	6.56	8.44	9.38	11.25	12.19	14.06	15.94	17.81	18.75	20.63
Inner layer density [layers/cm]	5 [layers/cm]									
# inner MLI layers	3	3	5	5	7	7	8	8	10	10
Inner MLI thickness [mm]	5.63	5.63	9.38	9.38	13.13	13.13	15.00	15.00	18.75	18.75
Total MLI thickness [mm]	18.44	22.19	28.13	31.88	37.81	41.56	46.56	50.31	56.25	60.00

The analysis is made for design options that have a total layers number from 20 up to 80, for storage durations that go from 1 month to 1 Earth year. The results for the first 6 months are shown in Figure 6.5. All the design options correspond to the same VDMLI layer density distribution: 16 layers/cm for the outer layer (S3), 11 layers/cm for the middle layer (S2), and 5 layers/cm for the inner layer (S1), which is also the optimal distribution.

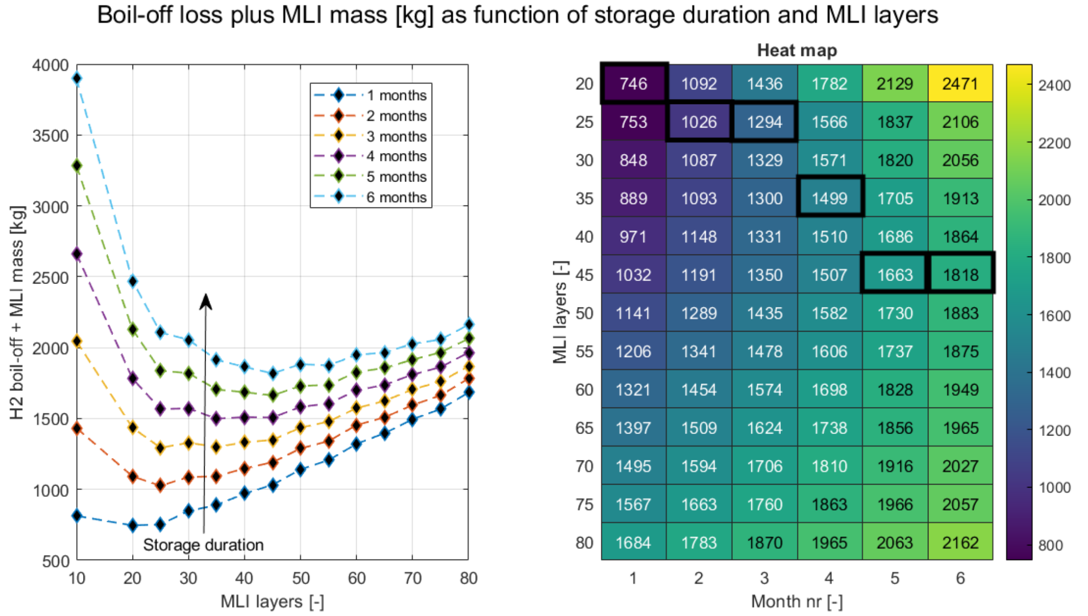

Figure 6.5: Boil-off and insulation mass as a function of number of MLI layers and storage duration, Variable Density MLI, 34.6 mT of LH2 storage in GEO.

The plot on the left of Figure 6.5 is shifted down compared to the UDMLI (Figure 6.3), meaning that the insulation and boil-off mass are less for the VDMLI case. Moreover, contrarily to the UDMLI case, from the heat map on the right, it is possible to see that the lightest design options correspond to insulation solutions that employ less MLI layers (darker region is shifted up). This is expected as VDMLI would reduce the heat leak through the insulation layers, meaning that the same performance is achieved with less layers.

A summary of the results can be found in Table 6.5, where first a comparison between UDMLI and VDMLI designs with the same layers number is done, and then the best design options for VDMLI are shown. Results for the 1 Earth year storage are also included.

Table 6.5: Most mass efficient designs for storage of 34.6 mT of LH2, GEO depot, Uniform and Variable Density MLI.

Storage duration [months]		1	2	3	4	5	6	12
Comparison with best UDMLI designs								
# MLI layers		25	35	45	50	55	65	80
BO + MLI mass [kg]	UDMLI	771	1099	1354	1564	1758	1929	2762
	VDMLI	753	1093	1350	1582	1737	1965	2726
Difference* [%]		-2%	-0.5%	-0.3%	+1%	-1%	+2%	-1%
Best VDMLI designs								
# MLI layers		20	25	25	35	45	45	65
MLI mass [kg]		398	483	483	690	881	881	1295
Boil-off mass [kg]		348	543	811	809	782	937	1360
Insulation + boil-off mass [kg]		**746**	**1026**	**1294**	**1499**	**1663**	**1818**	**2655**
Difference* [%]		-3%	-7%	-4%	-4%	-5%	-6%	-4 %

* indicates the percentage increase or decrease by the UDMLI case calculated as:
$(M_{\text{MLI+BO, VDMLI}} - M_{\text{MLI+BO, UDMLI}}) \cdot 100/M_{\text{MLI+BO, UDMLI}}$

From the first section of Table 6.5 it is possible to notice that a VDMLI design would not bring

considerable improvements in terms of system mass when compared to an UDMLI design with the same total number of layers: the percentage difference is oscillating between a minimum of - 3% and a maximum of 2 %. This is because the VDMLI design requires more insulation mass than the UDMLI, thus outbalancing the boil-off mass reduction.
The real advantage of using a VDMLI configuration is that less layers are employed to achieve the most mass efficient design. This is shown in the second section of Table 6.5, where the most mass efficient VDMLI designs are formed by less layers than the UDMLI and bring mass improvements from 3 up to 7 %.

The comparison between the UDMLI and VDMLI mass for different number of layers is shown in Figure 6.6.

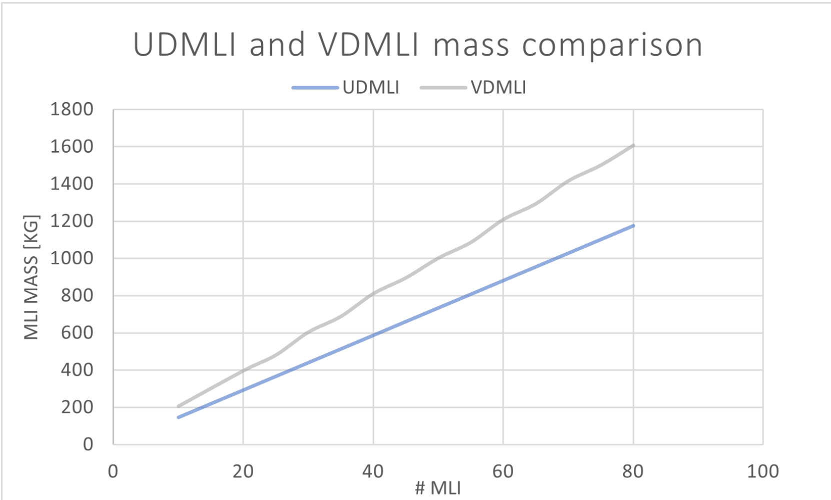

Figure 6.6: Uniform and Variable Density MLI mass comparison with varying reflector layers number.

The mass difference between UDMLI and VDMLI is due to the increased number of spacers needed in between the reflective layers in the lower density MLI regions. This effect has been explained in detail by [31], and is shown in Figure 6.7, where VDMLI (left) and UDMLI (right) designs are compared. In the figure, the solid lines represent the reflector layers (which are the actual MLI layers), while the dashed lines correspond to the spacers.
For example, the MLI sector characterized by one reflector layer every 6 spacers (1:6) corresponds to a low layer density sector. In fact, MLI segments with a low $\overline{N}$ have less reflector layers per centimeter of insulation, thus requiring more spacers to keep the reflector layers at the desired distance. It comes without saying that the lower the layer density, the more the needed spacers.

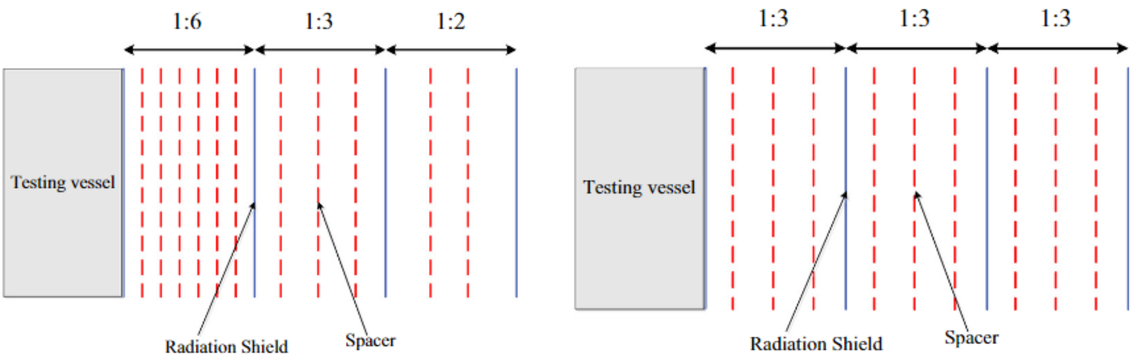

Figure 6.7: Schematic of Variable-Density MLI (left) and Uniform-Density MLI (right) configurations [31].

Assuming the same number of reflector layers, a design like the one on the left of Figure 6.7 indeed requires a higher number of spacers in the inner regions due to the decreased layer density. On the contrary, the UDMLI design on the right has a constant density throughout all the insulation thickness, thus requiring less spacers and reducing the total insulation mass.

The number of spacers is therefore variable between one insulation structure and the other, and this mainly depends on the MLI layer density ($\overline{N}$). This is confirmed by Equation 6.1, which is obtained from the MLI mass relation (Equation 3.10) and indicates the number of spacers needed per reflector layer.

$$\text{spacers/reflector layer} = \frac{1}{t_s}\left(\frac{1}{100\overline{N}} - t_m\right) \tag{6.1}$$

In particular, Equation 6.1 confirms that, assuming the same reflector and spacer thickness, lower MLI layer densities $\overline{N}$ increase the number of spacers needed for each reflector layer.

6.1.3. Third run: Vapor Cooled Shield (VCS)

Finally, a vapor cooled shield is added to the previously identified VDMLI best design cases. As already said in subsection 3.3.3, an aluminum shield is inserted through the middle density MLI sector. This layout guarantees that the beneficial effects that the VCS brings in terms of heat leak are best exploited. The geometric parameters selected for the shield are taken from [23] and are shown in Table 6.6.

Table 6.6: Vapor cooled shield geometric parameters.

VCS shield data	
Shield material	5083 Aluminum alloy, density of $2660\ kg/m^3$
Tube diameter	11.7 mm
Shield wall thickness	0.1 mm

The results of the analysis are shown in Table 6.7. For the chosen tank dimensions, adding an aluminum shield to the design increases the insulation mass of about 120 kg. According to [23], the tube mass accounts for about 22 % of the total VCS system mass, yielding to an expected VCS mass penalty of 150 kg.

Table 6.7: Most mass efficient designs for storage of 34.6 mT of LH2, GEO single depot, VDMLI+VCS.

Storage duration [months]		1	2	3	4	5	6	12
# MLI layers		20	25	25	35	45	45	65
MLI mass [kg]		398	483	483	690	881	881	1295
Boil-off mass [kg]	VDMLI	348	543	811	809	782	937	1360
	VCS	318	483	726	713	644	786	1071
Difference* [%]		-9%	-11%	-10%	-12%	-18%	-16%	-21%
Total VDMLI mass [kg]		746	1026	1294	1499	1663	1818	2655
Total VCS mass (w/ shield) [kg]		**866**	**1116**	**1359**	**1553**	**1675**	**1817**	**2516**
Difference [%]**		+16%	+9%	+5%	+ 4%	+0.7%	0%	-5%

*$(M_{\text{BO, VCS}} - M_{\text{BO, VDMLI}}) \cdot 100/M_{\text{BO, VDMLI}}$,**$(M_{\text{tot, VCS}} - M_{\text{tot, VDMLI}}) \cdot 100/M_{\text{tot, VDMLI}}$

As expected, adding a vapor cooled shield reduces the boil-off mass of the liquid hydrogen stored in the tank with respect to the case without, with differences that to up to 20 % for 1 Earth year of storage (shown in the first section of Table 6.7). However, choosing this thermal control option starts to bring total mass reductions (insulation + boil-off) only for storage durations longer than 6 months, as adding the shield introduces a mass penalty in the thermal insulation design. This is shown in the second section of Table 6.7.

Therefore, VCS in GEO would return mass efficient designs only after at least 6 months of storage if both insulation and boil-off mass are a concern. In case one would be interested in the design which would give the lowest boil-off mass, then VCS always outperforms VDMLI.

6.2. LEO propellant depot: single tank model

The same analysis as above is performed for a LEO depot case. As stated before, the relevance of this case lies in the extreme thermal environment the depot is subjected to, since not only solar (like the GEO case), but also albedo and planetary radiation contribute to the thermal fluxes incoming in the tank.
The effect of the added fluxes can already be seen in the monthly boil-off rates, which indeed increase compared to GEO, as shown in Figure 6.8a.

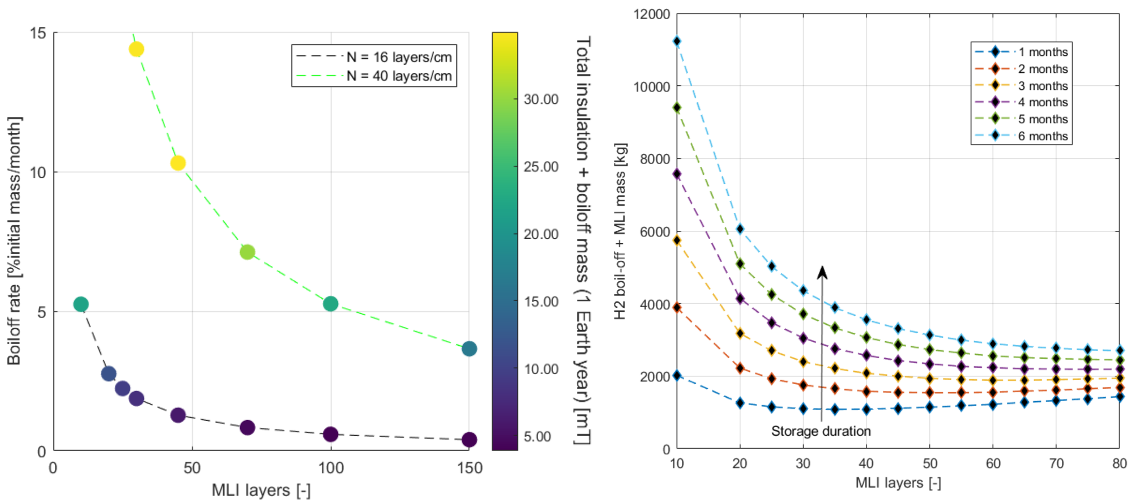

(a) Monthly boil-off (wrt initial mass) and insulation + boil-off mass (after 1 year) for different MLI layer densities.

(b) Boil-off + MLI mass vs number of MLI layers for storage durations from 1 to 6 months, 16 layers/cm density.

Figure 6.8: Monthly boil-off and insulation + boil-off mass vs number of MLI layers for 34.6 mT of LH2 storage in LEO.

For the UDMLI case, the boil-off and insulation mass combination (see Figure 6.8b) shows the same trends as the GEO case, with the difference that the plots are shifted up, reaching an upper limit for the insulation and boil-off mass of about 12 mT. This is expected as, for the same MLI layers and thus same insulation mass, the boil-off mass is more for LEO due to the higher monthly rates. Consequently, the most mass efficient designs (plot minimum) are shifted to the right, meaning that more MLI layers are needed to achieve the best mass balance.

The bar graph in Figure 6.9 shows the separate contributions of MLI and boil-off mass for different storage durations. Also in this case the MLI mass increases with increasing number of layers, while the boil-off mass reduces. However, the plot also shows that the MLI mass makes up to a smaller fraction of the total mass compared to the GEO case. For the 12 months storage duration, the most mass efficient design is achieved again with more than 80 layers.

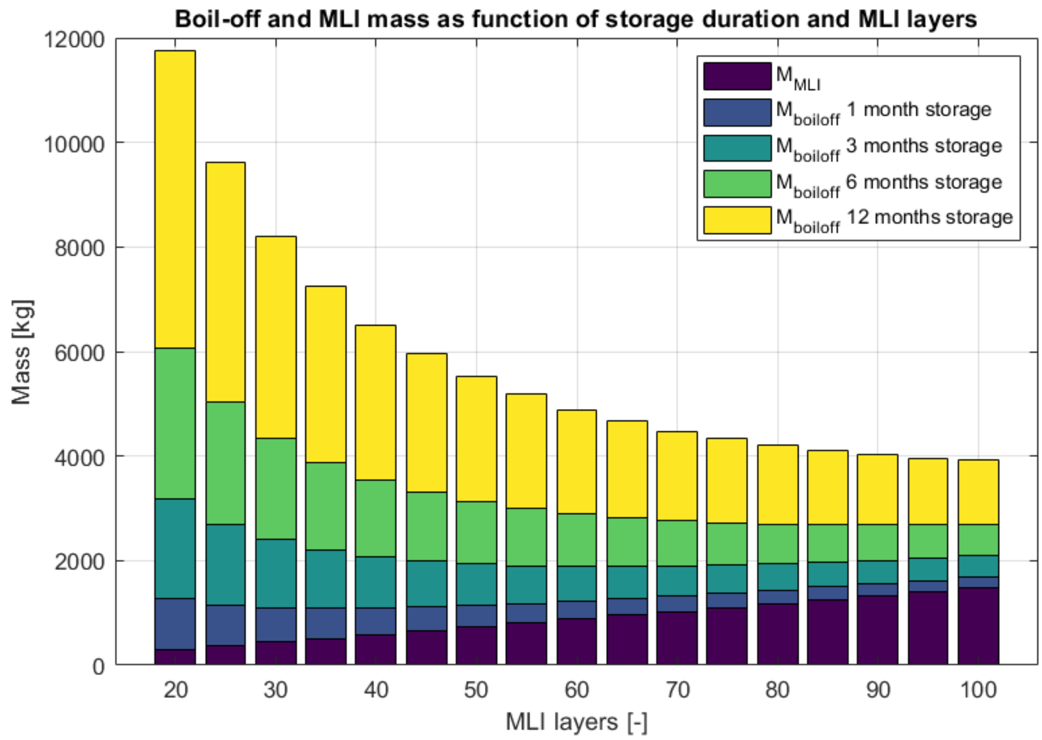

Figure 6.9: Bar graph nsulation and boil-off mass vs number of MLI layers, layer density of 16 layers/cm, 34.6 mT of LH2 storage (1 Earth year) in LEO.

A summary of the most efficient design cases identified for the UDMLI in LEO is given in Table 6.8, together with the UDMLI system mass break-down.

Table 6.8: Most mass efficient designs for storage of 34.6 mT of LH2, LEO depot, UDMLI, 16 layers/cm.

Storage duration [months]	1	2	3	4	5	6	12
# MLI layers	35	50	60	75	80	80	150
MLI thickness [mm]	21.9	31.3	37.5	46.9	50	50	93.8
MLI mass [kg]	515	735	882	1103	1177	1177	2206
Boil-off mass [kg]	568	809	1008	1085	1272	1523	1647
Insulation + boil-off mass [kg]	**1083**	**1544**	**1890**	**2188**	**2449**	**2700**	**3853**
Monthly boil-off rate [wrt initial mass]	1.64 %	1.17 %	0.97 %	0.78 %	0.74 %	0.73 %	0.40 %

As expected, heavier MLI designs than GEO are needed for the depot placed in LEO because of the more critical fluxes that the tank is exposed to. In particular, in case of 1 Earth year of storage, the lowest mass design is achieved with 150 reflector layers. As already stated above, according to [11] this would exceed the practical limit of 80, therefore it is necessary to assess whether applying the other design options (that is VDMLI and VCS) reduces the needed number of MLI layers.

6.2.1. Variable Density Multi Layer Insulation and Vapor Cooled Shields

The same procedure as the GEO depot case is followed for the VDMLI and VCS case studies in LEO. The resulting most efficient mass designs are shown in Table 6.9.
First of all, also here the VDMLI option allows to achieve a better thermal performance by using less reflector layers than the UDMLI, therefore leading lo lighter designs in terms of MLI mass. Especially for 1 year of storage, using VDMLI would reduce the required layers from 150 to 75, thus complying with the limit value of 80.

Table 6.9: Most mass efficient designs for storage of 34.6 mT of LH2, LEO depot, VDMLI and VCS.

Storage duration [months]		1	2	3	4	5	6	12
# MLI layers		25	35	45	45	55	55	75
MLI mass [kg]		483	690	881	881	1088	1088	1486
Boil-off mass [kg]	VDMLI	517	771	888	1182	1235	1481	2199
	VCS	424	595	655	859	850	1026	1400
Difference* [%]		-18 %	-23 %	-26 %	-27 %	-31 %	-31 %	-36 %
Total VDMLI mass [kg]		**1000**	**1461**	**1769**	**2063**	**2323**	**2569**	**3685**
Total VCS mass (w/ shield) [kg]		**1057**	**1435**	**1686**	**1890**	**2088**	**2264**	**3036**
Difference [%]**		+6%	-2%	-5%	-8%	-10%	-12%	-18%

$^*(M_{\text{BO, VCS}} - M_{\text{BO, VDMLI}}) \cdot 100/M_{\text{BO, VDMLI}}$,$^{**}(M_{\text{tot, VCS}} - M_{\text{tot, VDMLI}}) \cdot 100/M_{\text{tot, VDMLI}}$

It is clear that introducing a vapor shield reduces the boil-off mass with respect to the case of VDMLI only. This is shown in the first section of Table 6.9, where the boil-off mass reduction when using VCS goes from 18 % for 1 month of storage up to 36 % for 12 months. This confirms that the VCS design is always the best performing solution in case boil-off mass only is a concern. As for the total system mass, the use of VCS in LEO starts to bring benefits already after two months of storage.

6.3. Single tank architectures comparison

Figure 6.10 shows the monthly boil-off rates of all the design options analysed for the GEO and the LEO depots as a function of the number of MLI layers. All the options correspond to a MLI layer density of 16 layers/cm, which for the VDMLI case corresponds to the density of the outer sector.

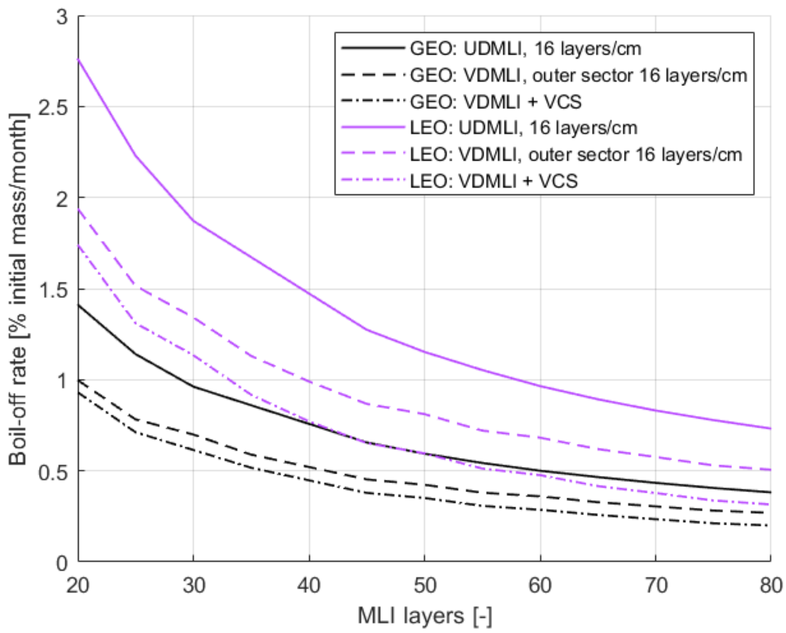

Figure 6.10: Boil-off rates comparison between GEO and LEO for all design options, 34.6 mT of LH2 storage.

Being the LEO case the most critical in terms of external thermal fluxes, the resulting boil-off rates are higher than a depot placed in GEO. Indeed, using VDMLI and VCS reduces the boil-off rates for both cases, and this can be seen in the solid curves shifting down in Figure 6.10.
Furthermore, two more effects can be noticed. First, the GEO designs almost always return less boil-off

than LEO, with the exception of MLI blankets formed by more than 50 layers, after which a VCS LEO design results in less boil-off than a UDMLI GEO design.
The second effect concerns the VDMLI and VCS designs for both GEO and LEO. It is in fact possible to notice that the boil-off rates curves for these options (dashed and dashdotted lines) are closer for the GEO case than the LEO. This is expected as the beneficial effect of VCS on boil-off is more noticeable in case of orbits with more critical heat loads like LEO.

The best design options for all the analysed storage durations are found in Figure 6.11, for both the GEO and LEO case. In particular, the total mass for each design option in the plot is divided into insulation mass (patterned bars) and boil-off mass (colored bars). It has to be noted that each design option in the plot corresponds to different total numbers of MLI layers, as the most mass efficient designs vary based on the storage duration. Therefore, more details on the MLI structure of the best design options shown in Figure 6.11 are found in Table 6.10.

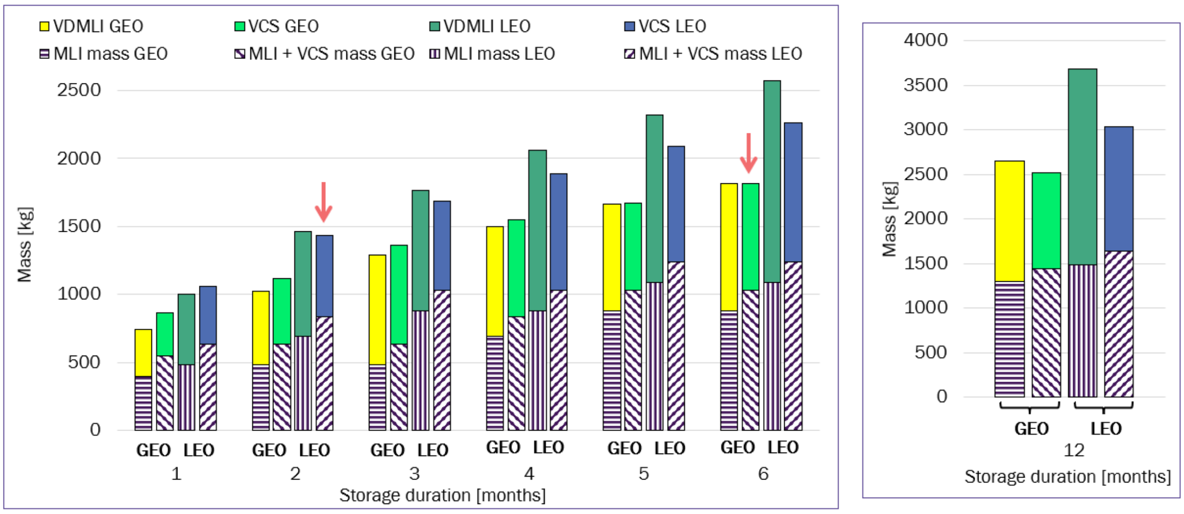

Figure 6.11: Best design options for GEO and LEO single tank depot cases.

CASE	**# MLI**						
Months	1	2	3	4	5	6	12
GEO	20	25	25	35	45	45	65
LEO	25	35	45	45	55	55	75

Table 6.10: Details on MLI layers number for best design options for GEO and LEO cases.

Figure 6.11 also shows that, in order for the VCS to become advantageous in terms of system mass, a certain storage duration needs to pass. This corresponds to the points where the VDMLI and VCS options reach the same bar height in Figure 6.11, which is at least 6 months for a GEO depot, while it is reduced to 2 months in case of LEO (both indicated by the arrows). This effect can be explained by the more critical thermal environment the LEO depot is in: being the monthly boil-off mass more for this case, the mass penalty introduced by the shield is outweighed more rapidly than in the case without the shield.

In conclusion, it can be said that, for both architectures, the VCS option always results the one with the lowest boil-off rates, but not always the most mass efficient, which depends on the required storage duration. When comparing the two propellant depot cases, it is possible to notice that in order to achieve the minimum insulation plus boil-off mass, a depot placed in LEO would require more insulation layers and therefore heavier designs. However, by employing the VCS system, the differences in boil-off rates from the GEO case start reducing.

6.4. Multi-tank model: eight tank configuration

This section is dedicated to the analysis of two locations of the hydrogen tank in the multi-tank configuration: the side and back tank. The propellant depot setup is shown in Figure 6.12, where the terms back and front have been selected based on the tank position in the depot with respect to the Sun.
It is noted that, in this configuration, the front tank is used for the storage of the liquid oxygen. In fact, for the chosen attitude, the front tanks are the ones most exposed to the solar radiation and do not benefit from any shading effect from the other tanks. Therefore, they are used for the storage of the cryogen with less strict temperature requirements, which is oxygen in the hydrolox mixture (90 K vs 20 K). For this reason, the thermal analysis on the front tank is not included hereby, where hydrogen only is studied.

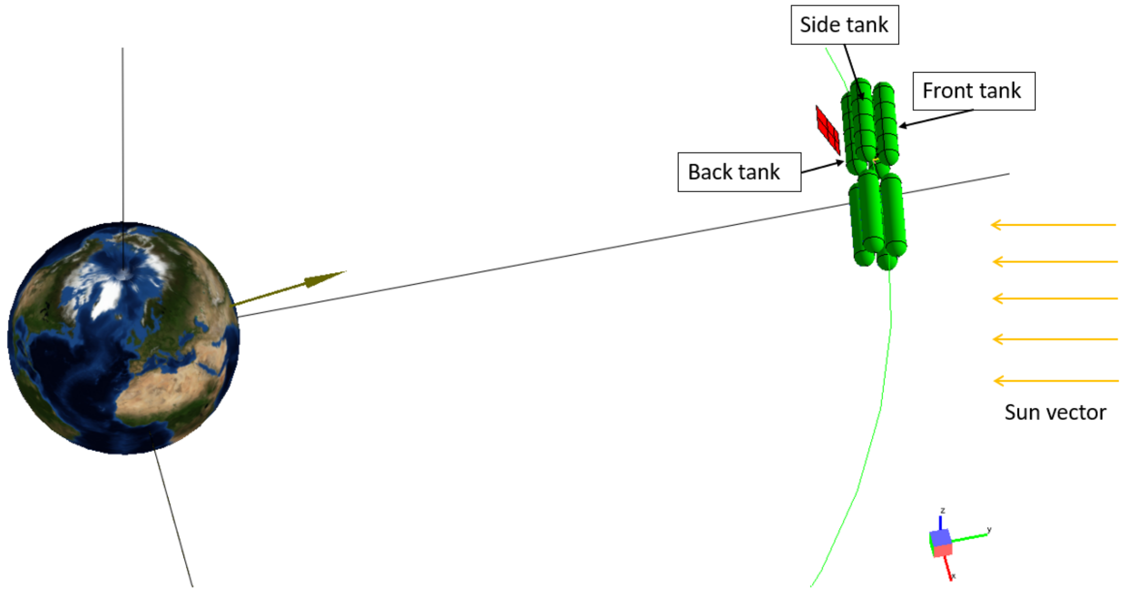

(a) Top view.

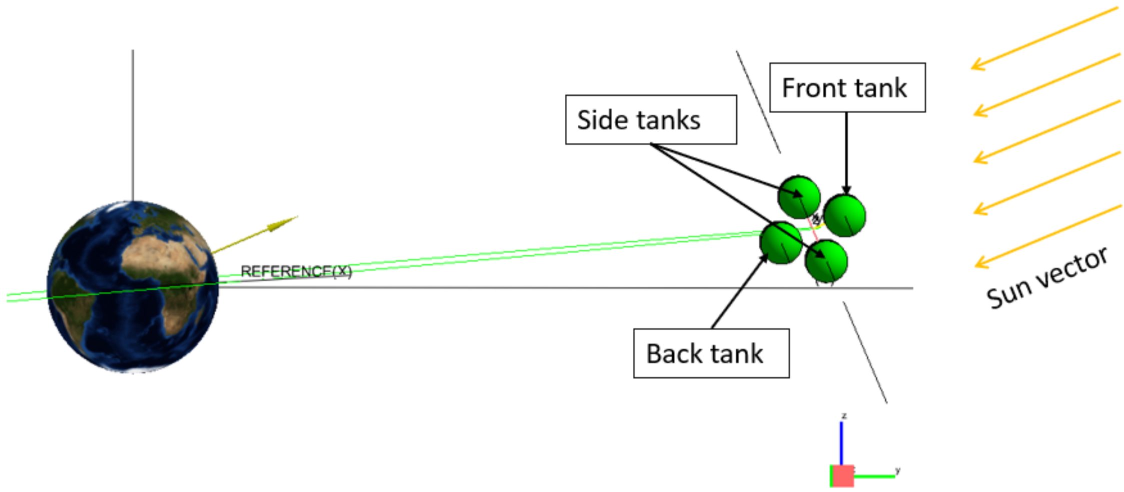

(b) Side view.

Figure 6.12: Eight tank model setup. Orbit is indicated in green.

To compare the single and multi-tank models, the same tank dimensions and propellant capacity as before are used. Each tank of the eight tank depot has the same geometry as the single tank model (see section 5.4), thus the inputs in Table 6.1 are still valid for this case.
The only difference comes from the thermal environment definition, which in the multi-tank case also

includes the effect of reflected heat from the other tanks of the depot. Moreover, each tank of the multi-tank depot is subjected to different heat loads depending on its position with respect to the Sun. For example, the tank in the back does not receive direct sunlight, but only reflections.

The GEO case is selected for the multi-tank analysis, while the same data relative to the LEO case can be found in Appendix A.3. In particular, only the VDMLI and VCS design options are analysed as they have been previously proven to be more mass efficient than the UDMLI in any case. The results of the analysis are shown in the plots in Figure 6.13, where the best VDMLI and VCS designs for the GEO case (Table 6.7) are applied to the side and back tank of the multi-tank depot and compared to the single tank depot.

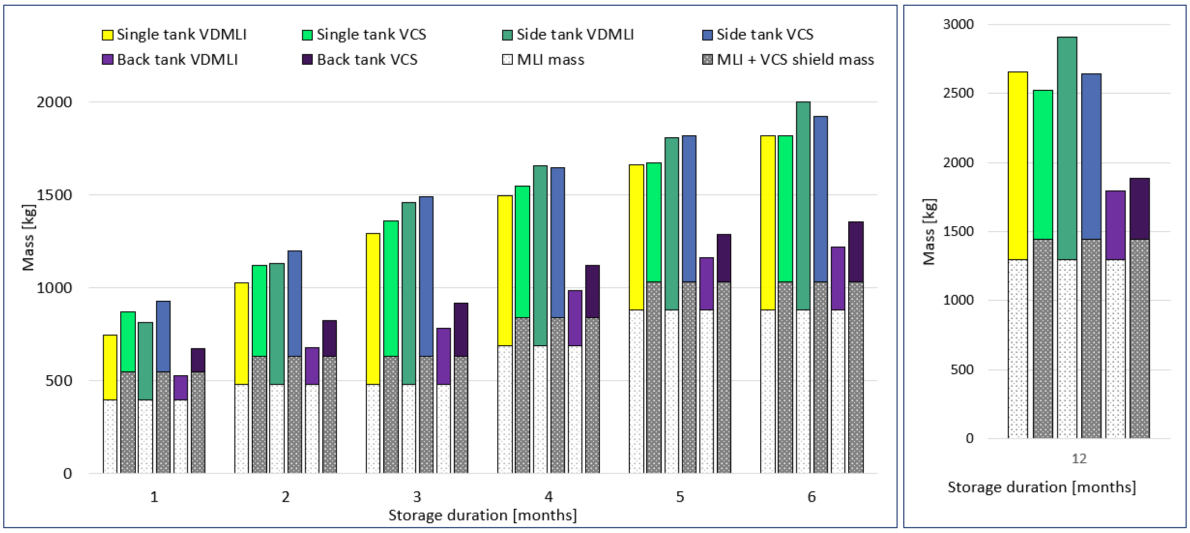

Figure 6.13: Single and multi-tank depot comparison, insulation and boil-off mass for different storage durations.

Figure 6.13 shows the insulation and boil-off mass for each design and for storage durations from 1 to 6 months, and 1 Earth year. Each bar in the graph indicates the combination of boil-off and insulation mass for one design option. In particular, the white and grey bars correspond to the MLI mass respectively without and with the addition of the VCS shield, while the colored bars are for the boil-off mass. It is noticed that for all the storage durations analysed, the best thermal performance, and therefore the lowest system mass is achieved by the hydrogen tank at the back of the multi-tank compound. On the other hand, the side tank case has slightly higher mass values than the isolated tank, which is expected because of the effect of reflections.

Figure 6.13 also shows that the VCS improves the VDMLI performance only for storage durations longer than 6 months for the single and side tank cases, while up to 1 Earth year of storage it is always not convenient to use a vapor shield for the back tank. This effect can be explained by the fact that, being the back tank very well shielded from the direct Sun rays, the boil-off mass takes more time to balance the mass penalty introduced by the shield. This is also confirmed by the bars of the boil-off mass being the shortest for the back tank.

Taking everything into account, it can be said that in an eight tank depot storing liquid hydrogen in GEO, it is more convenient to install a vapor shield only on the side and frontal tanks, leaving the back ones with VDMLI only.

A summary of the best design options for the back and side tanks of the multi-tank depot is shown in Table 6.11.

Table 6.11: Most mass efficient designs for storage of 34.6 mT of LH2, multi-tank GEO depot.

storage duration [months]		1	2	3	4	5	6	12
Best VDMLI designs: Back Tank								
	Tot # MLI	20	20	20	25	25	25	45
BO + MLI mass [kg]	VDMLI	530	655	780	885	975	1070	1550
	VDMLI + VCS	675	800	915	1015	1110	1200	1665
Best VDMLI designs: Side Tank								
	Tot # MLI	25	25	35	45	45	45	65
BO + MLI mass [kg]	VDMLI	810	1135	1415	1620	1810	2000	2910
	VDMLI + VCS	925	1200	1460	1625	1770	1925	2645

6.5. Final remarks

The analysis performed in this work is solely focusing on the thermal performance of the studied architectures. In order to extend the analysis to a broader systems study, some points of reasoning should be brought to the reader's attention.

It is shown that generally GEO depots are more convenient than LEO in terms of heat fluxes and resulting boil-off rates, however more Δv efforts are required to reach these orbits compared to LEO: inserting a payload into LEO requires about 9.3 km/s, which increases up to 11.7 km/s for GEO.
Therefore, for a GEO mission the payload at launch needs to be reduced because of the bigger amount of propellant needed to reach this orbit. Placing the depot in L1 reduces the required Δv with respect to GEO, however the depot would still need to be transported beyond LEO. On the other hand, by staying in LEO, more boil-off occurs due to the increased heat loads intensity.

This analysis has also proven that using multi-tank depots may not always be convenient in terms of heat loads. For this reason, the choice between single and multi-tank depot configurations should again depend on the requirement that stem from the mission, and whether multiple refuelings or a multi-mission support are desired.

One last note is on the depot attitude. The station could in fact be placed in orbit in such a way that minimizes the tank surface directly facing the Sun, limiting the boil-off and thus requiring less insulation mass. One example is placing the depot with its longitudinal axis always parallel to the Earth-Sun line. Another option could be to either reduce or remove the insulation from the sides of the depot that are always in the shadow. Alternatively, a lighter insulation structure could be coupled with a spinning depot to equally distribute the heat loads on its surfaces.
In any case, all the above mentioned options would require a dedicated Attitude Determination and Control System (ADCS), which adds its own mass and complexity to the depot design, and thus should be accounted for in the analysis.

In any case, it is clear that a deeper system analysis is needed to assess which architecture is more convenient depending on the mission objectives. On this regard, recommendations on how to proceed are given in chapter 7.

7 Conclusions and Recommendations

This chapter is dedicated to the conclusions of the thesis work presented in this report. In particular, the research questions formulated in the research plan are answered. Finally, recommendations for future research are given.

7.1. Conclusions

A versatile propellant depot sizing tool has been developed. This, called the Boil-off tool, performs a multi-nodal thermal analysis of a cryogenic tank for different thermal control design options, thermal environments, and depot geometries for varying mission duration. The thermal environment definition is done using ESATAN-TMS and given as input to the tool, allowing flexibility in the depot design, and orbit and attitude selection.
As for the thermal control options, the tool includes passive means such as uniform and variable density MLI, along with active means such as vapor cooled shields.
The main outputs of the Boil-off tool are the propellant boil-off rate, and the combined insulation and boil-off mass for a wide range of storage durations. If desired, heat loads and temperatures are also among the available outputs.

The Boil-off tool has then been applied to a single tank depot model to assess its thermal performance in two different locations, namely Geostationary and Low Earth orbit, with the possibility to use the GEO results also for a L1 depot. It has been shown that using variable density MLI improves the effectiveness of the thermal insulation: the most mass efficient designs in term of insulation and boil-off mass are achieved with less total number of layers when VDMLI is used.
The use of Vapour Cooled Shields additionally reduces the propellant boil-off of the cryogenic tank. However, this system starts to be beneficial in terms of mass savings only after 6 (for GEO depots) and 2 (for LEO depots) months of storage. This is due to the mass penalty introduced by the metal shield into the system.

Moreover, in case of a eight-tank depot, the boil-off mass depends on the the position of the tank in the station. For example, placing the tank in the shadow of the others, therefore away from direct sunlight, helps to reduce the propellant boil-off rates. On the other hand, the other tank positions are subjected to increased heat loads as a result of reflections that would worsen the boil-off with respect to the case of a single tank depot.
Furthermore, it has been shown that the most mass efficient configuration for a GEO eight tank depot is achieved using VDMLI for all tanks up to 6 months of storage, after which the use of VCS is recommended. This does however not apply to the tanks shaded from the sunlight, for which the VCS design is still heavier than VDMLI after 1 year of storage.

The final comparison has identified the single tank GEO depot as the most convenient in terms of total system mass. However, it has to be noted that conclusions drawn here are very case-specific, and therefore only applicable to the depot designs considered in this work.
Moreover, the analysis done here is only focusing on the performance of the thermal insulation. Therefore, it is not possible to state at this stage which depot location would be the most advantageous when considering other factors like cost, life, or risk. It should be also noted that the farther the depot is

placed, the more resources are needed to deliver all the necessary components for its assembly in orbit.
The Boil-off tool, and the performance evaluation done in this work can be used as starting point for a broader depot system analysis that considers all the above-mentioned factors, applying them to a wider range of realistic case studies to determine the most feasible concept.

7.1.1. Answers to research questions

It is now possible to go back to the research questions that were formulated in section 1.3, and to give proper answers based on the results of this thesis work. It should be noted that all the results mentioned hereby refer to the in-orbit cryogenic storage of liquid hydrogen.

The main research question for this project is the following:

Can successful strategies for applying active and passive cooling methods for in-orbit cryogenic storage be identified in terms of total system mass with focus on a chosen mission?

The analysis performed in this work has focused on the use of passive thermal control techniques, in particular Multi-Layer Insulation (MLI) with a uniform and variable density distribution of the reflector layers. On the active thermal control part, the use of a metal shield cooled down by the hydrogen boil-off vapors as means to improve the thermal performance has been studied.

The main objective of the study is to identify thermal design combinations that are most mass efficient for specific case studies defined in section 5.4. In particular, single and multi-tank depots in GEO and LEO are studied.
The parameter used for the comparison is the combination of insulation and boil-off mass, which are varying based on the chosen thermal control solution. Therefore, the most mass efficient design is defined as the one that returns the lowest value of this mass combination.

Results have shown that using variable density MLI improves the effectiveness of a thermal insulation: the most mass efficient designs in term of insulation and boil-off mass is achieved with less total number of layers when VDMLI is used, thus reducing the total insulation mass needed. Moreover, the use of Vapour Cooled Shields additionally reduces the boil-off into the cryogenic tank. However, this system introduces a mass penalty due to the presence of the metal shield, therefore the use of VCS starts to be advantageous only for missions which require long storage times (in the order of months). The exact number depends on the orbit the depot is placed into.

In order to give a proper answer to the main question, the following sub-questions have been formulated and answered to throughout the thesis project.

1. **Can a computational tool be developed such that it allows for analysing a space mission and selecting the best design option based on total system mass minimization?**
   The Boil-off tool is a propellant depot sizing model that allows to determine the effect of different thermal control design options, thermal environments, attitudes and depot configurations for varying mission duration.
   The original version of the Boil-off tool, developed by [24], has been extended in this work in order to include new design options, such as variable density MLI, vapor cooled shields, and autogenous pressurization. Furthermore, a new nodal structure and external thermal environment definition has been added. In particular, the latter has been done with the support of the ESATAN-TMS software. A summary of all the Boil-off tool extensions made in this work can be found in Table 2.1.

2. **Can the importance of depot configuration and location be identified for attaining the lowest mass for a cryogenic propellant depot for a specific mission?**
   The effect of the depot configuration on the total system mass has been studied by comparing a single tank and a multi-tank depot. All the considered tanks were alike in shape and geometry, but located in different positions with respect to the Sun based on the depot configuration.

   Results showed that it would be preferable to have a tank shielded from direct sunlight as it indeed returns the lowest insulation and boil-off mass combination. However, it has also been noticed that each tank of a multi-tank depot experiences higher boil-off rates, up to 70 % increase than if they were isolated. This is because of the reflected heat coming from the other components of the depot, which is completely rejected into space only in case of a single tank depot.

The depot location in space is important for any depot design as it affects the thermal environment definition, and the thermal control system. For example, it has been shown in this work how depots in LEO always require more more MLI layers than GEO to achieve the lowest boil-off and insulation mass combination, therefore resulting in heavier designs. The depot location also influences the effectiveness of the VCS, as it is investigated by the following question.

3. **Can boil-off venting solutions lead to a system mass reduction for orbital propellant depots?**
Vapor Cooled Shields are considered boil-off venting solutions as they make use of the vented vapors from the ullage to cool down the cryogenic tank.
Results have shown that systems equipped with vapor shields always return the lowest boil-off mass compared to the other design options. However, using VCS starts to be advantageous only when the mass penalty introduced by the metal shield is outweighed by the boil-off mass in case no VCS is used. This means that the VCS is beneficial only if the cryogen needs to be held in orbit for some time before being used. This time depends on the depot location in space: for LEO orbits, VCS returns the lowest system mass for storage times from 2 months on, while for a depot placed in GEO this time goes up to a minimum of 6 months. More in general, the more severe the incoming heat loads on a depot are, the more the use of VCS is beneficial in terms of total system mass.

4. **What are suitable mission architectures for this study and why?**
The cis-lunar space is identified as the main area of operations for orbital propellant depots so far. Within this area, Low Earth and Geostationary orbits are currently the main area of interest of all satellite and spacecraft operations. In addition, the Earth-Moon Lagrange points are also considered as suitable propellant depot locations because of their easier access to the Solar System and the cold thermal environment they provide.
Furthermore, literature has shown that many orbital propellant depots stations exist, for example formed by a single tank, or a group of them. The latter is the case where a single station would be able to support multiple missions without the need of refuelling in between.

   Therefore, the mission architectures analysed in this work have been generated by combining the main orbits of the cis-lunar environment with different propellant depot configurations already proposed in literature.

5. **What is the influence of the thermal environment on the results?**
The analysis performed here has focused on two main cis-lunar propellant depot locations: Geostationary and Low Earth orbits. A characteristic of these two orbits is that they have a very different thermal environment: a spacecraft placed in GEO receives almost constant solar fluxes throughout the orbit, with seasonal eclipses that do not last more than one hour each. On the other hand, LEO orbits are characterized by eclipses with durations depending on the relative position of the spacecraft, the Earth and the Sun. Furthermore, due to the proximity of LEO to the Earth's surface (less than 2000 km), albedo and planetary fluxes have a non-negligible influence on the heat received by the spacecraft.

   Albedo and planetary fluxes depend on the orbit distance from the Earth's surface, therefore they are never exactly zero for the orbits of the cis-lunar space. However, it has been proven that for a GEO depot, they add up to less than 2% of the total fluxes incoming on the tank body.
The weaker influence of albedo and planetary fluxes allowed to identify here the same thermal environment for the GEO and L1 depot case: a comparison of the solar fluxes generated by ESATAN-TMS for the same depot geometry for these two orbits has shown almost a complete agreement. This means that the GEO depot thermal performance analysis done here is still valid and applicable to the L1 depot case, which may be also the preferable location between the two as it can be reached with a smaller Δv.

6. **Does the outcome of the study change between missions with different architectures and durations?**

All the studied architectures agree on the fact that the design experiencing the lowest monthly boil-off rates is the Vapor Cooled Shield. However, in case the system mass is a concern, orbits characterized by more intense heat fluxes immediately benefit from the use of a VCS (this happened for LEO), while for ”colder” orbits, a VCS may not be the best design option if the storage time is short (GEO requires 6 months).
Moreover, also the depot configuration influences the effectiveness of the VCS. In fact, in the multi-tank analysis, it is shown that within the same depot, tanks shielded from the direct solar fluxes do not need a VCS to achieve the optimum mass performance. On the other hand, tanks directly facing the Sun would indeed gain benefits from the use of vapor shields. Again is confirmed the dependence of this effect on the storage duration.

7.2. Recommendations

As it is always the case for research topics as broad as the one of in-orbit cryogenic storage, the work presented in this thesis does not have to be seen as a finish line, but rather a starting point and an added value to anyone that decides to approach the field of cryogenics. Therefore, some ideas for future work and applications of the Boil-off tool are given in this final section. These are grouped in sections based on their area of interest.

7.2.1. Thermal environment model in ESATAN-TMS

- Include the effect of seasonal variations in the incoming fluxes. This can be done by exporting different ESATAN-TMS heat fluxes profiles for different positions of the Earth in its orbit around the Sun.

- Include the shielding effect of other components of the depot station: solar panels, tank forward and aft skirt, Sun-shield. This requires the mentioned elements to be modeled with the depot geometry in ESATAN-TMS.

- To the scope of this work, ESATAN-TMS has only been used for the radiative analysis of the different orbits. However, many more features of this software could be used in advantage of this work. For example, with a proper training and deeper knowledge of the software, the ESATAN-TMS thermal analysis could be used to validate the results obtained from the Boil-off tool.
  In fact, the software is able to compute any spacecraft's surface temperature, as long as a proper thermal model is built. This would require more details than the ones used for the radiative analysis, such as inclusion of conductive couplings, surface materials, any internal heat sources, and boundary conditions. Once a model that satisfies all the requirements above has been built and the temperature calculations performed, this could be compared to the one obtained with the Boil-off tool.

7.2.2. Boil-off tool

- The Boil-off tool thermal network has been re-defined to allow for a multi-nodal analysis of the tank. In particular, the tank nodes are now divided into two groups, them corresponding to the left and right side of the tank. Future work could be focused on further improving the variability of the number of nodes and decoupling them from any tank sub-division.

- One issue identified in this work is the huge simulation time required by the Boil-off tool, which has limited the number of options and mission durations studied. One recommendation would be then to improve the tool's computational speed so to increase the number of design options that can be simulated at the same time: the Boil-off tool has been written in Cython and therefore all the processes are run in series. However, it would be ideal to run in parallel some of the processes in the code in order to speed-up the simulations.

7.2.3. General recommendations

- This analysis focused on the estimation of the total heat leak into the cryogenic tank in order to evaluate the monthly boil-off rate. For this reason, the number of nodes in the thermal network has been chosen accordingly. However, this number has not been proven to be the optimal one and further studies could be focused on this matter.

For example, in case of a study that focuses on the temperature distribution along the tank body, it is recommended to identify a higher number of nodes for the liquid and ullage sections.

- The Boil-off tool is able to analyse the thermal performance of a cryogenic tank with the propellant in settled conditions. A future step would then be to analyse and model the processes in the tank under micro-gravity conditions.
- This work has been focusing on depot attitudes that would represent the worst case scenario for the tanks in terms of thermal fluxes. Future work could focus on analysing the same radiative case for different depot attitudes, finding an optimum in terms not only of heat fluxes, but also the least demanding in terms of Attitude Control System (more ideas are given in section 6.5).
- Include the architecture studies performed here into a broader mission analysis with a defined objective in order to identify the best orbital propellant depot solution. On this regard, parameters such as payload to be moved, final destination of spacecraft, and propellant capability on depot should be considered.
- Extend the analysis to different propellant mixtures, for example methalox.

References

[1] George P Sutton and Oscar Biblarz. *Rocket propulsion elements*. John Wiley & Sons, 2016.

[2] Jeffrey De Kruif. “Centaur Upperstage Applicability for Multi-Day Mission Durations with Minor Insulations Modifications”. In: *43rd AIAA/ASME/SAE/ASEE Joint Propulsion Conference & Exhibit*. 2007, p. 5845.

[3] John Gaebler et al. “Reusable Lunar Transportation Architecture Utilizing Orbital Propellant Depots”. In: *AIAA SPACE 2009 Conference & Exposition*. 2009. DOI: `10.2514/6.2009-6711`. URL: `https://arc.aiaa.org/doi/abs/10.2514/6.2009-6711`.

[4] Thomas M Tomsik. *Recent advances and applications in cryogenic propellant densification technology*. American Institute of Chemical Engineers, 2000.

[5] Benton-C Clark. “H/O as the Key to Survival for Humans in Deep Space”. In: *SAE Transactions* (1988), pp. 430–433.

[6] Bernard Kutter et al. “Atlas centaur extensibility to long-duration in-space applications”. In: *Space 2005*. 2005, p. 6738.

[7] S. O’Dell et al. “Crewed missions to the martian surface via mars base camp”. In: 2018.

[8] B Zandbergen. “Ae1222-II: Aerospace design and systems engineering elements I. Part: Launch Vehicle design and sizing”. In: *Delft University of Technology* (2019).

[9] CB Muratov, Viatcheslav V Osipov, and Vadim N Smelyanskiy. *Issues of long-term cryogenic propellant storage in microgravity*. National Aeronautics and Space Administration, NASA Ames Research Center, 2011.

[10] Elon Musk. “Making humans a multi-planetary species”. In: *New Space* 5.2 (2017), pp. 46–61.

[11] Patrick R. Chai and Alan W. Wilhite. “Cryogenic thermal system analysis for orbital propellant depot”. In: *Acta Astronautica* 102 (2014), pp. 35–46. ISSN: 0094-5765.

[12] Alan Wilhite et al. “Evolved Human Space Exploration Architecture Using Commercial Launch/Propellant Depots”. In: *63rd International Astronautical Congress, Naples, Italy*. 2012.

[13] L Morgan. “Orbital tanker designs and operational modes for orbit launch programs”. In: *2nd Annual Meeting*. 1965, p. 383.

[14] David Street and Alan Wilhite. “A scalable orbital propellant depot design”. In: *Masters Project, Department of Aerospace Engineering, Georgia Institute of Technology, Atlanta, GA* (2006).

[15] Bernard Kutter et al. “A practical, affordable cryogenic propellant depot based on ULA’s flight experience”. In: *AIAA Space 2008 Conference & Exposition*. 2008, p. 7644.

[16] Frank Zegler and Bernard Kutter. “Evolving to a depot-based space transportation architecture”. In: *AIAA Space 2010 Conference & Exposition*. 2010, p. 8638.

[17] David Gilmore. *Spacecraft Thermal Control Handbook, Volume I: Fundamental Technologies*. 2002.

[18] Eric Hurlbert, Michael Baine, and Gene Grush. “An open exploration architecture using an L-1 space propellant depot”. In: *SpaceOps 2010 Conference Delivering on the Dream Hosted by NASA Marshall Space Flight Center and Organized by AIAA*. 2010, p. 2158.

[19] Leon J Hastings et al. “An overview of NASA efforts on zero boiloff storage of cryogenic propellants”. In: *Cryogenics* 41.11-12 (2001), pp. 833–839.

[20] PM Sutheesh and Alex Chollackal. “Thermal performance of multilayer insulation: a review”. In: *IOP Conference Series: Materials Science and Engineering*. Vol. 396. 1. IOP Publishing. 2018, p. 012061.

[21] Peter Kittel. “Cryocooler performance estimator”. In: International Cryocooler Conference. 2007.

[22] WB Jiang et al. “Coupling optimization of composite insulation and vapor-cooled shield for on-orbit cryogenic storage tank”. In: *Cryogenics* 96 (2018), pp. 90–98.

[23] Wenbing Jiang et al. “Thermal analysis of coupled vapor-cooling-shield insulation for liquid hydrogen-oxygen pair storage”. In: *International Journal of Hydrogen Energy* 47.12 (2022), pp. 8000–8014.

[24] Mitchell Borst. *Mass optimisation of cryogenic fluid systems for long-duration space missions*. TU Delft repository, 2020.

[25] C Fröhlich and RW Brusa. “Solar radiation and its variation in time”. In: *Solar Physics* 74.1 (1981), pp. 209–215.

[26] BJ Anderson, CG Justus, and GW Batts. “Guidelines for the selection of near-earth thermal environment parameters for spacecraft design”. In: *NASA Technical Memorandum* 211221 (2001).

[27] Peter Fortescue, Graham Swinerd, and John Stark. *Spacecraft systems engineering*. John Wiley & Sons, 2011.

[28] B Zandbergen. “Ae1222-II: Aerospace design and systems engineering elements I”. In: *Delft University of Technology* (2017).

[29] ITP Engines UK Ltd. *ESATAN-TMS Workbench User Manual*. 2017.

[30] Yunus A Çengel. *Introduction to thermodynamics and heat transfer: Engineering*. 2008.

[31] B Wang et al. “Optimization of variable density multilayer insulation for cryogenic application and experimental validation”. In: *Cryogenics* 80 (2016), pp. 154–163.

[32] MM Finckenor and D Dooling. *Multilayer insulation material guidelines*. Tech. rep. 1999.

[33] ConceptGroup and InsulonTechnology. *Vacuum Super Insulation with High Temperature MLI*. 2019. (accessed: 11.08.2022).

[34] Glen E McIntosh. “Layer by layer MLI calculation using a separated mode equation”. In: *Advances in cryogenic engineering*. Springer, 1994, pp. 1683–1690.

[35] CW Keller, GR Cunnington, and AP Glassford. *Thermal performance of multilayer insulations*. Tech. rep. 1974.

[36] LJ Hastings, A Hedayat, and TM Brown. *Analytical modeling and test correlation of variable density multilayer insulation for cryogenic storage*. Tech. rep. 2004.

[37] Leon J Hastings and James J Martin. “Experimental testing of a foam/multilayer insulation (FMLI) thermal control system (TCS) for use on a cryogenic upper stage”. In: *AIP Conference Proceedings*. Vol. 420. 1. American Institute of Physics. 1998, pp. 331–341.

[38] A Hedayat, LJ Hastings, and T Brown. “Analytical modeling of variable density multilayer insulation for cryogenic storage”. In: *AIP Conference Proceedings*. Vol. 613. 1. American Institute of Physics. 2002, pp. 1557–1564.

[39] Jianpeng Zheng et al. “Experimental study on composite insulation system of spray on foam insulation and variable density multilayer insulation”. In: *Applied Thermal Engineering* 130 (2018), pp. 161–168.

[40] JE Fesmire et al. “Spray-on foam insulations for launch vehicle cryogenic tanks”. In: *Cryogenics* 52.4-6 (2012), pp. 251–261.

[41] D. Plachta et al. “NASA cryocooler technology developments and goals to achieve zero boil-off and to liquefy cryogenic propellants for space exploration”. In: *Cryogenics* 94 (2018), pp. 95–102. ISSN: 0011-2275.

[42] Christopher McLean et al. “Simple, robust cryogenic propellant depot for near term applications”. In: *2011 Aerospace Conference*. IEEE. 2011, pp. 1–24.

[43] C Christian, E Lehmann, and L Ruby. “Autogenous pressurization for space vehicle propulsion systems”. In: *4th Propulsion Joint Specialist Conference*. 1968, p. 626.

[44] William Notardonato. “Active control of cryogenic propellants in space”. In: *Cryogenics* 52.4-6 (2012), pp. 236–242.

[45] LG Bolshinskiy et al. *Tank system integrated model: a cryogenic tank performance prediction program*. Tech. rep. 2017.

[46] Ian H Bell et al. “Pure and pseudo-pure fluid thermophysical property evaluation and the open-source thermophysical property library CoolProp”. In: *Industrial & engineering chemistry research* 53.6 (2014), pp. 2498–2508.

[47] EW Lemmon et al. “NIST Standard Reference Database 23: Reference Fluid Thermodynamic and Transport Properties-REFPROP, Version 10.0, National Institute of Standards and Technology”. In: *Standard Reference Data Program, Gaithersburg* (2018).

[48] LJ Hastings et al. *Spray bar zero-gravity vent system for on-orbit liquid hydrogen storage*. Tech. rep. 2003.

[49] Cornelius E Klots. “Evaporative cooling”. In: *The Journal of chemical physics* 83.11 (1985), pp. 5854–5860.

[50] Russell B Scott. “Thermal design of large storage vessels for liquid hydrogen and helium”. In: *Journal of Research of the National Bureau of Standards* 58.6 (1957), p. 317.

[51] WB Jiang et al. “Experimental investigation on combination of vapor cooled shield (VCS) and multilayer insulation (MLI) for cryogenic application”. In: *IOP Conference Series: Materials Science and Engineering*. Vol. 755. 1. IOP Publishing. 2020, p. 012153.

[52] Jim Le Bar and Ed Cady. “The advanced cryogenic evolved stage (ACES)-a low-cost, low-risk approach to space exploration launch”. In: *Space 2006*. 2006, p. 7454.

[53] Jonathan Goff et al. “Realistic near-term propellant depots: implementation of a critical spacefaring capability”. In: *AIAA Space 2009 Conference & Exposition*. 2009, p. 6756.

[54] Alok Majumdar et al. “Numerical modeling of self-pressurization and pressure control by a thermodynamic vent system in a cryogenic tank”. In: *Cryogenics* 74 (2016), pp. 113–122.

[55] Peter J Linstrom and William G Mallard. “The NIST Chemistry WebBook: A chemical data resource on the internet”. In: *Journal of Chemical & Engineering Data* 46.5 (2001), pp. 1059–1063.

[56] Stefan Behnel et al. “Cython: The best of both worlds”. In: *Computing in Science & Engineering* 13.2 (2010), pp. 31–39.

[57] Cython. *Welcome to Cython’s Documentation*. 2021. URL: `https://cython.readthedocs.io/en/latest/`.

[58] Daniel Moser. “Prospects for composite LOX tankage”. In: *29th Joint Propulsion Conference and Exhibit*. 1993, p. 2249.

[59] Kaushik Mallick et al. “Ultralight linerless composite tanks for in-space applications”. In: *Space 2004 Conference and Exhibit*. 2004, p. 5801.

[60] Fardin Ghaffari-Tabrizi, Jan Haemisch, and Daniela Lindner. “Reducing Hydrogen Boil-Off Losses during Fuelling by Pre-Cooling Cryogenic Tank”. In: *Hydrogen* 3.2 (2022), pp. 255–269.

[61] JJ Martin and L Hastings. *Large-scale liquid hydrogen testing of variable density multilayer insulation with a foam substrate*. Tech. rep. 2001.

[62] Steven Simske. “Chapter 5 - Sensitivity analysis and big system engineering”. In: *Meta-Analytics*. Ed. by Steven Simske. Morgan Kaufmann, 2019, pp. 187–201. ISBN: 978-0-12-814623-1.

[63] Yinan Qiu et al. “Research progress of cryogenic materials for storage and transportation of liquid hydrogen”. In: *Metals* 11.7 (2021), p. 1101.

[64] Thomas M Perrin and James G Casler. “Architecture Study for a Fuel Depot Supplied From Lunar Resources”. In: *AIAA SPACE 2016*. 2016, p. 5306.

[65] Paul D Spudis. *Develop Cislunar Space Next*. 2012.

[66] Richard Oeftering. “A cis-lunar propellant infrastructure for flexible path exploration and space commerce”. In: *AIAA SPACE 2011 Conference & Exposition*. 2011, p. 7113.

[67] Frank Zegler, Bernard Kutter, and Jon Barr. “A commercially based Lunar architecture”. In: *AIAA SPACE 2009 Conference & Exposition*. 2009, p. 6567.

[68] Howard Curtis. *Orbital mechanics for engineering students*. Butterworth-Heinemann, 2013.

[69] NASA. *Moon Fact Sheet*. 2021. URL: `https://nssdc.gsfc.nasa.gov/planetary/factsheet/moonfact.html`. (accessed: 27.05.2022).

[70] WL Johnson. “Optimization of layer densities for multilayered insulation systems”. In: *AIP Conference Proceedings*. Vol. 1218. 1. American Institute of Physics. 2010, pp. 804–811.

[71] Patrick R Chai. “Stochastic feasibility assessments of orbital propellant depot and commercial launch enabled space exploration architectures”. PhD thesis. Georgia Institute of Technology, 2014.

A

Additional information

A.1. Forward Euler method

For a pure-time differential equation in the form:

$$\begin{aligned} \frac{\mathrm{d}y}{\mathrm{d}t} &= f(t) \\ y\,(t_0) &= y_0 \end{aligned} \tag{A.1}$$

The forward Euler method uses a time step size Δt which defines a grid of t values ($t_{i+1} = t_i + \Delta t$) and approximates the solution y through:

$$y_{n+1} = y_n + \Delta t f\,(t_n, y_n) = y_{i-1} + \Delta t \lambda y_{i-1} = y_{i-1}(1 + \lambda \Delta t) \tag{A.2}$$

Being it an explicit method, forward Euler allows to find the solution straightforward. However, attention should be paid to not fall outside the stability region of this method. According to [1], for stability the step size Δt should be such that:

$$\Delta t \leq \frac{2}{|\lambda|} \tag{A.3}$$

A.2. Thermal network with tank wall node

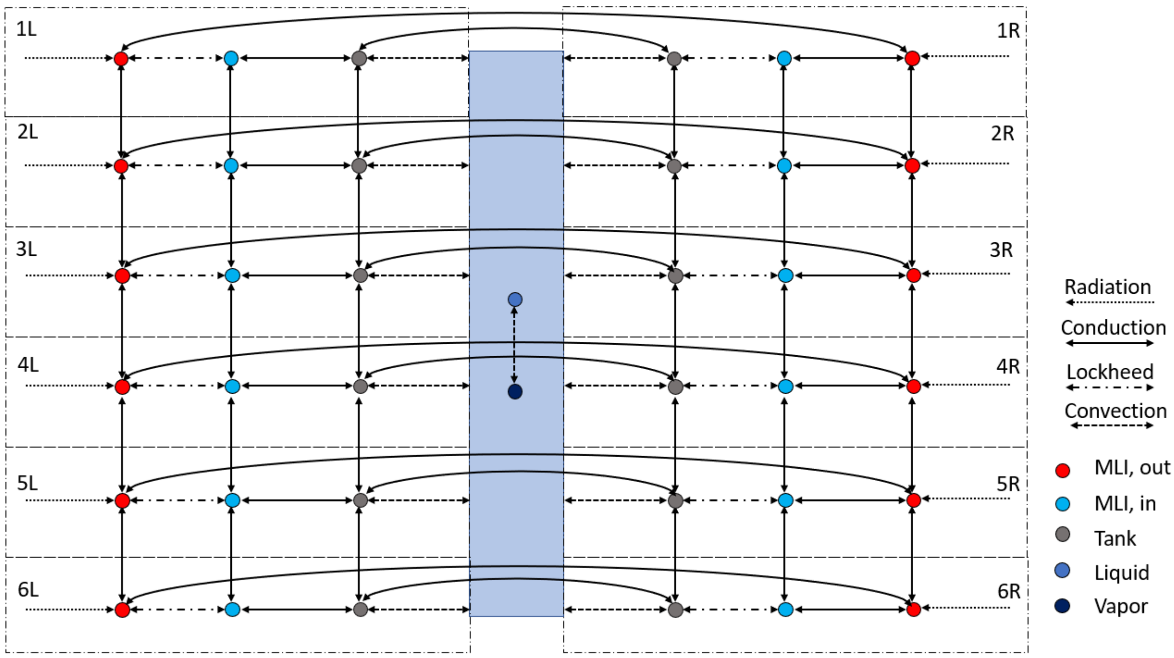

Figure A.1: Tank thermal network including tank wall node.

A.3. Multi-tank model: LEO Case

The same multi-tank depot analysis performed in section 6.4 is done here for the LEO case. Again, only the VDMLI and VCS options have been studied. The results are shown in Figure A.2, where the best VDMLI and VCS design options are applied to the side and back tank of the multi-tank depot and compared to the single tank depot.

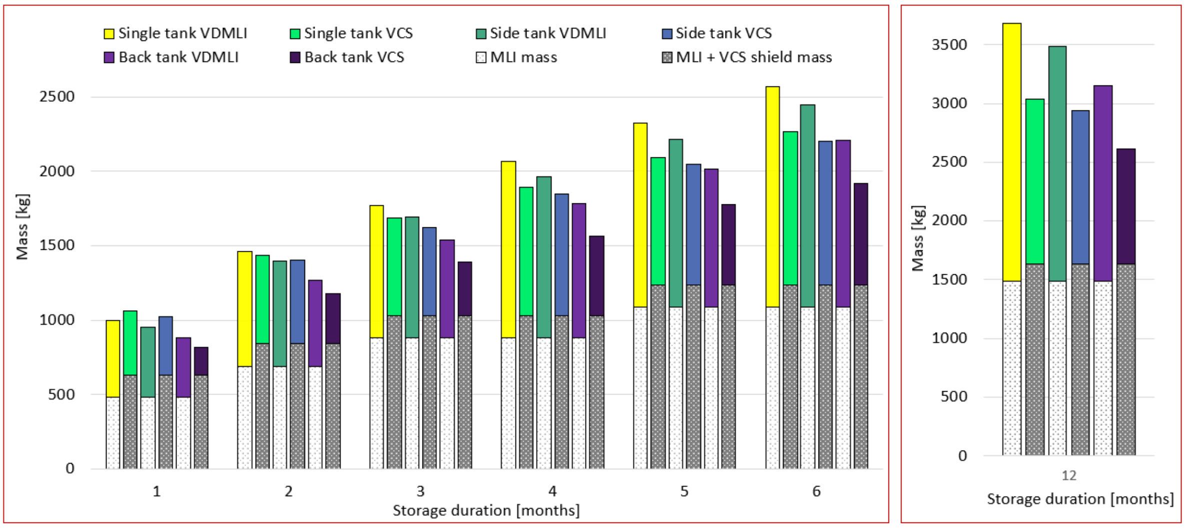

Figure A.2: Single and multi-tank depot comparison, insulation and boil-off mass for different storage times, LEO.

The first detail that is noticed from Figure A.2 is that placing the hydrogen tank in the back of the depot does not bring the same mass savings as the GEO case. In particular, the difference in total mass of the back tank case with respect to the side and single tank is greatly reduced. This effect is expected because, while the back tank is shielded by the other tanks from the direct sunlight, nothing

can be done for the albedo and planetary radiation, which are incident on every surface of the depot facing the Earth.
Furthermore, for the LEO case, placing the tank on the back or side of the eight tank depot results in a more mass efficient design than the single tank depot. This is explained by the presence of albedo and planetary radiation, which intensity for the single tank depot exceeds the quantity of heat absorbed by the tanks of the eight tank depot as a consequence of reflections.
Lastly, while the use of VCS on the side tank of the eight tank depot brings mass benefits only after 2 months of storage, the vapor shield is always recommended for the back tank.

A summary of the best design options for the back and side tanks of the multi-tank depot is shown Table A.1.

Table A.1: Most mass efficient designs for storage of 34.6 mT of LH2, multi-tank LEO depot.

Storage time [months]		1	2	3	4	5	6	12
Best VDMLI designs Tank back								
BO + MLI mass [kg]	Tot # MLI	25	35	45	45	55	55	75
	VDMLI	880	1270	1540	1780	2015	2210	3155
	VDMLI + VCS	815	1180	1390	1565	1775	1920	2615
Best VDMLI designs Tank side								
BO + MLI mass [kg]	Tot # MLI	25	35	45	45	55	55	75
	VDMLI	955	1395	1695	1965	2215	2445	3490
	VDMLI + VCS	1025	1405	1625	1845	2045	2205	2940

B
Boil-off tool guidelines

In this appendix, some important guidelines on the use of the Boil-off tool are given, together with a detailed description of its program files.
The Boil-off tool is open-source, and it is available upon request to the author or to the Delft University of Technology.

B.1. The Boil-off tool package

The Boil-off tool is written using the Cython 3.0.0a11 and Python 3.9.4 versions. In particular, the tool consists of several Python and Cython files that all contribute to building and analysing the propellant tank thermal model. The Boil-off tool package must contain the following files to properly work:

- *'Import_from_ESATAN.py'*
- *'New_code.pyx'*
- *'setup.py'*
- *'Boiloff_Monte_Carlo_program_and_parameters.py'*

The function of each of the Boil-off tool package files is explained in the following sections.
In addition, the following Python packages must also be installed:

- pandas
- tqdm
- numpy
- pathlib
- cython
- matplotlib
- CoolProp

B.2. Guidelines to run the program

In this section, the function of each file part of the Boil-off tool package is explained. Furthermore, instructions on how to run the code, the inputs to be given to the tool, and the outputs format are also given.
The files introduced in the following section are also in their execution order in the Boil-off tool.

B.2.1. Import thermal environment data in Python

File:'Import_from_ESATAN.py' Output: 'Radiative_model.npz'
This Pyhton program takes as input the "Radiative results" report file from ESATAN-TMS. The file extension is *.rpt, and needs to be converted in a *.txt format.
Some changes are needed before giving this file as input to the Boil-off tool: first of all, every data that does not directly concern the fluxes on the nodes need to be removed from the file: this includes the radiative model information at the beginning of the file, and fluxes information about total model and inactive faces at the end of the file.
The *'Import_from_ESATAN.py'* file can then be executed in Python, and it fills in a fluxes matrix according to the procedure already explained in subsection 3.1.2, and shown again here with Figure B.1 for completeness.

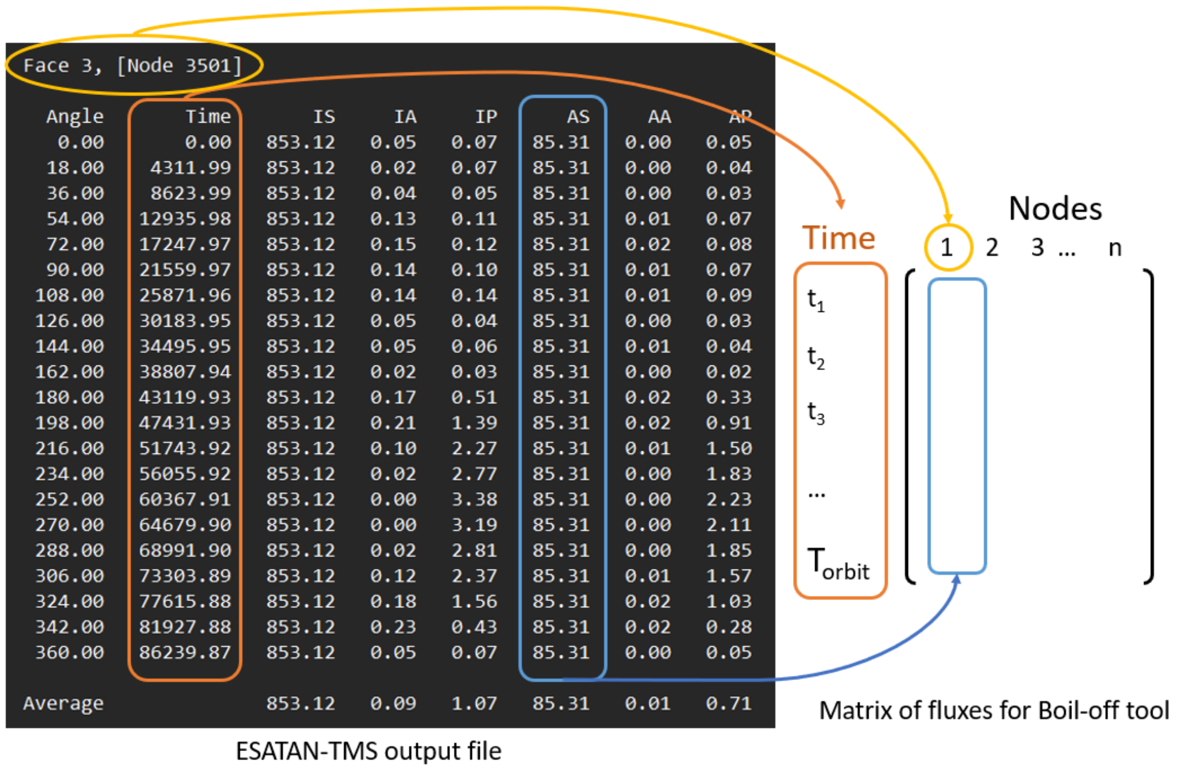

Angle	Time	IS	IA	IP	AS	AA	AP
0.00	0.00	853.12	0.05	0.07	85.31	0.00	0.05
18.00	4311.99	853.12	0.02	0.07	85.31	0.00	0.04
36.00	8623.99	853.12	0.04	0.05	85.31	0.00	0.03
54.00	12935.98	853.12	0.13	0.11	85.31	0.01	0.07
72.00	17247.97	853.12	0.15	0.12	85.31	0.02	0.08
90.00	21559.97	853.12	0.14	0.10	85.31	0.01	0.07
108.00	25871.96	853.12	0.14	0.14	85.31	0.01	0.09
126.00	30183.95	853.12	0.05	0.04	85.31	0.00	0.03
144.00	34495.95	853.12	0.05	0.06	85.31	0.01	0.04
162.00	38807.94	853.12	0.02	0.03	85.31	0.00	0.02
180.00	43119.93	853.12	0.17	0.51	85.31	0.02	0.33
198.00	47431.93	853.12	0.21	1.39	85.31	0.02	0.91
216.00	51743.92	853.12	0.10	2.27	85.31	0.01	1.50
234.00	56055.92	853.12	0.02	2.77	85.31	0.00	1.83
252.00	60367.91	853.12	0.00	3.38	85.31	0.00	2.23
270.00	64679.90	853.12	0.00	3.19	85.31	0.00	2.11
288.00	68991.90	853.12	0.02	2.81	85.31	0.00	1.85
306.00	73303.89	853.12	0.12	2.37	85.31	0.01	1.57
324.00	77615.88	853.12	0.18	1.56	85.31	0.02	1.03
342.00	81927.88	853.12	0.23	0.43	85.31	0.02	0.28
360.00	86239.87	853.12	0.05	0.07	85.31	0.00	0.05
Average		853.12	0.09	1.07	85.31	0.01	0.71

Figure B.1: Python-based ESATAN conversion: fluxes matrix generation. Optical properties used (MLI): $\alpha = 0.10, \varepsilon_{IR} = 0.66$.

In particular, all the heat fluxes will be saved in a total of two matrices: one for the right and the other for the left side of the tank, as shown in Figure B.2.

It has to be noted that the fluxes matrix generation process is dependant on the number of nodes chosen and on how the tank model has been generated in ESATAN-TMS. Therefore, it is up to the user to make sure that the fluxes are acquired correctly in the matrix.
The code developed here is a first draft made only to the scope of acquiring the thermal fluxes to continue with the analysis. Improving the flexibility of this code is indeed a recommendation for future work.

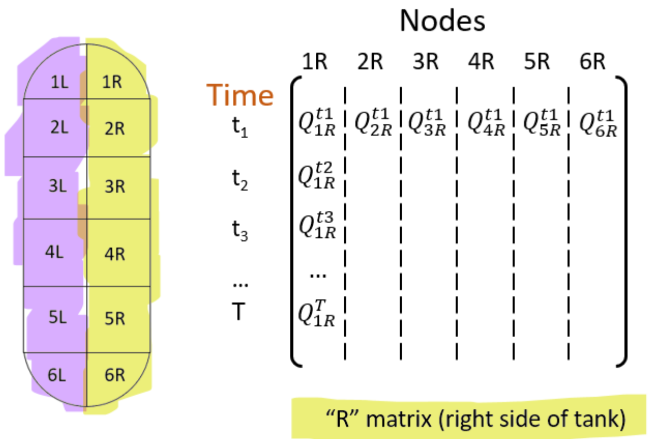

Figure B.2: Matrices of fluxes for right (R) and left (L) side of the tank, generated using ESATAN-TMS data.

B.2.2. *Cythonize* the Boil-off program

The Boil-off tool main body can be found in the **'New_code.pyx'** file, and it is written in Cython . There are little to no differences with the Python language (more details can be found in the Cython documentation [2]).
To execute the Boil-off tool using Cython, the code needs to be first compiled in C (this process is also called "Cythonizing" the code). More details about how to compile Cython programs can be found in [2], however one method would be to execute the following line in the terminal:

python setup.py build_ext –inplace

This requires an additional Python file called *'setup.py'* which is provided with the Boil-off tool package. A message notifies the user when the compilation is complete, generating two additional files with extensions *.c and *.so.

It is important to always make sure that the latest version of the *'New_code.pyx'* file is being used. If changes are made to the code, saving these changes does not mean that they are automatically compiled. Therefore, it is advised to always Cythonize the code before running it.

B.2.3. Run the Boil-off program

File: 'Boiloff_Monte_Carlo_program_and_parameters.py' Output: npz files and csv files
This is a Python file where all the Boil-off tool inputs are set, and it is executed in Python once the *'New_code.pyx'* has been compiled in C. The complete list of inputs of the boil-off tool can be found hereby:

- Simulation time step
- Storage duration (in months)
- Number of MLI layers
- MLI layer density
- Type of ESATAN-TMS fluxes: absorbed or direct
- VDMLI: ON or OFF
- VDMLI number of sectors
- VCS activity: ON or OFF
- VCS location: middle or inner VDMLI sector
- Insulation structure: MLI only, or MLI and WALL

- Pressurization: autogenous or heterogeneous
- Propellant mass
- Initial temperature and pressure
- Maximum tank pressure
- Tank radius (set this to 0 for spherical tank)
- Tank initial fill level
- Tank wall material (C_p, k, density, thickness)
- Reflector layer specific weight and nominal thickness
- Spacer layer specific weight and nominal thickness
- MLI thermal parameters (C_p, k)
- MLI inner and outer emissivity, and MLI solar absorptivity
- Gravity
- Space temperature ($\approx 3K$)
- Propellant mixture (LH2, LCH4 and LOX possible)
- Tank number of nodes
- Tank end-cap height (spherical or ellipsoidal shape)
- VCS tube diameter and length
- VCS shield material (density, C_p)
- VCS shield thickness
- Time-step for VCS analysis
- Desired pressure after venting
- Save data vectors over time: YES or NO

The Boil-off tool outputs are the following:

- Design options parameters, mass of the systems, and boil-off rate and mass are stored in *.csv files based on the selected mission duration
- Final temperature and heat loads are stored in *.npz files and can only be opened using Python

Once a single simulation is done, the outputs need to be stored on different directories before running the tool again: every new run, any existing data is automatically overwritten.

C
IAC22 conference paper

IAC-22,D1,2,x73094

Architecture study for in-orbit long term cryogenic storage to support space exploration

Ludovica Formisani [a]*, Barry Zandbergen [a]

[a] *Department of Space Systems Engineering, Delft University of Technology (TU Delft), The Netherlands,* ludovica.formisani@gmail.com, B.T.C.Zandbergen@tudelft.nl
* Corresponding Author

Abstract

The space community is currently focusing on defining mission architectures able to perform multiple interplanetary missions to support deep space exploration. In particular, placing orbital propellant depots in strategic locations in space would allow to increase the useful mass transferred.

The design of the propellant depot depends greatly on the propellant storage duration and the thermal environment the depot experiences. Furthermore, different cryogenic propellant combinations are being considered for use, including hydrolox and methalox. For both, efficient boil-off reduction strategies are fundamental. The aim of this work is to evaluate different depot architectures for different thermal environments and mission durations.

The approach taken in this work included the development of a propellant depot sizing model that allows determining the effect of different thermal control design options, thermal environments, and depot configurations for varying mission duration. The design options include, amongst others, Multi-Layer Insulation and Vapor Cooled Shields. The model also allows for a multi-nodal thermal analysis to estimate boil-off rates for the different designs. Main objective for the studies is to identify the architecture that is most mass efficient.

Preliminary results show that mass efficient designs can be achieved with only passive insulation for mission durations below one year, with further improvements when adding a vapor cooled shield to the design.

Keywords: cryogenics, propellant depot, vapor cooled shields, thermal control system, mission architecture, liquid hydrogen storage

Nomenclature

α	absorptivity
ε	MLI inner emissivity
ε_{IR}	MLI IR outer emissivity
ρ	Mass density
σ	Stefan-Boltzmann constant
dT	Temperature variation
dt	Time-step
Δv	Velocity change
$\dot{m}$	Mass flow rate
$\bar{N}$	MLI density distribution
$P^*(x,T)$	MLI interstitial pressure
$\bar{T}$	Average temperature
A	Area
a, b, c	Lockheed model constants
C_p	Specific heat capacity
d	Diameter
h	Convective heat transfer coefficient
k	Conductivity
L	Latent heat
M	Mass
m, n	Lockheed model constant exponents
N	MLI layers number
Nu	Nusselt number
Pr	Prandtl number
Q	Heat load
Re	Reynolds number
T	Temperature
t	Thickness

Subscripts

abs	absorbed
C	cold boundary
cont	contact
diss	dissipated
emit	emitted
F	fluid
H	hot boundary
in	input
liq	liquid
mid	middle
net	net, remaining
out	output
r	reflector layer
S1, S2, S3	VDMLI inner, middle, outer sector
S,tot	total MLI sectors

s	spacer
shield	VCS metal shield
tank	tank
tot	total
vap	vapor
vent	venting

Acronyms/Abbreviations

BO	Boil-off
ESATAN-TMS	ESATAN Thermal Modelling Suite
GEO	Geostationary Orbit
IR	Infra-red
LEO	Low Earth Orbit
LH2	Liquid Hydrogen
LOX	Liquid Oxygen
MLI	Multi-Layer Insulation
UDMLI	Uniform-Density MLI
VCS	Vapor Cooled Shields
VDMLI	Variable-Density MLI
ZBO	Zero Boil-off
#MLI	Number of MLI layers

1. Introduction

The current trend in space exploration is to develop advanced systems able to transport humans to the far edges of the Solar System.
One of the options considered for future space exploration is in-orbit (re)fuelling of spacecrafts from orbital propellant depots. Orbital propellant depots would in fact allow to allocate more vehicle launch mass to payload, while propellant is launched on less expensive (because uncrewed) launch vehicles. Among the considered options to make such systems in a mass efficient way is the use of cryogenic propulsion, like hydrolox or methalox, thanks to the very high specific impulse that can be achieved [1].
A major drawback of these propellants that could jeopardize all the mass savings though is boil-off. This is unused propellant which comes from cryogen evaporation due to heat penetration in the tank structure. For current systems, this boil-off is about 2% per day of the initial stored propellant mass [2]. Such a high boil-off rate can easily nullify the benefits of using cryogenic propellants.

The birth of the concept of orbital propellant depots goes back to 1965 [3], when early orbital tanker designs started to be proposed to the scientific community. Ever since, this concept has drawn increasing attention.
In 2006, [4] developed a scalable depot sizing tool and applied it to a Low Earth Orbit (LEO) case study. However, several other locations have been proposed, like for example the Earth-Moon Lagrange points, or even an orbit about the Moon or Mars.
The first propellant depot concepts were based on adapting existing launchers and upper stages for long-term orbital storage ([5], [6]). This was done to minimize risks and uncertainties. According to [5], the depot is assembled on Earth and launched empty to eliminate the need of foam insulation, thereby allowing for a mass reduction. In fact, foam is only properly working in atmospheric environments as its task is to reduce the convective heat transfer [7].
Another depot concept has been proposed by [8] and [9]. This consists in pre-positioning a depot in orbit to support multiple missions. The depot is formed by one or multiple tanks, and it is assembled in orbit; standardized interfaces allow compatibility with multiple launch suppliers. This solution would decouple the depot itself, which would not depend on the needs and timelines of a specific mission anymore.
[10] have proven that propellant depots are fundamental for the space exploration evolution, as they improve the extensibility and mission payload capability.

In any case, in-orbit refueling would require orbital propellant depots that are able to store cryogenics for long durations while in orbit: for these systems, boil-off reduction becomes fundamental.
Boil-off reduction can be achieved with both passive and/or active means. Passive thermal control systems involve no mechanical moving parts or fluids, and there is no power consumption, thus ensuring lower mass and cost [11]. Among these, Multi-Layer Insulation (MLI) [12] is the most used technology, and it consists in foils coated with a highly reflective metal and with low thermal conductive spacers placed in between so that they are not in direct contact. On the other hand, active thermal control systems make use of moving fluids, mechanisms, or power to transfer heat. Among these, it is worth to mention cryogenic coolers (also called cryocoolers or cryogenic refrigerators) [13]. Cryocoolers are particularly suitable to achieve zero Boil-off (ZBO) designs [11].

[14] proposed a performance study of a cryogenic orbital depot employing both passive and active systems. In particular, the analysis focused on combinations of MLI and cryocoolers for LEO storage of liquid hydrogen (LH2) and oxygen (LOX). Results showed that the ZBO option is only achievable with the employment of cryocoolers; however, the current state-of-the-art of in-space cryocoolers does not include systems powerful enough to achieve ZBO for the hydrogen tank.
Among the potential candidates identified for cryogenic storage performance improvement, vapor cooled shields (VCS) were of interest to this work. This technique consists in using the boil-off vapors from the ullage to cool down the tank walls before being vented overboard.

Studies on VCS systems have been performed by [15] and [16], and they have both shown that the use of these systems reduces the heat leak into the tank.

To our knowledge, no system study assessing the effectiveness of employing VCS on orbital propellant depots currently exists. Furthermore, only few studies assess the performance of multiple combinations of thermal design options for long-term storage. In most publications of thermal depot studies, tools are used but they are not publicly available.
The objective of this study is to develop a propellant depot sizing tool which is then used to perform a comparison between two different case studies. The analysis focuses on passive thermal control systems, with the option of including VCS. Main object of interest is the thermal performance of the depot, as it is the driving factor in most studies.

In this paper, the methodology and theory behind the propellant depot sizing model is first described (sections 2 and 3). Then, in section 4, results relative to two case studies are presented and analysed, along with the main conclusions (section 5).

2. Methodology

The approach taken in this work consisted in the development of a propellant depot sizing model (the "Boil-off tool") that allows determining the effect of different thermal control design options, thermal environments, and depot configurations for varying mission duration. This has been done by creating a model that considers different passive thermal control methods, namely uniform and variable density MLI (UDMLI and VDMLI respectively), and vapor cooled shields. Moreover, the tool also supports the addition of active cryocoolers to the design, however these systems have not been included in the current analysis.
The model allows to estimate boil-off rates for the different design options, together with the associated system mass.

The Boil-off tool performs a multi-nodal thermal analysis of the propellant tank, with the number of nodes and the thermal insulation structure that can be user-defined. In particular, the model consists in a time-step analysis that iteratively solves the heat balance for each node of the network, computing at each step their temperature and the heat leak into the stored cryogen. The latter is then used to compute the propellant boil-off mass. The analysis stops when the desired storage duration is reached, which could go from a couple of days up to years. A detailed block diagram representing the Boil-off tool code structure is given in Appendix A.

The cryogen is stored in the tank by simply keeping the liquid and ullage in equilibrium at their saturation temperature and pressure. This technique is also called autogenous pressurization, meaning that there is no other gas in the ullage than the cryogen vapor phase. However, this also means that any heat leak into the tank would result in the boil-off of the fluid.
The more the fluid evaporates, the more the tank pressure increases; when the pressure design limit is reached, a venting process is activated to ensure that the pressure is kept under control. However, this also means that the boil-off vapors vented overboard are permanently lost. The cryogenic fluid boil-off is computed using the total heat leak into the bulk liquid Q_{liq} and the latent heat of vaporization L_{vap} at the cryogen saturation condition:

$$\dot{m}_{boiloff} = \frac{Q_{liq}}{L_{vap}} \tag{1}$$

For example, the saturation temperature of liquid hydrogen stored at 1 bar is 20.4 K, corresponding to a latent heat of vaporization of 452 kJ/kg.

When setting up a tool for the thermal performance simulation of an orbital depot, there are two main aspects that must be considered: the external thermal environment definition, which is responsible of the hot temperature on the outer surface of the spacecraft, and the tank sizing and thermal model.
For this work, the ESATAN Thermal Modelling Suite (ESATAN-TMS) is used to model the thermal environment, while the sizing and thermal performance estimation are done by a custom-developed tool.

3. Theoretical model

In this section, the theory behind the Boil-off tool is described. More details about the thermal environment definition are also given.

3.1 *Thermal environment model*

ESATAN-TMS is a general-purpose thermal-radiative software tool, and it is one of the standards used within the space industry.
This program allows the user to create a thermal model, by defining materials, geometry, optical properties of the finishes used, boundary conditions, and many other parameters needed to perform the thermal analysis.
Once the geometry of the model is defined, the ESATAN-TMS radiative analysis is able to compute all the external heat fluxes coming to the spacecraft during a specific mission, based on its attitude and the Sun/planet environment.

An example of depot geometries that can be designed using ESATAN-TMS is given in Figure 1.

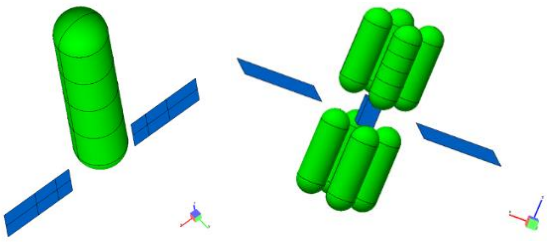

(a) Single tank depot. (b) Multi-tank depot [8].

Figure 1. Different depot geometries modelled using ESATAN-TMS.

The output given by the program is in the form of a file containing all the incident and absorbed fluxes on each tank section defined by the user, for a specified number of positions in the defined orbit.
For this reason, a Python-based program has been developed to convert the output data given by ESATAN-TMS into compatible inputs for the boil-off model, providing an external tank environment definition which is node and time dependant.

The absorbed fluxes given by ESATAN-TMS are then converted into their respective heat loads. This is done by the Boil-off tool, which calculates the absorbing surface area of each tank section and multiplies it by the heat fluxes provided in the thermal environment model. Afterwards, the following heat balance is performed [7]:

$$\begin{gathered} Q_{\text{in}} = Q_{\text{out}} \\ Q_{\text{abs}} + P_{\text{diss}} = Q_{\text{emit}} \end{gathered} \tag{2}$$

Assuming that there is no internal power generation ($P_{\text{diss}} = 0$), combining the balance in (2) with the thermal radiation equation (3) allows to compute the temperature of the MLI outer side (also called hot temperature T_H).

$$\mathrm{Q}_{\text{emit}} = \varepsilon_{IR} \sigma A_{emit} {T_H}^4 \tag{3}$$

3.2 Tank sizing and thermal analysis model

Boil-off management is one, if not the main, point of attention for long-term storage of cryogenics in orbit: a correct estimation of the boil-off losses is fundamental for the success of a mission, as well as to developing a design that is efficient and with the least mass demand. The propellant depot sizing model presented here is written in Cython and performs a multi-nodal thermal analysis of a propellant tank system, allowing to determine the effect of different thermal control design options, thermal environments, and depot configurations for varying mission duration.

The main parameters object of the analysis are the propellant boil-off in the tank over time and the thermal control system mass.
In this section, more details about the modelling of the single objects involved in the thermal analysis are given. Attention is focused on passive means, namely uniform and variable density MLI, and vapor cooled shields.

3.2.1 Multi-layer insulation

An empirical relation to estimate the thermal performance of MLI without performing a layer-by-layer analytical analysis (as proposed by [17]) is the Lockheed model, which has been developed by [18].
In this model three heat transfer mechanisms are considered, namely solid conduction, gas conduction, and radiation between reflective shields. Among the three effects, radiation has been proven to be the most critical in space, where vacuum conditions almost eliminate the gas conduction effect. As for solid conduction, according to [17] this is due to the presence of materials to support and separate the reflector layers, therefore it can never be completely eliminated.
These three contributions are shown in equations (4), (5), and (6), and they refer to the thermal fluxes (W/m^2) through the MLI.

$$\mathrm{q}_{\text{solid conduction}} = \frac{a(\bar{N})^{\mathrm{n}} \mathrm{T_m} (\mathrm{T_H} - \mathrm{T_C})}{N} \tag{4}$$

$$\mathrm{q}_{\text{radiation}} = \frac{b\varepsilon\sigma(\mathrm{T_H^{4.67}} - \mathrm{T_C^{4.67}})}{N} \tag{5}$$

$$\mathrm{q}_{\text{gas conduction}} = \frac{c\mathrm{P}^*(\mathrm{x,T})\left(\mathrm{T_H^{(m+1)}} - \mathrm{T_C^{(m+1)}}\right)}{N} \tag{6}$$

$$\mathrm{q}_{\text{tot, MLI}} = \mathrm{q}_{\text{solid conduction}} + \mathrm{q}_{\text{radiation}} + \mathrm{q}_{\text{gas conduction}} \tag{7}$$

This model allows to compute the total heat leak through the MLI (7) by solving for the hot ($\mathrm{T_H}$) and cold ($\mathrm{T_C}$) temperatures. The other parameters in the equations are derived from the specific insulation system and interstitial gas used; for example, in case of perforated aluminized shields and Dacron net spacers, [19] proposed the Modified Lockheed Model.
Many authors in literature, like [19] and [14] have proven that there is a good agreement in terms of estimated heat leak between the traditional layer-by-layer and the Lockheed model.

The Lockheed equation can be used to calculate the heat leak through the MLI both in case of uniform and variable layer density. In the second case, each MLI segment characterized by the same density requires a separate Lockheed equation to be solved. A schematic of the thermal model used for the variable-density MLI case is shown in Figure 2.

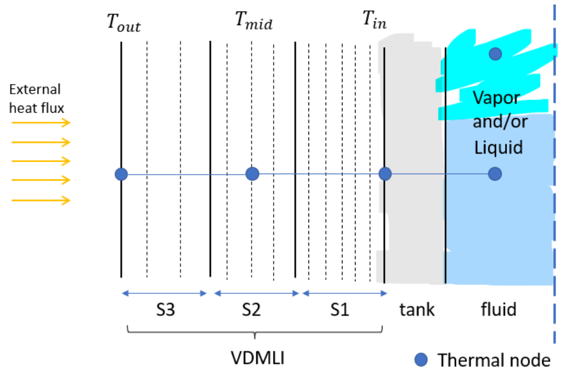

Figure 2. Variable-Density MLI thermal model structure (blue circles correspond to thermal nodes).

According to [20], the main function of Variable-Density MLI is to provide more layers in the warmer (outer) regions of the insulation blanket, and fewer layers in the colder (inner) regions where blocking radiation becomes less important. When using VDMLI, the number of possible combinations of number of layers and layer densities becomes high. [21] presented and validated through experiments a practical method to optimize any VDMLI configuration. Results showed that the best thermal performance in terms of lowest heat leak would be given by a density of the middle (S2) and inner (S1) MLI sector which is respectively 2/3 and 1/3 of the outer one (S3).
For the present work, a system of equations is used to compute the number of reflector layers for each VDMLI sector. This is done by starting from equation (8), which defines the total thickness of the VDMLI based on the number of layers per sector and their respective density:

$$t_{VDMLI} = \frac{N_{s3}}{100\bar{N}_{s3}} + \frac{N_{s2}}{100\bar{N}_{s2}} + \frac{N_{s1}}{100\bar{N}_{s1}} \qquad (8)$$

By manipulating the equation above and assuming that all the VDMLI sectors have the same thickness ([16], [22]), the system in (9) can be written:

$$\begin{cases} N_{s3} = \dfrac{N_{s,tot}/100\bar{N}_{s1}}{\dfrac{1}{100\bar{N}_{s3}} + \dfrac{1}{100\bar{N}_{s1}} + \dfrac{\bar{N}_{s2}}{100\bar{N}_{s3}\bar{N}_{s1}}} \\ N_{s2} = \dfrac{\bar{N}_{s2}}{\bar{N}_{s3}} N_{s3} \\ N_{s1} = N_{s,\text{tot}} - N_{s3} - N_{s2} \end{cases} \qquad (9)$$

With this algorithm it is thus possible to calculate the number of layers of each sector in a 3 segment VDMLI system, given the total number of layers and the layer density distribution.

Finally, both for the uniform and variable density MLI, the same mass estimation equation as [14] is used:

$$M_{\text{MLI}} = \left[\rho_r + \frac{\rho_s}{t_s}\left(\frac{1}{100\bar{N}} - t_r\right)\right] N A_{tank} \qquad (10)$$

Equation (10) has been obtained by directly looking at the structure of the MLI blanket; in particular, the relation shown above is applicable only when each sheet of separator material covers the same surface (A_{tank}) as each reflector layer.
In case other separation techniques are used, like for example bumper stripes [17], a different relation to estimate the mass contribution of the spacers should be applied.

3.2.2 Vapor Cooled Shield

The VCS is modelled as a highly conductive thermal shield with a spiral flow tube through which the venting gas flows [15]. One important assumption in the modelling of the VCS is the temperature uniformity of the shield.

A schematic of the VCS structure can be found in Figure 3, while a detailed nodal architecture and principal heat flows occurring are shown in Figure 4.

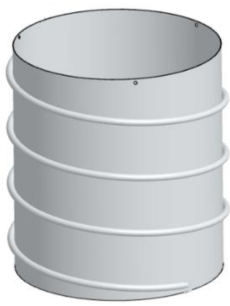

Figure 3. Schematic of vapor cooled shield [15].

According to [15], placing the shield between two MLI segments (with same or varying layer density) achieves the most efficient cooling performance of the VCS, thus the same configuration is chosen for this analysis.

In this work, the vapor cooled shield is modelled as a solid-vapor heat exchanger between the vented gas and the shield itself, that is the heat load subtracted from the VCS vapors is computed using the convective heat transfer correlations. After that, it is possible to use the net heat leak into the shield to compute its temperature, and the heat load absorbed by the fluid to find its outlet temperature at the end of the spiral path.

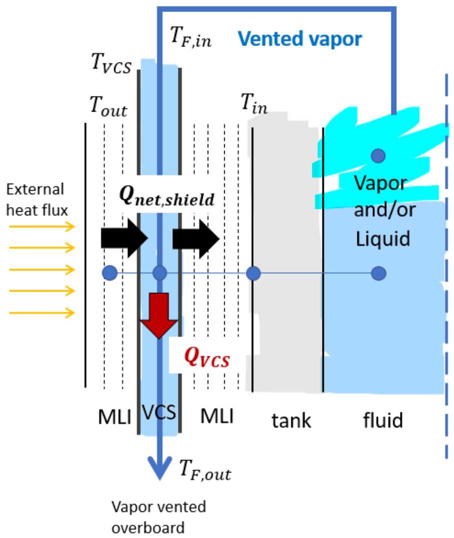

Figure 4. Vapor Cooled Shield system main parameters and heat balance.

The main equations used to model the heat exchange process in the VCS shield are:

$$Q_{VCS} = h_{VCS}A_{\text{cont}}\,(T_{VCS} - \overline{T_F}) \quad (11)$$

$$\frac{dT_{VCS}}{dt} = \frac{Q_{\text{net, shield}} - Q_{VCS}}{M_{\text{shield}}\,C_{p,\text{ shield}}} \quad (12)$$

$$T_{F,\text{ out}} = T_{F,\text{ in}} + \frac{Q_{VCS}}{\dot{m}_{vent}C_{p,vent}} \quad (13)$$

Where Q_{VCS} is the heat absorbed by the fluid in the VCS, while $Q_{\text{net, shield}}$ is the net heat load into the shield.

The shield mass M_{shield} is computed using the shield thickness and material properties, while A_{cont}, which refers to the available heat exchange area, is calculated using the VCS tube diameter (11.7 mm [16]) and total length. All the fluid properties that are pressure and temperature dependant are taken from the Coolprop open source thermophysical property library [23].

To properly model the heat exchange, an accurate estimation of the convective heat transfer coefficient h_{VCS} is needed. This is done using equation (14):

$$h_{VCS} = \frac{\text{Nu}_{vap}k_{vap}}{d_{VCS}} \quad (14)$$

Where the Nusselt number Nu_{vap} of the vented gas depends on the flow conditions in the tube and its Reynolds number [15]:

$For\ Re < 1960\ (laminar\ flow)$:

$$\text{Nu} = 3.66 \quad (15)$$

$For\ 1960 < Re < 6420\ (transitional\ flow)$:

$$\text{Nu} = 0.116\left(\text{Re}^{\frac{2}{3}} - 125.0\right)\text{Pr}^{0.4} \quad (16)$$

$For\ Re > 6420\ (turbulent\ flow)$:

$$\text{Nu} = 0.023\text{Re}^{0.8}\ \text{Pr}^{0.4} \quad (17)$$

4. Results and Discussion

In this section, the results of the analysis of two different depot scenarios are presented and discussed. In particular, the focus is on the storage of 34.6 mT of liquid hydrogen in orbit. This value is chosen by looking at similar cases studied in literature (in particular [14]), however the Boil-off tool allows to select any propellant capacity and tank dimensions that the user needs.

The depot structure consists of a single tank with spherical endcaps, with a radius of 2.7 m and a total height (including caps) of 25.4 m (shown in Figure 1a). The liquid hydrogen is stored at a pressure of 1.3 bar, and the ullage venting process is activated whenever the maximum allowed pressure (set at 3 bar) is reached.
The depot is covered with MLI and directly assembled in orbit, so no foam insulation is considered (see section 1). Boil-off reduction systems that can improve the performance of UDMLI, namely variable density MLI and vapor cooled shields are included in the analysis.
The main objective of the study is to identify thermal design options that are most mass efficient. The two parameters used for this analysis are the monthly boil-off rate, and the combined insulation and boil-off mass for different mission durations.
In particular, the boil-off and insulation mass are important as they define, together with the initial propellant and tank mass, the structural mass ratio of the depot station.

4.1 Thermal environment and depot attitude

The orbits chosen for the study are Geostationary (GEO) and Low Earth Orbit (LEO). The former has the advantage of less critical heat fluxes (only solar is relevant at that distance from the Earth), while the latter is preferable for its closeness to the Earth's surface and thus a better accessibility for any spacecraft launched from the Earth's surface.

For this study, the worst-case scenario in terms of heat fluxes incoming on the depot is selected, that is when one of the tank sides is continuously oriented towards the Sun. This attitude is graphically represented in Figure 5 using ESATAN-TMS. More details on the influence of the depot attitude on the incoming thermal heat loads can be found in Appendix B.

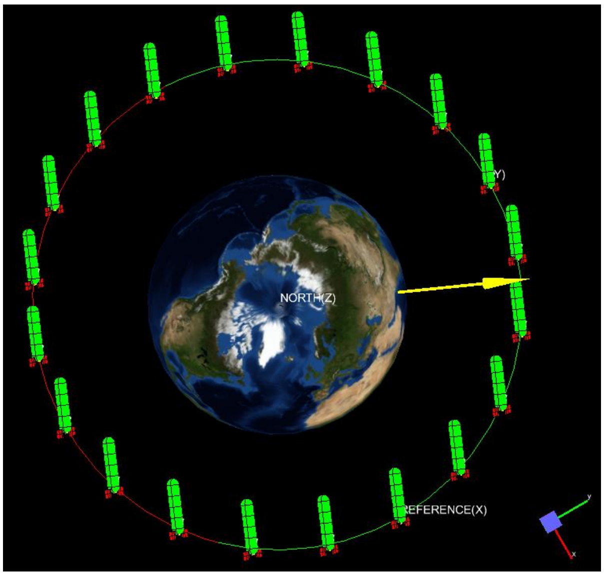

Figure 5. Single tank depot orientation along orbit, yellow arrow is pointing at the Sun.

A representation of the heat loads for both orbits can be found in Figure 6. The profiles are plotted for a total duration of 24 hours, which correspond to one orbit around Earth in GEO and about sixteen in LEO.

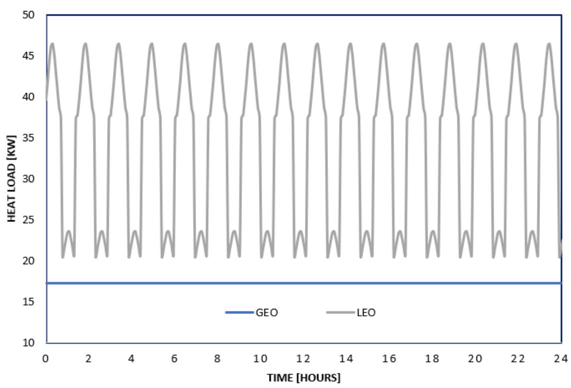

Figure 6. GEO and LEO absorbed heat load for single tank depot (MLI optical properties $\alpha = 0.10$, $\varepsilon_{IR} = 0.66$).

For the selected depot attitude, the GEO case is characterized by a constant heat load throughout the orbit, hence the "flat" line. In fact, for this case only the solar fluxes are considered, since planetary and albedo represent less than 2% the total incident heat [7]. The intensity of the solar fluxes depends in its turn on the planet-Sun distance, which of course stays constant throughout the orbit, and on the recurrent eclipses, which only happen seasonally for GEO.

The chosen LEO orbit is circular with a 400 km altitude and 5° inclination. For this case, not only solar but also albedo and planetary radiation contribute to the incident fluxes on the tank. Figure 6 also shows the effect of eclipses on the heat load.

4.2 GEO propellant depot

Figure 7 shows the percent of monthly boil-off (with respect to initial stored propellant mass) vs number of MLI layers, together with the total insulation and boil-off mass (shown in the colour bar) after 1 Earth year of storage in Geostationary orbit, for MLI layer densities of 16 and 40 layers/cm.

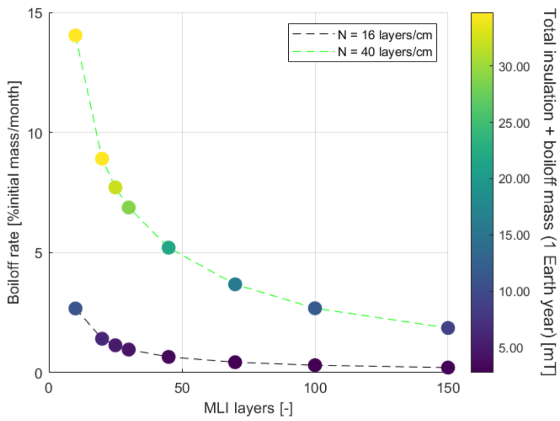

Figure 7. Monthly boil-off (wrt initial propellant mass) and insulation + boil-off mass (after 1 year) vs number of MLI layers for 34.6 mT of LH2 storage in GEO.

First, as expected, reducing the layer density results in lower boil-off rates for the liquid hydrogen. In fact, lower MLI densities mean that reflector layers are more distanced with one another, reducing conductive losses [14].

Furthermore, we see that the heaviest designs correspond to the ones with the least number of MLI layers. While having less MLI layers would be beneficial in terms of insulation mass, the same does not hold for the boil-off mass. In fact, less MLI layers would allow more external thermal radiation to penetrate the tank, thus increasing the heat leak and the boil-off. On the other hand, it would not be beneficial to use too many MLI layers, as this would result in a system with a huge insulation mass penalty. It is thus necessary to identify an optimal combination of number of MLI layers and boil-off that would return the lowest mass.

This mass comparison is given in Figure 8 for the 16 layers/cm density case, where the total insulation and

boil-off mass is plotted vs the number of MLI layers for different storage durations.
It is noticed that each curve has a minimum, corresponding to the most mass efficient design, and that this minimum slowly shifts to the right as the storage duration increases. The lowest mass designs for the UDMLI case correspond to a range of MLI layers that goes from 25 up to 65.

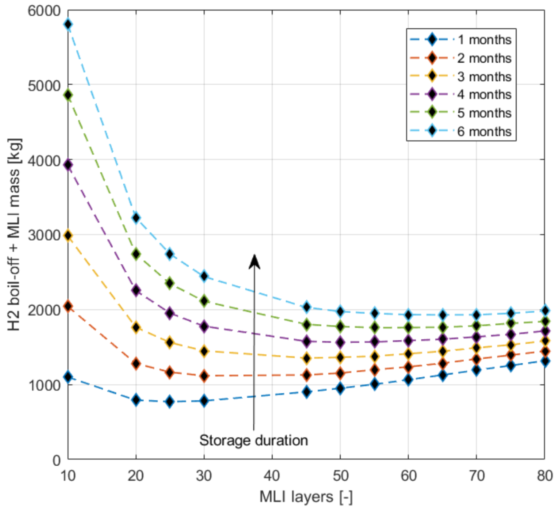

Figure 8. Boil-off + MLI mass vs number of MLI layers for storage durations from 1 to 6 months, UDMLI, 34.6 mT of LH2 storage in GEO.

In case of 1 Earth year of storage in GEO, it is noticed that the insulation and boil-off mass keep decreasing up to 100 MLI layers, to then increase again from 150 layers. The lowest mass is indeed achieved within this range of number of layers; however, this is not investigated further as this number is usually limited to 80 because of manufacturing difficulties. This has been confirmed by [14], according to whom there is no documented literature showing MLI blankets that employ more than 80 layers.

The same analysis can be done for the Variable Density MLI case by optimizing the MLI layers distribution according to the procedure explained in section 3.2.1. Results are shown in Figure 9. All the design options correspond to the optimal VDMLI layer density distribution: 16 layers/cm for the outer sector (S3), 11 layers/cm for the middle sector (S2), and 5 layers/cm for the inner sector (S1).
First, it can be noticed that the plot in Figure 9 is shifted down compared to the previous one, meaning that the insulation and boil-off mass are less for the VDMLI case. Moreover, it is possible to see that the lightest design options correspond to insulations that employ less MLI layers (minimum shifted to the left wrt Figure 8). This was expected as VDMLI reduces the heat leak through the insulation layers, meaning that the same performance can be achieved with less layers.

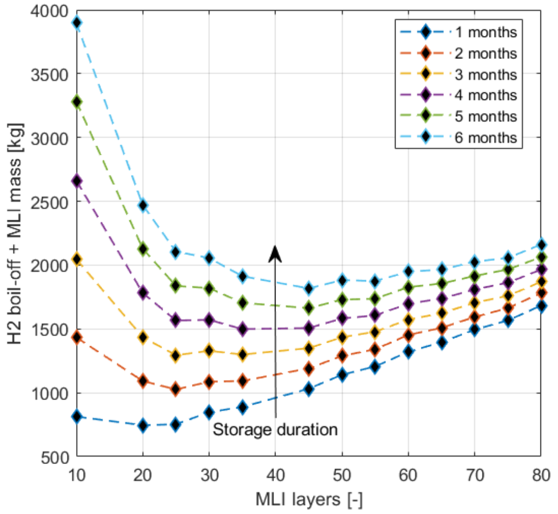

Figure 9. Boil-off + MLI mass vs number of MLI layers for storage durations from 1 to 6 months, VDMLI, 34.6 mT of LH2 storage in GEO.

The most efficient mass combinations for the Variable density MLI case are shown in Table 1. Here the boil-off rate and the storage duration can be used to retrieve the total boil-off mass and, consequently, the insulation mass from the values displayed in the third column (MLI+BO).

Table 1. Most mass efficient designs for VDMLI, liquid hydrogen storage in GEO.

Months	# MLI	MLI+BO [kg]	BO rate [%initial mass/month]
1	20	750	1.00
3	25	1300	0.78
6	45	1820	0.45
12	65	2655	0.33

Finally, Table 2 shows the effects on system mass and boil-off rate of adding a vapor cooled shield in the middle VDMLI sector.

Table 2. Most mass efficient designs for VDMLI and VCS, liquid hydrogen storage in GEO.

Months	# MLI	MLI+BO [kg]	BO rate [%initial mass/month]	wrt VDMLI [%]
1	20	870	0.93	+17%
3	25	1360	0.70	+5%
6	45	1820	0.38	0%
12	65	2520	0.26	-5%

As expected, adding a vapor cooled shield reduces the monthly boil-off rate of the liquid hydrogen stored in the tank with respect to the case of VDMLI only. However, choosing this thermal control option starts to bring mass reduction benefits only for storage durations longer than 6 months, as adding the shield introduces a mass penalty in the thermal insulation design, which is expected to be around 150 kg for an aluminium shield for this specific tank geometry.

4.2 LEO propellant depot

The same analysis as above is performed for the LEO depot case. As stated before, the relevance of this case lies in the extreme thermal environment the depot is subjected to, since not only solar, but also albedo and planetary radiation contribute to the thermal fluxes incoming in the tank.
The effect of the added fluxes can already be seen in the monthly boil-off rates, which increase compared to the GEO case, as later shown in Table 4.

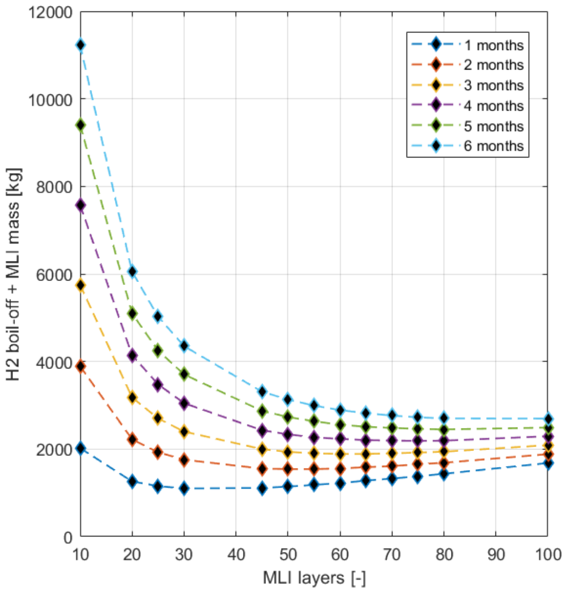

Figure 10. Boil-off + MLI mass vs number of MLI layers for storage durations from 1 to 6 months, UDMLI, 34.6 mT of LH2 storage in LEO.
For the UDMLI case, the boil-off and insulation mass combination has shown the same trends as the GEO case, with the difference that the plots are shifted up, reaching an upper limit for the insulation and boil-off mass of about 12 mT (see Figure 10). This was expected as, for the same MLI layers and thus same insulation mass, the boil-off mass is more due to the higher monthly rates. Consequently, the most mass efficient designs (plot minimum) are shifted to the right, meaning that more MLI layers are needed to achieve the best mass balance.
In particular, the region of interest for the UDMLI case is located for MLI layers between 30 and 80.
The same procedure as the GEO depot case is followed for the VDMLI and VCS case studies. The resulting most efficient mass designs are shown in Table 3.

Table 3. Most mass efficient designs for VDMLI and VCS comparison, liquid hydrogen storage in LEO.

Months	# MLI	VDMLI		VCS		Diff [%]
		MLI+ BO	BO rate	MLI+ BO	BO rate	
1	25	1000	1.50	1060	1.22	+6%
3	45	1770	0.87	1685	0.65	- 5 %
6	55	2570	0.72	2265	0.51	-12 %
12	75	3685	0.53	3040	0.34	-18 %

* MLI+BO in [kg], BO rate in [% initial mass/month]

Like before, for the LEO case using the VCS is beneficial in terms of boil-off rates reduction. However, contrarily to GEO, the use of VCS in LEO starts bringing benefits in terms of mass already after 3 months of storage.

4.3 Architectures comparison

As already mentioned, being the LEO case most critical in terms of external thermal fluxes, the resulting boil-off rates are higher than a depot placed in GEO (see Table 4).

Table 4. Boil-off rate, GEO vs LEO, 34.6 mT of LH2.

Monthly Boil-off rate [%initial mass/month]				
	# MLI	UDMLI	VDMLI	VCS
GEO	20	1.41	1.00	0.93
	45	0.65	0.45	0.38
	55	0.54	0.38	0.31
	65	0.47	0.33	0.26
	80	0.38	0.27	0.20
LEO	20	2.76	1.94	1.74
	45	1.27	0.87	0.65
	55	1.05	0.72	0.51
	65	0.89	0.62	0.42
	80	0.73	0.51	0.32

Table 5. Summary of GEO and LEO depot best design options for 6 and 12 months of storage, 34.6 mT of LH2.

CASE	Months	# MLI	MLI+BO [kg]			BO rate [%initial mass/month]		
			UDMLI	VDMLI	VCS	UDMLI	VDMLI	VCS
GEO	6	45	2030	1820	1820	0.66	0.45	0.38
LEO	6	55	2995	2570	2265	1.05	0.72	0.51
GEO	12	65	2890	2655	2520	0.47	0.33	0.26
LEO	12	75	4335	3685	3040	0.78	0.53	0.34

To achieve the minimum insulation plus boil-off mass, a depot placed in LEO would require more insulation layers. This is confirmed by the results and is shown in Table 5 for 6 and 12 months of storage duration.
As previously mentioned, the results also show that, for the VCS to become advantageous in terms of mass, a minimum storage duration is needed, which corresponds to at least 6 months for a GEO depot, while it is reduced to 3 months for LEO. This effect is explained by the more critical thermal environment the LEO depot is in, leading to a higher boil-off. Hence, the mass penalty resulting from adding the shield is outweighed more easily by the boil-off mass for this case.

A summary of the results is given in Table 5. Among all design cases, the VCS option is the most mass efficient, both for 6 and 12 months of storage. When comparing the two propellant depot cases, it is noticed that the LEO depot requires "heavier" designs. However, by employing the VCS system, the differences in boil-off rates from the GEO case reduce.

6. Conclusions

A versatile propellant depot sizing tool has been developed. This, called the Boil-off tool, performs a multi-nodal thermal analysis of a cryogenic tank for different thermal control design options, thermal environments, and depot geometries for varying mission duration. The thermal environment definition is done using ESATAN-TMS and given as input to the tool, allowing flexibility in the depot design, and orbit and attitude selection.
As for the thermal control options, the tool includes passive means such as coatings, uniform and variable density MLI, along with active means such as vapor cooled shields and cryocoolers.
The main outputs of the Boil-off tools are the propellant boil-off rate, and the combined insulation and boil-off mass for a wide range of storage durations. If desired, heat fluxes and temperatures are also among the available outputs.
The Boil-off tool has then been applied to the single tank depot model to assess its thermal performance in two different locations, namely Geostationary and Low Earth orbit. From this analysis, some nice conclusions can already be drawn.
It has been shown that variable density MLI improves the effectiveness of the thermal insulation: the most mass efficient designs in terms of insulation plus boil-off mass are achieved with less total number of layers when VDMLI is used.
The use of vapor cooled shields additionally reduces the boil-off into the cryogenic tank. However, this system starts to be beneficial in terms of mass savings only after 6 (for GEO depots) and 3 (for LEO depots) months of storage. This is due to the mass penalty introduced by the metal shield into the system.

The final comparison has identified the GEO depot as the most convenient in terms of total system mass. However, it has to be noted that conclusions drawn here are very case-specific, and therefore only applicable to the depot designs considered in this work.
Moreover, the analysis done here is only focusing on the performance of the thermal insulation. Therefore, it is not possible to state at this stage which depot location would be the most advantageous when considering other factors like cost, life, or risk. Moreover, it should be noted that the further the depot is placed, the more resources are needed to deliver all the necessary components for its assembly in orbit.

The Boil-off tool, and the performance evaluation done in this work can be used as starting point for a wider depot system analysis that considers all the above-mentioned factors, applying them to a wider range of realistic case studies to determine the most feasible concept.
Given the limited data publicly available on propellant depots, a future step would be to perform validation of the Boil-off tool using experiments, both on ground and in micro-gravity. Furthermore, the accuracy of the mass estimation relations used in this work should be also properly verified.

Acknowledgements

This work would not have been possible without the support of the Delft University of Technology, which has provided me with the guidance, resources, and

knowledge to pursue this research. My deepest gratitude goes to my supervisor, professor Barry Zandbergen, for the continuous support and for passing on his passion for this topic to me.
A special thanks also goes to my colleagues, who have brought their insights on my work with always meaningful discussions: Bart, Mitchell, Gonçalo, Ruben, Pietro, and Swati.
I am also incredibly grateful to my space-friends: you have always brought me joy, especially in the dark days. Last but not least, I wish to thank my friends at home and my family. You have supported and encouraged me every step of the way, and I will forever be grateful for this.

References

[1] B. Kutter, F. Zegler, S. Lucas, L. Hines, M. Ragab, I. Spradley and J. Hopkins, "Atlas centaur extensibility to long-duration in-space applications," *In Space 2005 (p. 6738)*, 2005.

[2] J. De Kruif and B. F. Kutter, "Centaur upperstage applicability for several-day mission durations with minor insulation modifications," in *AIAA JPC*, 2007.

[3] L. L. Morgan, "Orbital Tanker Designs and Operational Modes for Orbit Launch Programs," *AIAA Paper, No. 65-383.*, 1965.

[4] D. Street and A. Wilhite, "A scalable orbital propellant depot design," Masters Project, Department of Aerospace Engineering, Georgia Institute of Technology, Atlanta, GA., 2006.

[5] B. Kutter, G. Oneil, B. Pitchford and F. Zegler, "A practical, affordable cryogenic propellant depot based on ULA's flight experience," in *AIAA Space 2008 Conference & Exposition (p. 7644)*, 2008.

[6] F. Zegler and B. Kutter, "Evolving to a depot-based space transportation architecture," in *AIAA Space 2010 Conference & Exposition (p. 8638)*, 2010.

[7] D. Gilmore, Spacecraft thermal control handbook, volume I: Fundamental technologies, 2002.

[8] J. Gaebler, R. Lugo, E. Axdahl, P. Chai, M. Grimes, M. Long and A. Wilhite, "Reusable Lunar transportation architecture utilizing orbital propellant depots," in *AIAA SPACE 2009 Conference & Exposition (p. 6711)*, 2009.

[9] E. Hurlbert, M. Baine and G. Grush, " An open exploration architecture using an L-1 space propellant depot," in *SpaceOps 2010 Conference Delivering on the Dream Hosted by NASA Marshall Space Flight Center and Organized by AIAA (p. 2158)*, 2010.

[10] A. Wilhite, D. Arney, C. Jones and P. Chai, "Evolved Human Space Exploration Architecture Using Commercial Launch/Propellant Depots," in *63rd International Astronautical Congress*, Naples, Italy, 2012.

[11] L. J. Hastings, D. Plachta, L. Salerno and P. Kittel, "An overview of nasa efforts on zero boiloff storage of cryogenic propellants.," *Cryogenics, 41(11-12), 833–839,* 2001.

[12] P. M. Sutheesh and A. Chollackal, "Thermal performance of multilayer insulation: a review," in *In IOP Conference Series: Materials Science and Engineering (Vol. 396, No. 1, p. 012061). IOP Publishing.*, 2018.

[13] P. Kittel, "Cryocooler Performance Estimator," in *Cryocoolers vol. 14,* 2007, p. 563–572.

[14] P. R. Chai and A. W. Wilhite, "Cryogenic thermal system analysis for orbital propellant depot," *Acta Astronautica, 102, 35–46,* 2014.

[15] W. Jiang, Z. Zuo, Y. Huang, B. Wang, P. Sun and P. Li, "Coupling optimization of composite insulation and vapor-cooled shield for on-orbit cryogenic storage tank," *Cryogenics, 96, 90–98,* 2018.

[16] W. Jiang, Z. Zuo, P. Sun, P. Li and Y. Huang, "Thermal analysis of coupled vapor-cooling-shield insulation for liquid hydrogen-oxygen pair storage," *International Journal of Hydrogen Energy, 47(12), 8000–8014,* 2022.

[17] G. E. McIntosh, "Layer by layer mli calculation using a separated mode equation," *Advances in cryogenic engineering (pp. 1683–1690), Springer,* 1994.

[18] C. Keller, G. Cunnington and A. Glassford, "Thermal performance of multilayer insulations," (technical report), 1974.

[19] L. Hastings, A. Hedayat and T. Brown, "Analytical modeling and test correlation of variable density multilayer insulation for cryogenic storage," (technical report), 2004.

[20] L. J. Hastings and J. J. Martin, "Experimental testing of a foam/multilayer insulation (fmli) thermal control system (tcs) for use on a cryogenic upper stage.," in *AIP Conference Proceedings, 420(1), 331–341,* 1998.

[21] B. Wang, Y. Huang, P. Li, P. Sun, Z. Chen and J. Wu, "Optimization of variable density

multilayer insulation for cryogenic application and experimental validation," *Cryogenics, 80, 154–163,* 2016.

[22] J. Martin and L. Hastings, "Large-scale liquid hydrogen testing of variable density multilayer insulation with a foam substrate," (technical report), 2001.

[23] I. H. Bell, J. Wronski, S. Quoilin and V. Lemort, "Pure and pseudo-pure fluid thermophysical property evaluation and the open-source thermophysical property library coolprop.," *Industrial & engineering chemistry research, 53(6), 2498–2508,* 2014.

[24] G. E. McIntosh, "Layer by layer MLI calculation using a separated mode equation," *Advances in cryogenic engineering, Springer, Boston, MA,* pp. 1683-1690, 1994.

Appendix A Boil-off tool block diagram

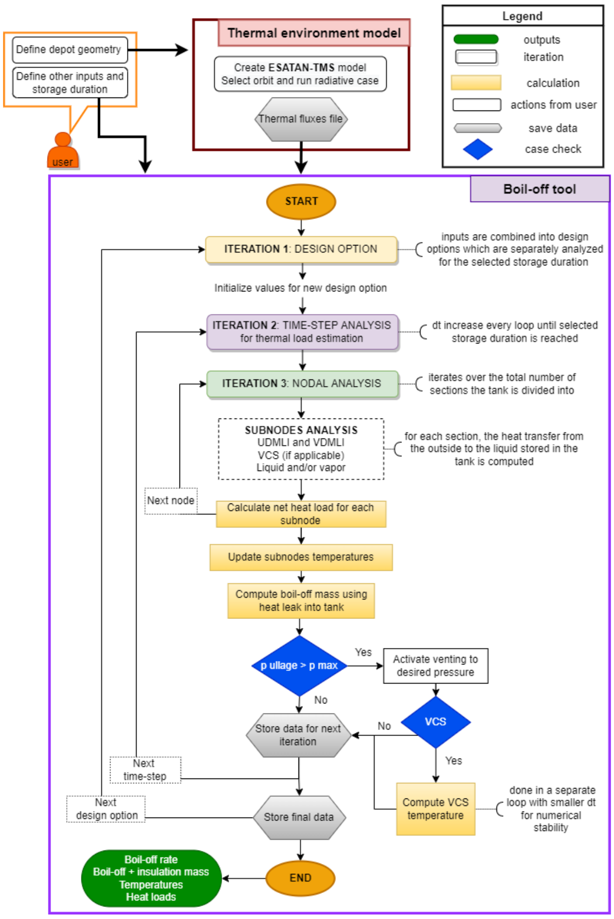

Figure 11. Boil-off tool block diagram.

Appendix B Depot attitude: effects on heat loads

One of the characteristics that make it easier to study GEO orbits is the "constant" nature of the thermal fluxes: in fact, the absence of eclipses recurring in every orbit results in almost constant solar fluxes, while the distance from the Earth's surface allows to neglect albedo and planetary fluxes, who also vary along the orbit based on the relative position of Sun, Earth, and depot itself. Nevertheless, fluxes incoming on a depot placed in GEO could still be variable, and this strongly depends on the depot attitude. Figure 12 shows the total heat loads received by the single tank model in GEO for three different depot attitudes: tank side to Sun (sunlit side colored in yellow), tank endcap to Sun (sunlit side colored in light blue), and tank longitudinal axis aligned with Nadir (shown in Figure 13).

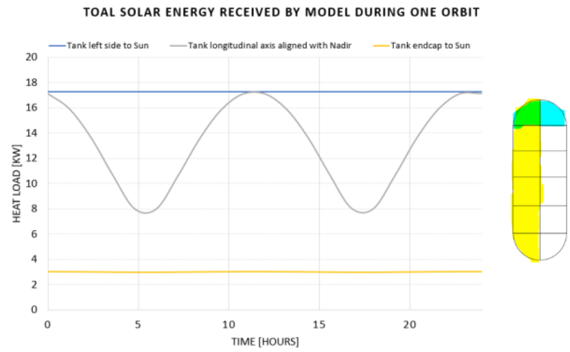

Figure 12. Total solar heat load received by the single tank model in GEO for different depot orientations.

It can be noticed from the heat load plot that aligning the tank axis with Earth's Nadir results in variable fluxes on the depot about the GEO orbit. In particular, the resulting heat loads oscillate between a minimum and maximum value based on the position of the tank in the orbit.

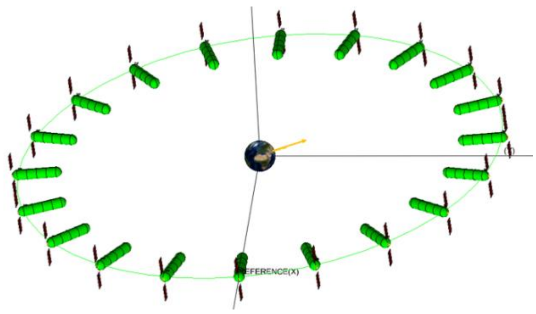
Figure 13. ESATAN-TMS orbit display of single tank GEO depot with longitudinal axis aligned with Earth Nadir.

In conclusion, heat load variability over time can depend both on the chosen orbit and depot attitude, therefore a proper thermal environment would be the one that is able to track the thermal fluxes variations over time.

This is not only valid for the GEO case just analysed, but it can also be applied to orbits characterized by daily eclipses, or variable albedo and planetary heat loads, like LEO.

The ESATAN-TMS thermal environment model chosen for this work takes into account any fluxes variability, being it because of the orbit or the spacecraft orientation.

Appendices References

[1] Richard L Burden. *Numerical analysis*. 2011.

[2] Cython. *Welcome to Cython's Documentation*. 2021. URL: `https://cython.readthedocs.io/en/latest/`.